SISSA
Scuola Internazionale Superiore di Studi Avanzati

Physics Area - PhD course in Theory and Numerical Simulation of Condensed Matter Physics

Growth and redox of borophene on Al(111) substrate

Candidate:
Mandana Safari

Advisors:
Prof. Stefano Baroni
Prof. Stefano de Gironcoli

Academic Year 2022-2023

SUMMARY

This thesis presents a comprehensive investigation of borophene growth on an Al(111) substrate, combining our theoretical analysis with the experimental findings obtained by our collaborators at the Elettra synchrotron radiation facility, in the framework of the *FERMAT* project, funded by the Italian Ministry of University and Research (MUR). The theoretical aspects of this study focus on understanding the role of oxygen and hydrogen adsorbates in the formation of various configurations, as well as their impact on the structural and electronic properties of the system. To this end, we have paid special attention to several quantum-mechanical effects, including the charge transfer mechanisms, the thermodynamic stability of different phases, and the characterization of the bond strength through the computation of the relevant vibrational frequencies. Our theoretical results greatly contribute to the understanding of the experimental findings, which are also rather extensively reported in the thesis for a comprehensive analysis of borophene growth on Al(111).

Density functional theory (DFT) combined with a genetic algorithm have been employed to predict the electronic and structural properties of borophene, oxidized borophene, and hydrogenated borophene (borophane) on Al(111). *Ab initio* thermodynamics has been implemented to find the most stable structures of the above systems in realistic conditions. Vibrational frequencies have been computed from density functional perturbation theory (DFPT). As this methodology is very compute-intensive, we have explored new methods and algorithms to reduce the compute time while enhancing its applicability. To this end, we have started a new project aimed at extending the scope of Neural Network Potentials (NNP) for calculating the phonon dispersion of materials explicitly accounting for the effects of long-range interactions.

The calculated total energy, phonon frequency, band structure, and density of states of borophene, oxidized borophene, and borophane on Al(111) provide the theoretical counterpart to the experimental observations performed with Low-Energy Electron Diffraction (LEED), Infrared-Visible Sum Frequency Generation (IR-Vis SFG), and X-ray Photoelectron Spectroscopy (XPS), and other techniques.

Our computational study reveals that: (*i*) The coupling between Al(111) and borophene leads to the formation of strong Al–B bonds, which can be modulated by oxygen doping due to the higher

tendency of oxygen to combine with aluminum. Experimental results confirm this finding. (*ii*) The hydrogenation of borophene on Al(111) induces the formation of a well-ordered honeycomb borophane phase with interesting electronic conductivity properties.

In summary, the study contributes to the understanding of the mechanism of borophene growth on metal substrates. It provides insights into the control of the electronic properties of boron-based materials. The results have implications for developing novel 2D materials with tailored properties for technological applications such as nanoelectronics and energy storage.

In the course of this research, several studies were conducted and significant findings were obtained. The following papers have been published or are currently in progress, highlighting the outcomes of this work:

- M. Safari, E. Vesselli, S. de Gironcoli, S. Baroni. 'Growing borophene on metal substrates: A theoretical study of the role of oxygen on Al(111).' Phys. Rev. Mater. 6, issue 11, (2022), 115801-115811.

- M. Safari, Y. Shaidu, S. de Gironcoli. 'Correct Vibrational Properties of Polar Materials from Neural Network Interatomic Potentials.' Proceedings poster presented at Psi-k 2022 conference, EPFL, Lausanne, Switzerland.

- P. Biasin, M. Safari, E. Ghidorsi, S. Baronio, A. Preobrajenski, S. de Gironcoli, S. Baroni, E. Vesselli. 'From borophene polymorphs towards a single honeycomb borophane phase: reduction of hexagonal boron layers on Al(111).' Manuscript submitted to Nanoscale (2023).

- P. Biasin, M. Safari, E. Ghidorsi, S. Baronio, M. Scardamaglia, A. Preobrajenski, N. Vinogradov, A. Sala, G. Comelli, C. Cepek, S. de Gironcoli, S. Baroni, E. Vesselli. 'Growth and redox properties of borophene: competing affinities and the case of honeycomb AlB2/Al(111).' Manuscript in preparation.

ACKNOWLEDGEMENTS AND GRATITUDE

Foremost, I would like to extend my heartfelt appreciation to my esteemed advisors, Prof. Baroni, and Prof. de Gironcoli, for their unwavering support, guidance, and profound expertise throughout my Ph.D. journey. Their continuous encouragement, patience, and enthusiasm have been instrumental in shaping my research and academic growth. I am truly grateful for their invaluable mentorship, which has played a pivotal role in the successful completion of this thesis.
In addition to my advisors, I extend my gratitude to Yusuf Shaidu and Pietro Delugas for their technical assistance, uplifting encouragement, and insightful contributions. Their valuable input, thought-provoking discussions, and shared knowledge of simulation techniques and physics have greatly enriched my understanding and enhanced the quality of my research work. I appreciate their help with the technical problem using the USPEX code and many useful discussions on Quantum ESPRESSO and using the GPU accelerator for phonon calculations.

I want to thank our experimental collaborators, Pietro Biasin and Prof. Erik Vesselli at SFG laboratory at the University of Trieste and Elettra (Elettra Sincrotrone Trieste), that shared their results with me. This work is supported by the Italian MUR through the PRIN project *FERMAT* 2017KFY7XF and by the University of Trieste through project FRA2022, with access to the FlexPES beamline of the MAX IV synchrotron radiation facility granted upon proposal no. 20220034. I had the chance to visit their laboratory at Elettra, and we had a very good discussion on the technical details of the experimental work.
This work is also partially funded by the EU through the MaX Centre of Excellence for supercomputing applications (grant numbers 824143 and 10109337).

In the end, I would like to thank my friends in SISSA and Trieste: Ali, Emine, Franco, Guglielmo, Mahsa, Mina, Niloofar, Nicolas, Nishan, Roggero, as well as my friends in the mHPC course: Alfredo, Andrea, Daniel, Iara, Irina, Fernando, Keshvi, Massimo, Neeraj for their supports, enlightening scientific discussion, and for all the fun we have had in these years.
Hereby I thank my colleagues: Alberto, Fabio, Martino, Paolo, Philip, Riccardo, and Vittorio for their helpful discussions during first-year

lectures.
Also, I thank my friends from Iran. In particular, I am grateful to Rayehe for all the encouraging and supporting moments of our 16-year-old friendship.
I would like to thank my family: my parents, my brother, and my sister for supporting me spiritually throughout my life.
Last but not least, I would like to thank Mohammad for all his kindness, love, support, help, and presence during my difficult moments.

To Mahsa Amini (1999-2022),

and to all the brave women who fight for their rights...

CONTENTS

LIST OF FIGURES

1 INTRODUCTION: A GENERAL OVERVIEW

The unique characteristics of two-dimensional (2D) boron allotropes, such as their metallic behavior, the existence of Dirac fermions, charge density waves, and potential for superconductivity, have captured growing attention. These physical and chemical properties make them promising for various applications in quantum electronics, energy storage, catalysis, and sensing [33, 72, 106, 140, 150].

The reason why boron (B) forms different allotropic structures in three dimensions (3D) is that it has fewer electrons compared to carbon (C), resulting in multi-centered bonding. However, when we consider a two-dimensional (2D) system, the stability of a boron layer is compromised due to its electron-deficient configuration. In order to stabilize a nearly flat (pure) boron material, self-doping can be employed, leading to a buckled triangular structure.

On the other hand, the density[1] η and the spatial arrangement of boron hexagonal holes play a significant role in generating various 2D boron allotropic phases. These phases can potentially be stabilized through the introduction of compensating external doping. Indeed, in order to supply the necessary electronic charge for stabilization, the interaction and bonding with a supporting (metal) substrate or chemical doping are needed.

Recently, a number of cases have been observed experimentally and thoroughly characterized. For the Ag(111) substrate [34, 78], physical vapor deposition of boron yields the formation of two prevailing structures, the S_1 (predicted to be β_{12} with $\eta = \frac{1}{6}$) and S_2 (predicted to be χ_3 with $\eta = \frac{1}{5}$) phases, the latter being more stable than the former. Surface temperature (in the 620 K – 720 K range) [34, 72, 78] and boron deposition rate actually determines the relative coverage of the different domains, showing that the small energy difference between the structures and the kinetic hindrance strongly affect the experimental phase diagram.

At a temperature of 820 K, when B is deposited on a gold (Au(111)) substrate with a herringbone surface reconstruction [136], the original

1 The hexagonal hole density η can be defined as:

$$\eta = \frac{\text{The number of hexagonal holes}}{\text{The number of atoms in the original triangular sheet}} .$$

This parameter can characterize boron sheets with a mixture of triangles and hexagons.

pattern is disrupted. Instead, a new trigonal network is formed, consisting of borophene sheets characterized by $\eta = 1/12$ [58]. As the amount of boron is increased, larger islands of borophene form, expanding the size of the domains. However, it is worth noting that to achieve complete coverage of a single layer of borophene, the required dose of boron is ten times higher compared to the case of deposition on a silver (Ag) substrate. Through the analysis of core levels and depth profiling, it has been observed that on Au(111), boron atoms exhibit a behavior where they diffuse into the bulk. This diffusion process involves a complex mechanism that is influenced by temperature, resulting in segregation, alloying, and migration within the subsurface region. Remarkably, this behavior bears similarities to the conversion chemistry observed during the carbon-carbide-graphene transformation on the nickel surface (Ni(111)) [87, 143].

Finally, we come to one of the most interesting 2D boron phases, i.e. the honeycomb boron layer ($\eta = 1/3$) that can be synthesized on Al(111). The geometry of the layer, resembling the B atomic planes of the crystalline MgB_2 bulk superconductor, guarantees the presence of Dirac fermions, a high carrier mobility, and a bunch of other properties that boosted the experimental search for the possible stabilization of this 2D boron allotrope in extended domains. The first evidence reports a honeycomb phase (hB) that can be stabilized thanks to the charge doping offered by the aluminum substrate [69]. The lattice mismatch (0.298 nm for borophene vs 0.286 nm for the Al surface) permits the formation of hB domains with a 60-75 Å coincidence Moiré supercell and a 40-60 pm corrugation amplitude. However, the B-Al covalent interaction, which provides the stabilizing charge transfer, is also responsible for the strong coupling of the boron layer to the substrate, so that an AlB_2 sheet is actually formed [39, 96].

From this overview, it becomes evident that a metal substrate is essential for stabilizing low-density borophene phases through electron doping. However, the strong coupling between boron and the supporting metals complicates the separation of the boron layer from the growth substrate. This challenge is not only mechanical but also arises from a physical and chemical standpoint. This is because the properties of the borophene layer are intricately linked and influenced by the properties of the underlying substrate. In addition, the actual (meta)stable boron structure, that is experimentally obtained, can in principle be far from optimal due to the coexistence of several phases that are very close in energy and therefore, kinetically speaking, very difficult to separate. In this context, it is important to take into account that various phenomena such as segregation, diffusion, and alloying play a significant role in the growth and formation of 2D

boron allotropes. These processes can be influenced by the chemical potential of gases and specific adsorbates.

The redox properties of different 2D boron structures are closely influenced by how boron and the metal substrate interact with elements like oxygen or hydrogen. Specifically, when it comes to oxygen, there is a strong interaction between oxygen and the metal, leading to notable segregation processes that cause the formation of an oxide layer. A similar case can be observed in the self-limited growth of an extremely thin alumina film on the $Ni_3Al(111)$ termination. The process involves the expulsion of aluminum atoms from the surface and the creation of a diluted aluminum interface layer. However, this mechanism is subject to kinetic restrictions that impact its overall progression [76, 128]. An instructive and closely related example comes then from the aluminum oxide growth on Al(111), governed by the motion of the buried metal-oxide interface [46], where the outward growth is associated with the Al^{3+} ion transport from the metal bulk to the oxide phase already at room temperature.

In terms of reduction, recent experiments have focused on isolating larger borophane phases through direct hydrogenation of borophene [141]. For instance, on Ag(111), it was discovered that multiple phases coexist on the surface, with a small portion consisting of honeycomb borophane and the dominant polymorph exhibiting a mixture of two-center-two-electron B–H and three-center-two-electron B–H–B bonds. The H adsorption sites are determined by the local B coordination and the interaction with the metal substrate plays a fundamental role in this sense [55]. Moreover, the reduction of borophene yields its chemical passivation and reduces in particular the oxidation rates [67].

In this thesis, a thorough investigation of the growth of borophene on an Al(111) substrate is presented. The study combines theoretical analysis and experimental findings obtained through collaboration with other researchers. The main focus of the theoretical analysis is to understand the role played by oxygen and hydrogen atoms in the formation of different configurations and how they influence the structural and electronic properties of the system. Additionally, the study explores the charge transfer mechanism, compares the thermodynamic stability, and investigates the strength of bonds using phonon frequencies. The experimental results significantly contribute to our understanding of the system and are incorporated into the thesis to provide a comprehensive analysis of borophene growth on Al(111).

To predict the electronic and structural properties of borophene, oxidized borophene, and hydrogenated borophene (borophane) on Al(111), density functional theory (DFT) combined with a genetic

algorithm is employed. Additionally, *ab initio* thermodynamics is used to determine the most stable structures in realistic conditions. In the study, density functional perturbation theory (DFPT) is initially chosen to calculate phonon frequencies, and efforts are made to find new methods and algorithms that reduce computational time and increase applicability. A preliminary investigation of Neural Network Potentials (NNP) is conducted to calculate the phonon dispersion of materials for various applications.

The theoretical calculations of the total energy, phonon frequency, band structure, and density of states for borophene, oxidized borophene, and borophane on Al(111) serve as a basis for understanding experimental observations. Techniques like Low-Energy Electron Diffraction (LEED), Infrared-Visible Sum Frequency Generation (IR-Vis SFG), and X-ray Photoelectron Spectroscopy (XPS) are used to obtain these experimental observations. The theoretical results provide a solid framework to interpret and explain the experimental findings obtained from these techniques.

The theoretical study reveals two significant findings: (i) The interaction between Al(111) and borophene results in the formation of strong Al–B bonds, which can be adjusted by introducing oxygen due to oxygen's strong affinity for aluminum. This finding is confirmed by experimental results. (ii) Hydrogenation of borophene on Al(111) leads to the creation of a well-organized honeycomb borophane phase with intriguing electronic conductivity properties.

This study enhances our understanding of the mechanism behind borophene growth on metal substrates and provides insights into controlling the electronic properties of boron-based materials. The findings have implications for the development of novel 2D materials with tailored properties for applications in nanoelectronics and energy storage.

Here is a general overview of the topics which will be introduced in each chapter:

- Chapter 2: A brief overview of theoretical background based on density functional theory, *ab initio* thermodynamics, *ab initio* lattice dynamics (DFPT), and genetic optimization techniques.

- Chapter 3: An investigation of the electronic and structural properties of borophene grown on Al(111), completed by a thorough study of the thermodynamic stability of the borophene-Al(111) interface.

  - Complementary experimental study on the characterization of 2D boron polymorphs and the synthesis of stable, homogeneous borophene monolayers. Experimental results confirmed the formation of Al–B bonds.

- Chapter 4: An investigation of the electronic and structural properties of oxidized borophene grown on Al(111), with emphasis on the impact of oxygen on the strength of the coupling between substrate and overlayer, completed by a thorough study of the thermodynamic stability of the oxygenated borophene-Al(111) interface.

  - Complementary experimental study on the characterization of experimental results confirmed the formation of Al–O bonds and predicted that oxygen doping reduces charge transfer between aluminum and borophene, thus allowing modulation of their strength and paving the way to engineering the electronic properties of 2D-supported borophene sheets for industrial applications.

- Chapter 5: The theoretical study of structural prediction of different hydrogenated borophene and charge transfer investigation as well as phonon frequencies. Hydrogenation of borophene was addressed as a promising chemical passivation treatment that can in parallel modulate the boron-substrate interaction, thus stepping towards the synthesis of a stable, (almost) free-standing honeycomb phase with interesting electron conductivity properties.

  - Experimental evidence was provided for the (reversible) formation of well-ordered honeycomb borophane upon hydrogenation of the honeycomb boron phase on Al(111) in the lab, as a complementary discussion.

- Chapter 6: Proposing a recently developed method for speeding up the calculations, with a specific focus on long-range correction in artificial neural network interatomic potentials to reach correct phonon dispersion spectra. It includes an overview of Machine learning techniques, especially Neural Network for interatomic potentials (NNIP).

- Chapter 7: Conclusion, recap, and implications for future research and industrial applications, and limitations and future directions for the study.

- Appendix A: Computational details.

- Appendix B: Experimental supporting information, including methods and techniques that mostly were used in experiments.

2 THEORETICAL BACKGROUND

All physical systems can be thought of as registering and processing information, and how one wishes to define computation will determine your view of what computation consists of. —-Seth Lloyd.

The field of materials science focuses on designing and applying materials, but to achieve this, a deep understanding of the material's atomic-scale functionality is required. To gain this understanding, models must account for the behavior of electrons and their interactions with atoms and molecules in the system. Electronic structure theory methods, such as density functional theory (DFT), have become standard tools for studying these phenomena. These methods are referred to as "first-principles" or "*ab initio*" methods, meaning they do not rely on empirical or fitted parameters. Because of this, they can be applied to a wide range of realistic conditions, including varying temperatures and pressures, in what is known as *ab initio* thermodynamics [102], as well as finding the most stable structures, known as structural prediction.

In this chapter, a brief review of the theoretical background, underlying the computational methods used in this thesis, is presented.

2.1 DENSITY-FUNCTIONAL THEORY

The quantum mechanical study of a many-body system including electrons and nuclei requires the definition of a suitable Hamiltonian. This Hamiltonian generally operates on a many-body wavefunction of both electronic and ionic coordinates. The first approximation which makes it solvable is the Born-Oppenheimer (also called adiabatic) approximation. This approximation allows one to disentangle the ionic degrees of freedom from the electronic ones. Although the momenta of these particles are comparable, this separation is valid due to the fact that the ratio of the electronic mass to nuclei mass is very small ($\frac{m_e}{M_I} \leqslant 10^{-3}$). On the other hand, the time scale of ionic dynamics is much longer than the electronic one, which allows us to neglect the ionic kinetic energy when studying electronic motion.

These facts take credit to solve the problem of N interacting electrons, considering fixed ions acting as an external potential V_{ext}.

Considering the adiabatic approximation, the many-body Schrödinger equation of N_e electrons in the external potential of the nuclei can be written as:

$$H_{\mathbf{R}}\psi_{\mathbf{R}}(\mathbf{r}) = E(\mathbf{R})\psi_{\mathbf{R}}(\mathbf{r}) \,, \tag{2.1.1}$$

where $\psi_{\mathbf{R}}(\mathbf{r})$ is considered as the many-body wavefunction of electrons at fixed nuclear positions $\mathbf{R}$ and Hamiltonian appearing in this equation is:

$$H_{\mathbf{R}} = -\sum_{i=1}^{N_e} \frac{\hbar^2}{2m_e}\nabla^2_{\mathbf{r}_i} + \frac{1}{2}\sum_{i\neq j}\frac{e^2}{|\mathbf{r}_i - \mathbf{r}_j|} - \sum_{i,I}\frac{Z_I e^2}{|\mathbf{r}_i - \mathbf{R}_I|} \,, \tag{2.1.2}$$

where $\mathbf{R}_I$ and $\mathbf{r}_i$ are coordinates of the nuclei and electrons, respectively, $Z_I e$ is the charge of the I-th nucleus, and e and m_e are the electronic charge and mass, respectively. The electronic wavefunction $\psi_{\mathbf{R}}(\mathbf{r})$ as a function of $3N_e$ electronic degrees of freedom, is still unsolvable.

In order to turn this problem into a solvable question, one needs other approximations. One of the well-known approaches to solving this problem is density functional theory. This approach was introduced in 1964 by Hohenberg and Kohn (HK) [51], who showed a one-to-one correspondence between an external potential V_{ext} and a non-degenerate ground-state electronic charge density $n_0(\mathbf{r})$:

$$n_0(\mathbf{r}) = \langle\psi_0(\mathbf{r}_1, ..., \mathbf{r}_N)| \sum_{i=1}^{N} \delta(\mathbf{r} - \mathbf{r}_i) \,|\psi_0(\mathbf{r}_1, ..., \mathbf{r}_N)\rangle \,, \tag{2.1.3}$$

where ψ_0 is the non-degenerate ground state wavefunction. The first Hohenberg–Kohn theorem states that 'the ground state of any interacting many-particle system with a given fixed inter-particle interaction is a unique functional of the electron density $n_0(\mathbf{r})$'. Since the external potential also determines the many-body wavefunction of the ground state ψ_0, every observable of the system in its ground state can be expressed as a functional of the ground state electron density $n_0(\mathbf{r})$. This implies the validity of introducing ground-state total energy as a functional of the electronic charge density of the ground-state:

$$\begin{aligned} E[n_0(\mathbf{r})] &= \langle\psi_0(\mathbf{r}_1, ..., \mathbf{r}_N)|\, H \,|\psi_0(\mathbf{r}_1, ..., \mathbf{r}_N)\rangle \\ &= F[n_0(\mathbf{r})] + \int_V d^3\mathbf{r} V_{ext}(\mathbf{r}) n_0(\mathbf{r}) \,. \end{aligned} \tag{2.1.4}$$

The functional $F[n_0(\mathbf{r})]$ is known as the HK universal functional, which can be calculated, at least in principle, by evaluating the kinetic

and interaction terms on the ground state. Due to the HK theorem, the minimum of total energy functional $E[n(\mathbf{r})]$ occurs at the charge density ($n_0(\mathbf{r})$) of the ground state. Consequently, minimizing the total energy functional in 2.1.4 with respect to density $n(\mathbf{r})$, for a given number of electrons N, yields the ground state total energy and electronic density. However, the exact form of the kinetic and interaction density functional $F[n(\mathbf{r})]$ is not known. In 1965 Kohn and Sham [61] introduced a map for this many-body functional into an auxiliary non-interacting electron system with the ground-state density of the initial system. In this regard, the functional can be written into three terms:

$$F[n] = T_s[n] + E_H[n] + E_{xc}[n] \, . \tag{2.1.5}$$

The kinetic energy of the non-interacting system, $T_s[n]$, is:

$$T_s[n] = \sum f_i \left\langle \phi_i \right| - \frac{\hbar^2}{2m_e} \nabla^2 \left| \phi_i \right\rangle \, , \tag{2.1.6}$$

where f_i and ϕ_i are the occupation and wavefunction of state i, respectively. The classical Hartree electrostatic energy of a system with charge density n is defined as:

$$E_H[n] = \int d^3\mathbf{r} d^3\mathbf{r}' n(\mathbf{r}) \frac{e^2}{|\mathbf{r} - \mathbf{r}'|} n(\mathbf{r}') \, . \tag{2.1.7}$$

The exchange-correlation functional, E_{xc}, holds actually all the many-body details of the system.

The energy functional associated with the external potential can also be written as:

$$E_{ext}[n] = \sum_i f_i \left\langle \phi_i \right| V_{ext} \left| \phi_i \right\rangle \, . \tag{2.1.8}$$

Then one could rewrite equation 2.1.4 as:

$$E[n] = T_s + E_H + E_{xc} + E_{ext} \, , \tag{2.1.9}$$

and minimize this functional with respect to the orthonormal single-particle wavefunctions ϕ_i using Lagrange multipliers. The solution of this minimization leads to the Kohn-Sham (KS) equation:

$$\left(-\frac{\hbar^2}{2m_e} \nabla^2 + V_{KS}(\mathbf{r}) \right) \phi_i(\mathbf{r}) = \epsilon_i \phi_i(\mathbf{r}) \, , \tag{2.1.10}$$

where the effective Kohn-Sham potential V_{KS} is defined as:

$$V_{KS} = V_{ext} + V_H + V_{xc} \, , \tag{2.1.11}$$

in which

$$V_H(r) = \int \frac{d^3\mathbf{r}' n(\mathbf{r}') e^2}{|\mathbf{r} - \mathbf{r}'|} \, .$$

Notice that V_H is the Hartree potential, and the exchange-correlation potential is defined as the functional derivative of the exchange-correlation energy term:

$$V_{xc}(\mathbf{r}) = \left.\frac{\delta E_{xc}}{\delta n(\mathbf{r})}\right|_{n(\mathbf{r})=n_0(\mathbf{r})} . \tag{2.1.12}$$

Therefore the auxiliary one-electron wavefunction, ϕ_i, can be obtained from the solution of KS equations. Then the ground-state density can be constructed easily as follows:

$$n_0(\mathbf{r}) = \sum_i f_i |\phi_i(\mathbf{r})|^2 . \tag{2.1.13}$$

Based on the above single-particle equations, the KS scheme can be interpreted as a mean-field approach where an electron is affected by the potential of the surrounding nuclei. In this case, the interaction with other electrons takes place through the charge density. Therefore the charge density of the ground state depends on the single-particle solutions, which in turn, depends on the density. The solution can be achieved via a self-consistent iterative procedure or via global minimization strategies such as conjugate gradient [105]. The self-consistent iterative procedure is used for this study.

The previously described density functional theory (DFT) is accurate under the Born-Oppenheimer approximation, but its practical utility is limited because we do not have an analytical expression for the exchange-correlation density functional (E_{xc}). A critical step in DFT is to replace this unknown functional with an approximation. The first and simplest approach to be proposed was the Local Density Approximation (LDA) where the exchange-correlation energy density of a homogeneous gas of interacting electrons with constant charge density, $\epsilon_{xc}^{hom}(n)$, is used as an approximation for the non-homogeneous system of interest, as follows:

$$E_{xc}[n(\mathbf{r})] = \int_V d^3\mathbf{r}\, n(r)\epsilon_{xc}^{hom}(n(\mathbf{r})) . \tag{2.1.14}$$

Here $\epsilon_{xc}^{hom}(n)$ is a well-defined function that can be calculated using Monte Carlo simulations[20]. Since the birth of DFT, many functional forms have been proposed for the E_{xc} functional. Different interpolation schemes have been proposed for ϵ_{xc}^{hom}, such as the one introduced by Perdew and Zunger [89] in 1981.

A significant step that improved the performance of DFT was the proposal of Perdew and Wang in 1991 [91]. They introduced a new functional form that depends not only on the local density but also on its gradient, which is known as Generalized Gradient Approximation (GGA). GGA improved some deficiencies of LDA method, especially for systems with strong inhomogeneities in the charge density. Many

different reformulations and extensions of GGA have been proposed and tested over the years. One of the most commonly used GGA functionals in the condensed matter community is the PBE functional, proposed by Perdew, Burke, and Ernzerhof [90]. A revision of PBE (revPBE) was suggested by Zhang and Yang and demonstrated improved atomic energies for several elements[146].

Both PBE and revPBE do not simulate the van der Waals interactions correctly, which is a common problem of any local and semi-local density functional. A recent solution to this problem has been proposed by Dion and his colleagues [28] with a non-local functional called vdW-DF. The development of non-local functionals is still ongoing, some very recent studies propose several new functionals such as vdW-DF2 [63] and c09x [23], which do not include any drastic changes but are mostly aiming to tune the exchange functionals that can be used with the nonlocal correlation part of vdW-DF for better results.

2.2 *AB INITIO* THERMODYNAMICS

One of the applications of first-principle calculations is studying materials features at different conditions of temperature and pressure. This is achievable with some consideration in a realistic environment. It is worth mentioning that the energetic information known as total energy can be obtained as a function of the atomic configuration $\{R_I\}$. This concept leads to the so-called potential energy surface (PES) $E(\{R_I\})$, which then contains the relevant information needed to describe the effect of temperature on the atomic positions. A (meta)stable atomic configuration refers to a state where the PES reaches a local minimum. The forces exerted on the atoms within this configuration correspond to the local gradient of the PES, and the vibrational modes are determined by the curvature of the PES around the local minimum.

To extend this understanding to situations involving finite temperature and pressure, it is necessary to incorporate thermodynamics. *Ab initio* atomistic thermodynamics employs the knowledge of the first-principles PES to calculate thermodynamic potential functions, such as the Gibbs free energy [108]. This approach allows for matching between the atomic configurations and the corresponding thermodynamic properties at finite temperature and pressure [102] [1].

1 This section is mostly based on ref [102] and references quoted therein.

2.2.1 Surfaces in realistic environments

Since our study focuses on equilibrium situations, we focus on the equilibrium geometry and composition of a solid surface in contact with a given environment at finite temperature and pressure. This means that the evolution and atomic exchange are stable.

The general framework was introduced by Scheffler *et al.* [102] in the late nineties. To investigate this setup, the appropriate thermodynamic potential function is the Gibbs free energy. The absolute Gibbs free energy (G) of the entire system consisting of surface, gas, and solid can be rewritten as:

$$G = G_{solid} + G_{gas} + \Delta G_{surf} \, , \tag{2.2.1}$$

where G_{solid} refers to the Gibbs free energy of the bulk part of the solid phase, G_{gas} is the Gibbs free energy of the homogeneous gas phase, and an additional term introduced through the surface (ΔG_{surf}).

If the surface is homogeneous as in the case of an ideal single-crystal surface, ΔG_{surf} will scale linearly with the surface area A. Dividing this quantity by surface area leads to the surface free energy per unit area (γ).

$$\gamma = \frac{1}{A}(G - G_{solid} - G_{gas}) \, . \tag{2.2.2}$$

γ is accurately determined by a finite portion of the overall (infinite) system. When we consider a distance away from the surface that is large enough, both the solid phase and the gas phase of the entire system are no longer influenced by the presence of the surface. Although these (infinite) components are present in G, they effectively cancel out when we subtract the equivalent energies of the homogeneous gas phase (G_{gas}) and solid phase (G_{solid}). As a result, only the finite part of the system that is influenced by the surface becomes significant. If we denote N_M and N_{gas} as the numbers of metal and gas atoms per unit surface area, respectively, we can express γ as equation 2.2.3 based on the transformation from equation 2.2.2. Therefore,

$$\gamma(T,p) = \frac{1}{A}(G(T,p,N_M,N_{gas}) - N_M g_M(T,p) - N_{gas}\mu_{gas}(T,p)) \, , \tag{2.2.3}$$

where g_M is the Gibbs free energy per metal atom in the bulk[2], and μ_{gas} refers to the gas chemical potential of the gas phase.

2 In the case of an infinite and homogeneous system, g is equivalent to the chemical potential μ. It means if the reservoir is a homogeneous system, μ gives the cost at which this reservoir provides particles without any detectable change in pressure and temperature. To emphasize the reservoir feature of surrounding gas, μ is substituted with g in this framework.

When we refer to a more negative Gibbs free energy, it means that the system is in a more stable state. In terms of interpreting the chemical potential, this corresponds to the chemical potential (μ) approaching negative infinity as the gas becomes infinitely dilute.

A positive surface free energy per unit area ($\gamma > 0$) indicates the cost of creating the surface between the solid bulk phase and the gas phase (homogeneous gas). Alternatively, when we talk about the stability of phases that occur when certain substances are adsorbed on a solid surface, it can be helpful to use a different reference point. Instead of using γ to represent the energy required to create the surface, we can use the surface-free energy of the clean surface as a reference:

$$\begin{aligned}\Delta G_{ad}(T,p) &= \gamma(T,p,N_O,N_M) - \gamma_{clean}(T,p,0,N_M^{'}) \\ &= \frac{1}{A}(G(T,p,N_O,N_M) - G(T,p,0,N_M^{'}) \\ &\quad - N_O\mu_O(T,p) - (N_M - N_M^{'})g_M(T,p))\,, \end{aligned} \tag{2.2.4}$$

where $\gamma_{clean}(T,p) = \frac{1}{A}(G(T,p,N_M,0) - N_M g_M(T,p))$.

At a given temperature and pressure in the gas phase, the most stable surface structure and composition is determined by minimizing the surface free energy or by minimizing the Gibbs free energy of adsorption at the relevant oxygen chemical potential.

In order to calculate these quantities (γ or ΔG_{ad}), we need the Gibbs free energy of the solid surface and of the solid bulk, as well as the chemical potential of the oxygen environment. It is better to investigate each factor separately (because of different contributions to free energies in the gas phase and in the solid phase).

Gas phase chemical potential

The chemical potential of oxygen is determined by the condition of thermodynamic equilibrium with the surrounding gas phase reservoir. In the context of our needs, oxygen gas can be characterized by ideal gas regulations. The chemical potential is indicated at a specific temperature (T) and pressure (p) and expressed as follows:

$$\mu_O(T,p) = \frac{1}{2}\mu_{O_2(gas)}(T,p) = \frac{1}{2}\frac{(-k_B T \ln Q^{tot}_{O_2(gas)}) + pV)}{N}\,. \tag{2.2.5}$$

Here $Q^{tot}_{O_2(gas)}$ is the partition function of an ideal gas composed of N indistinguishable O_2 molecules. Based on statistical physics, this quantity can be written as below:

$$Q^{tot}_{O_2(gas)} = \frac{1}{N!}(q_{O_2})^N = \frac{1}{N!}(q^{trans}q^{rot}q^{vib}q^{electr}q^{nucl})^N\,. \tag{2.2.6}$$

The equation 2.2.6 is derived by considering the partition function of one O_2 molecule (q_{O_2}). This partition function can be split into

different functions, each related to a particular type of molecular motion. In this context, we have assumed that the nuclear and electronic degrees of freedom are distinct from the vibrational and rotational motions. The vibrational and rotational motions have been considered to occur at different timescales, and therefore, have been decoupled (the Born-Oppenheimer approximation).

Now by inserting equation 2.2.6 into equation 2.2.5 and applying the Born-Oppenheimer approximation, we reach this point:

$$\mu_O(T,p) = -\frac{1}{2N}\left[k_B T \ln\left(\frac{1}{N!}(q^{trans})^N\right) - pV\right] + \frac{1}{2}(\mu^{rot} + \mu^{vib} + \mu^{electr} + \mu^{nucl}) \,. \tag{2.2.7}$$

Each type of chemical potential (free energy) in this equation can be investigated as below:

TRANSLATIONAL FREE ENERGY: When dealing with a particle confined within a box, its energy due to center-of-mass motion can be expressed as the equation:

$$\epsilon_k = \frac{\hbar^2 k^2}{2m} \,,$$

where

$$\mathbf{k} = \frac{\pi}{L}(n_x\hat{x} + n_y\hat{y} + n_z\hat{z})$$

is in the classical limit. The size of the box is characterized by $L = V^{1/3}$, where V is the volume of the box. The mass of one particle is denoted by m, and x, y, and z are unit vectors in the three Cartesian directions, while $n_{x/y/z}$ are integers that range from 1 to ∞. As the box size approaches infinity ($L \longrightarrow \infty$), the one-particle partition function reaches equation

$$q^{trans} = V\left(\frac{2\pi m k_B T}{h^2}\right)^{3/2}$$

in the thermodynamic limit.

ROTATIONAL FREE ENERGY: In the rigid rotator approximation, the rotational partition function can be expressed as follows:

$$q^{rot} = \sum_{j=0}^{\infty}(2J+1)\exp\left(\frac{-J(J+1)B_o}{k_B T}\right) \,.$$

Here, J is the rotational quantum number, and $B_o = \frac{\hbar^2}{2I}$ represents the rotational constant, in which I denotes the moment of inertia that mainly depends on the mass and equilibrium bond lengths. However, in the case of homonuclear diatomic molecules like O_2, where there

are multiple indistinguishable orientations, the partition function becomes a bit complicated, as it is linked to the nuclear spin degrees of freedom, and the total wave function must be anti-symmetric under exchange of the indistinguishable particles. To simplify, we can use a classical symmetry number σ^{sym} to indicate the number of indistinguishable orientations that the molecule can have (e.g., 1 for heteronuclear diatomic molecules and 2 for homonuclear diatomic molecules) at the temperatures of our interest. When the spacing of the rotational levels is small in comparison to $k_B T$, the sum in q^{rot} can be transformed into an integral using the Euler-Maclaurin series. Consequently,

$$\mu^{rot} \approx -k_B T \ln\left(\frac{k_B T}{\sigma^{sym} B_o}\right)$$

is obtained. It is important to note that this formula is only valid for linear molecules, where only B_o is considered. In more complex cases, one would need to diagonalize the inertial tensor and consider all three eigenvalues quantity A_o, B_o, and C_o.

VIBRATIONAL FREE ENERGY: To calculate the vibrational contribution, the partition function is written in the harmonic approximation by summing up all the M fundamental modes of ω_i of the particle. This results in

$$q_{vib} = \sum_{i=1}^{M} \sum_{n=0}^{\infty} \exp\left(\frac{-(n+\frac{1}{2})\hbar\omega_i}{k_B T}\right).$$

By solving the geometric series,

$$\mu^{vib} = E^{ZPE} + \Delta\mu^{vib}$$

is obtained. The term E^{ZPE} comes from zero-point vibrations. Then the quantity μ^{vib} can be written as:

$$\sum_{i=1}^{M} \left[\frac{\hbar\omega_i}{2} + k_B T \ln\left(1 - \exp\left(\frac{\hbar\omega_i}{k_B T}\right)\right)\right].$$

ELECTRONIC AND NUCLEAR-FREE ENERGY: In most molecules, the internal energy levels are much higher than the thermal energy, so only the ground state significantly contributes to the partition function. Considering the spin degeneracy of the ground state (I^{spin}) and the total energy of the O_2 molecule ($E^{tot}_{O_2}$), electronic chemical potential can be represented by:

$$\mu^{electr} \approx E^{tot}_{O_2} - K_B T \ln\left(I^{spin}\right).$$

The nuclear degrees of freedom, having larger energy separations, are even more confined to the ground state. However, since the nuclear state remains largely unchanged in chemical processes, it is not considered in the thermodynamic changes discussed here [102].

IN RESULTS OF ALL THESE CONSIDERATIONS AND SIMPLIFICATIONS: Now, we can substitute the parameters of equation 2.2.7 with the above results. Inserting q^{trans} into the first term on the right-hand side of the equation 2.2.7, results in:

$$-\frac{1}{2}k_BT\ln\left[\left(\frac{2\pi m}{h^2}\right)^{3/2}\frac{(k_BT)^{5/2}}{p}\right]. \tag{2.2.8}$$

Note that we employed the ideal gas law $pV = Nk_BT$ and the Stirling formula ($\ln N! = N\ln N - N$). Then by inserting 2.2.8 and the formulas that were obtained above for μ^{rot}, μ^{vib}, μ^{electr}, and μ^{nucl} into equation 2.2.7, we obtain:

$$\mu_O(T,p) = \frac{1}{2}E^{tot}_{O_2} + \frac{1}{2}E^{ZPE}_{O_2} + \Delta\mu_O(T,p)\,, \tag{2.2.9}$$

where

$$\begin{aligned}\Delta\mu_O(T,p) = -\frac{1}{2}k_BT\Bigg\{&\ln\left[\left(\frac{2\pi m}{h^2}\right)^{3/2}\frac{(k_BT)^{5/2}}{p}\right] + \ln\left(\frac{k_BT}{\sigma^{sym}B_o}\right)\\ &-\ln\left[1-\exp\left(\frac{\hbar\omega_0}{k_BT}\right)\right] + \ln\left(I^{spin}\right)\Bigg\}\,.\end{aligned} \tag{2.2.10}$$

On the other hand, equation 2.2.10 reveals that it is possible to rewrite equation 2.2.9 in a different way, as shown as follows:

$$\mu_O(T,p) = \frac{1}{2}E^{tot}_{O_2} + \frac{1}{2}E^{ZPE}_{O_2} + \Delta\mu_O(T,p^0) + \frac{1}{2}k_BT\ln\left(\frac{p}{p^0}\right)\,. \tag{2.2.11}$$

Note that, by utilizing equation 2.2.11, it becomes possible to determine $\Delta\mu_O(T,p)$ by referring to tabulated enthalpy and entropy values at standard pressure $p^0 = 1$ atm, instead of relying on equation 2.2.10. Both approaches yield similar results for oxygen, but for more complex molecules the choice of method depends on the availability of gas phase data [102].

Gibbs free energy of solid bulk and surface

We decompose the solid phase Gibbs free energies into different terms

$$G = E^{total} + F^{vib} + F^{conf} + pV\,,$$

including total energy, vibrational free energy, and configurational free energy, respectively. The focus is on relative values rather than absolute values, allowing for potential error cancellation. The main term is the total energy, obtained through accurate DFT calculations. The approach used, known as *ab initio* atomistic thermodynamics, leverages the predictive power of first-principles techniques to evaluate total energy contributions for finite temperature and pressure conditions.

Moreover, the contribution of certain terms in Gibbs free energy (decomposed version) to the surface free energy is found to be negligible compared to other significant free energy terms. The PV-contribution, arising from pressure and volume, is on the order of 10^{-3} $meV/Å^2$, which is much smaller than the tens of $meV/Å^2$ magnitude of the remaining terms. The vibrational contribution can be handled using a similar approach, as of the gas phase chemical potential (same harmonic approximation) but with the introduction of the phonon density of states (DOS) rather than discrete fundamental modes (ω_i). Therefore, the vibrational contribution of free energy reads as:

$$F^{vib} = \int d\omega F^{vib}(\omega, T)\sigma(\omega) \, , \tag{2.2.12}$$

where $\sigma(\omega)$ is phonon density of states and $F^{vib}(\omega, T)$ is:

$$F^{vib}(\omega, T) = \frac{\hbar\omega}{2} + k_B T \ln\left(1 - \exp\left(\frac{\hbar\omega}{k_B T}\right)\right) .$$

To accurately estimate the impact of vibrations on γ (which is also called ΔG_{ad}), we need to calculate the phonon DOS for the bulk and surface of the material. This information is contained in the PES and can be obtained using DFT. However, surface phonon DOS calculations can be computationally demanding. Alternatively, we can focus on the difference in vibrational free energy between the bulk and surface, which is crucial for determining quantities like the Gibbs free energy of adsorption. Therefore, for a system with N_O oxygen atoms and N_M metal atoms, we have:

$$\Delta F^{vib,ad} \approx -\frac{1}{A}\Bigg[\int d\omega F^{vib}(\omega, T)(\sigma(N_O, N_M, \omega) - \sigma_{clean}(0, N_M, \omega) - (N_M - N_M')\sigma_M(\omega))\Bigg] - \frac{N_o}{2}E_{O_2}^{ZPE} \, . \tag{2.2.13}$$

In the equation above, N_M' is for considering the possibility of changing the number of metal atoms for the clean surface after oxidization, σ represents the phonon DOS of the surface, σ_{clean} corresponds to the phonon DOS of the clean surface, and σ_M denotes the phonon DOS of the metal bulk. This equation can be exact by substituting $(N_O/2) \times E_{O_2}^{ZPE}$ with $(N_O/2) \times \mu_{O_2}^{vib}$, however, it has been observed that the temperature-dependent vibrational contribution to $\mu_{O_2}^{vib}(T)$ is negligible [102]. We should notice the importance of accurately evaluating the vibrational contribution to the Gibbs free energy of adsorption on surfaces. The phonon DOS of the surface and bulk are crucial in determining this contribution, and although surface phonon DOS calculations are computationally demanding, simpler approximations can be used to estimate the vibrational contribution.

One such approximation is the Einstein model, which considers only one characteristic frequency for each atom type. However, it is important to note that neglecting the vibrational contribution may not always be appropriate and there may be cases where an explicit calculation of the surface and bulk phonon DOS is required (e.g. the case of the adsorption of larger molecules [74] or in hydrogen-containing environments [120]).

The remaining term to be considered is the configurational free energy, which poses significant computational challenges due to the vast configuration space of surface structures. Traditional statistical mechanics methods, such as Monte Carlo simulations [35], are designed to sample this space efficiently, but their direct integration with electronic structure theories requires an impractically large number of free energy evaluations [101]. To overcome this obstacle, a strategy is employed to map the real system onto a simplified model system with a computationally tractable Hamiltonian. However, uncertainties arise regarding the accuracy of the model system representation and the determination of its parameters from first-principles calculations. Nevertheless, this approach offers valuable insights and an understanding of the underlying mechanisms. In cases where a lattice can describe the system and define the possible adsorption sites, lattice-gas Hamiltonians (LGHs) or cluster expansions (CEs) serve as notable examples of such mapping techniques [101].

Jutta Rogal and Karsten Reuter proposed a simpler approach [102] for studying surface structures by comparing their stability based on surface free energies or Gibbs free energies of adsorption. This method involves screening a number of known or relevant ordered structures and considering the influence of defects on configurational entropy[3]. By estimating the configurational entropy contribution using a small number of defects in the system, they determined its impact on the Gibbs free energy. However, this direct screening approach has limitations as it relies on the considered configurations and cannot predict unexpected surface geometries or stoichiometries. Nonetheless, it serves as a valuable tool for quickly comparing the stability of different structural models and gaining insights into important structural motifs. To address phase coexistence and

3 At sufficiently low temperatures, the remaining configurational entropy per surface area is primarily attributed to a small number of defects in these ordered structures. An estimation of this entropy can be obtained as:

$$\frac{TS^{conf}}{NA} = \frac{k_B T}{A} \ln\left[\frac{(N+n)!}{N!n!}\right],$$

where n represents the number of defects in a system with N surface sites ($n << N$).

order-disorder transitions more comprehensively, proper sampling of the configurational space is necessary.

2.2.2 Recap and use in practice: Free energy plots and surface phase diagrams

One can apply the thermodynamic framework explained earlier to analyze the structure and composition of a solid surface in contact with an environment at finite temperature and pressure. To dive into the practical discussion, we will exclude the vibrational contribution and neglect the configurational entropy term in the solid phase Gibbs free energies based on previous reasoning and consideration. This simplification leads the preliminary equation 2.2.4 to the following working equation:

$$\Delta G_{ad}(T,p) \approx -\frac{1}{A}(E^{total}(N_O,N_M) - E^{total}(0,N_M) - (N_M - N'_M)E^{total}_M - \frac{N_O}{2}E^{total}_{O_2} - N_O\Delta\mu_O(T,p)) \; . \quad (2.2.14)$$

In the direct screening approach of *ab initio* atomistic thermodynamics, the Gibbs free energy of adsorption can be calculated by comparing the total energies of different surface structural models. By plotting the Gibbs free energy against the oxygen chemical potential (illustrated for our system in Fig. 3.5 and Fig. 4.3 - upper panels), the most stable model can be identified. This information can be represented in either free energy plots or surface phase diagrams (the same figures - lower panels), providing insights into the stability of different surface phases under specific (T,p) conditions. Both types of plots convey the same information; the surface phase diagrams give a direct understanding of experimental conditions and the free energy plots offer additional information about the energetic differences between surface models. The phase boundaries in surface phase diagrams exhibit similar curvatures based on lines of constant $\Delta\mu_O$.

2.3 AB INITIO LATTICE DYNAMICS: DFPT

Density Functional Perturbation Theory (DFPT) is a powerful extension of density functional theory (DFT) that enables the investigation of the vibrational properties of materials. It provides a comprehensive framework for calculating the phonon frequencies, infrared and Raman spectra, and other vibrational properties, which are crucial for understanding the lattice dynamics and thermal behavior of materials.

In DFPT, the starting point is the equilibrium electron density obtained from DFT calculations. By perturbing the system through small atomic displacements, DFPT allows us to determine how these perturbations affect the total energy and forces acting on the atoms. This information is then used to compute the dynamical matrix, which characterizes the interatomic force constants and provides a basis for calculating vibrational properties.

The key advantage of DFPT is its ability to calculate vibrational properties in a computationally efficient manner. Instead of performing separate calculations for each atomic displacement, DFPT relies on a first-order expansion of the total energy with respect to the atomic displacements. This significantly reduces the computational cost compared to more rigorous methods, such as a direct solution of the dynamical matrix.

Through DFPT, we gain insights into the vibrational modes and phonon spectra of materials, which are essential for understanding their thermal conductivity, heat capacity, and other thermodynamic properties. Additionally, DFPT enables the interpretation of experimental techniques like infrared and Raman spectroscopy, providing a valuable link between theory and experiment.

In this section, we will explore briefly the theoretical foundations of DFPT, elucidating its mathematical formulations, computational procedures, and applications.

2.3.1 Formalism

Within the framework of the adiabatic approximation, the behavior of the nuclei in a system can be described by considering the potential energy derived from the ground-state total energy E obtained through Density Functional Theory (DFT). In this approximation, the nuclei are assumed to be fixed in their positions R_I while the electrons' configuration is determined.

When considering small displacements from the equilibrium positions, represented by u_I at time t, the position of atom I can be expressed using $R_I + u_I$ instead of R_I. This substitution allows us to track the movement of the nuclei as they deviate from their equilibrium positions.

Expanding the total energy up to the second order, we arrive at the equation below:

$$E(R_I + u_I) = E_0(R_I) + \sum_{I\alpha} \frac{\partial E}{\partial u_{I\alpha}} u_{I\alpha} + \frac{1}{2} \sum_{I\alpha,J\beta} \frac{\partial^2 E}{\partial u_{I\alpha} \partial u_{J\beta}} u_{I\alpha} u_{J\beta} \ , \quad (2.3.1)$$

where the derivatives are evaluated at $u_I = 0$. The variables α and β correspond to the three Cartesian coordinates that define the displacement. This expansion provides insights into the

energy landscape as the nuclei undergo slight deviations from their equilibrium positions.

At the equilibrium state, $\frac{\partial E}{\partial u_{I\alpha}}$ is zero, and the Hamiltonian of the ions denoted as H, can be derived based on the energy expression:

$$H = \sum_{I\alpha} \frac{P_{I\alpha}^2}{2M_I} + \frac{1}{2} \sum_{I\alpha,J\beta} \frac{\partial^2 E}{\partial u_{I\alpha} \partial u_{J\beta}} u_{I\alpha} u_{J\beta} \, , \tag{2.3.2}$$

which captures the relationship between the momenta $P_{I\alpha}$ and the mass M_I of the nuclei.

Applying Hamilton's equations ($\dot{u}_{I\alpha} = \frac{\partial H}{\partial P_{I\alpha}}$ and $\dot{P}_{I\alpha} = -\frac{\partial H}{\partial u_{I\alpha}}$), which describe the time evolution of a system, we can obtain the equations of motion for the nuclei. They lead to:

$$M_I \ddot{u}_{I\alpha} = \sum_{J\beta} \frac{\partial^2 E}{\partial u_{I\alpha} \partial u_{J\beta}} u_{J\beta} \, , \tag{2.3.3}$$

which reveals the dynamics of the nuclei within the system. In the equation 2.3.3, we seek $N \times 3N_{at}$ solutions $u_{I\alpha}(t)$, where N_{at} represents the number of atoms. These solutions, corresponding to phonons, can be expressed as shown in the equation:

$$u_{\mu s\alpha}(t) = \frac{1}{\sqrt{M_s}} Re[u_{s\alpha}^{\nu}(q) \times \exp(i(qR_\mu - \omega_{q\nu} t))] \, , \tag{2.3.4}$$

where s is the atom in the cell μ (denoted before by I) and ν denotes the modes. Here, the angular frequency of a lattice vibration at wave vector q and mode ν is represented by $\omega_{q\nu}$, while $u_{s\alpha}^{\nu}(q)$ denotes the complex amplitude of the phonon mode.

Substituting equation 2.3.4 into equation 2.3.3 yields:

$$\omega_{q\nu}^2 u_{s\alpha}^{\nu}(q) = \sum_{s'\beta} D_{s\alpha s'\beta}(q) u_{s'\beta}^{\nu}(q) \, , \tag{2.3.5}$$

where $D_{s\alpha s'\beta}(q)$ represents the dynamical matrix of the solid:

$$D_{s\alpha s'\beta}(q) = \frac{1}{\sqrt{M_s M_{s'}}} \sum_{\eta} \frac{\partial^2 E}{\partial u_{\mu s\alpha} \partial u_{\eta s'\beta}} \exp(iq(R_\eta - R_\mu)) \, . \tag{2.3.6}$$

To calculate the second derivative of the total energy in equation 2.3.6, we can utilize the Hellmann-Feynman theorem, which provides an expression for the first derivative with respect to the external parameter λ, as shown in the equation below:

$$\frac{\partial E}{\partial \lambda} = \int \frac{\partial V_{ext}}{\partial \lambda} \rho(r) d^3 r + \frac{\partial U_{II}}{\partial \lambda} \, . \tag{2.3.7}$$

Differentiating equation 2.3.7 with respect to a second parameter μ allows us to obtain the second derivative, as demonstrated below:

$$\frac{\partial^2 E}{\partial \mu \partial \lambda} = \int \frac{\partial^2 V_{ext}}{\partial \mu \partial \lambda} \rho(r) d^3 r + \int \frac{\partial V_{ext}}{\partial \lambda} \frac{\rho(r)}{\partial \mu} d^3 r + \frac{\partial^2 U_{II}}{\partial \mu \partial \lambda} \, . \tag{2.3.8}$$

The external parameters λ and μ correspond to the displacements of the atoms. To compute equation 2.3.8, we need to consider not only the electronic charge density $\rho(r)$ but also its linear response to a change in the nuclear geometry, as expressed in equation below:

$$\frac{\partial \rho(r)}{\partial \mu} = 2 \sum_{kv} \left[\frac{\partial \psi^*_{kv}(r)}{\partial \mu} \psi_{kv}(r) + \psi^*_{kv}(r) \frac{\partial \psi_{kv}(r)}{\partial \mu} \right] . \tag{2.3.9}$$

Evaluating the derivative $\frac{\partial \psi_{kv}(r)}{\partial \mu}$ involves linearizing the Kohn-Sham potential V_{KS}, the single-particle wavefunctions ψ_{KS}, and the eigenvalues ϵ_{KS} with respect to the perturbation μ. Therefore:

$$V_{KS}(r, \mu) = V_{KS}(r, \mu)\Big|_{\mu=0} + \frac{\partial V_{KS}}{\partial \mu} \mu \, , \tag{2.3.10}$$

$$\psi_{KS}(r, \mu) = \psi_{KS}(r, \mu)\Big|_{\mu=0} + \frac{\partial \psi_{KS}}{\partial \mu} \mu \, , \tag{2.3.11}$$

$$\epsilon_{KS}(\mu) = \epsilon_{KS}(\mu)\Big|_{\mu=0} + \frac{\partial \epsilon_{KS}}{\partial \mu} \mu \, . \tag{2.3.12}$$

By substituting these equations into the Kohn-Sham equation (equation 2.1.10) and considering only the first order in μ, we obtain:

$$\left[-\frac{1}{2}\nabla^2 + V_{KS} - \epsilon_{kv} \right] \frac{\partial \psi_{kv}(r)}{\partial \mu} = -\frac{\partial V_{KS}}{\partial \mu} \psi_{kv}(r) + \frac{\partial \epsilon_{kv}}{\partial \mu} \psi_{kv}(r) \, , \tag{2.3.13}$$

which implies the charge density dependency through KS potential as:

$$\frac{\partial V_{KS}}{\partial \mu} = \frac{\partial V_{xc}}{\partial \mu} + \frac{\partial V_H}{\partial \mu} + \frac{\partial V_{ext}}{\partial \mu} \, .$$

These clauses, in turn, depend self-consistently on the charge density induced by the perturbation.

It has been demonstrated that the induced charge density solely depends on $P_c \frac{\partial \psi_{kv}}{\partial \mu}$, where P_c represents the projection onto the conduction bands. As a result, the linear system described in equation 2.3.13 can be reformulated as shown below:

$$\left[-\frac{1}{2}\nabla^2 + V_{KS} - \epsilon_{kv} \right] P_c \frac{\partial \psi_{kv}(r)}{\partial \mu} = -P_c \frac{\partial V_{KS}}{\partial \mu} \psi_{kv}(r) \, . \tag{2.3.14}$$

Considering all the above, the response to the charge density can be expressed as follows:

$$\frac{\partial \rho(r)}{\partial \mu} = 2 \sum_{kv} \left[\left(P_c \frac{\partial \psi_{kv}(r)}{\partial \mu} \right)^* \psi_{kv}(r) + \psi^*_{kv}(r) P_c \frac{\partial \psi_{kv}(r)}{\partial \mu} \right] . \tag{2.3.15}$$

By obtaining the response to the charge density, we can calculate the dynamical matrix 2.3.6 and the second derivatives of the energy

2.3.8, enabling the determination of the phonon frequencies. This method, known as density-functional perturbation theory (DFPT) [6], is commonly employed to obtain the linear response of the electron density within DFT.

In summary, this section provided a brief background explanation of DFPT. However, to dive into details of polar semiconductors' phonon dispersion, it needs extra consideration. These materials have unique properties related to LO-TO splitting at the Γ point, which requires considering the concept of born effective charge (reference: [41]). This topic is not within the scope of this chapter, it will be discussed in a later section.

Additionally, for more information and modifications specific to dealing with metals, please refer to the relevant reference [6].

2.4 STRUCTURAL PREDICTION

Nowadays, structural prediction methods are important in many fields, including biochemistry, biology, and medicinal chemistry. They continue to be refined and improved, with new approaches and techniques being developed to better understand the structures and functions of materials such as biological molecules.

In the 1950s, Linus Pauling and Robert Corey proposed the first three-dimensional models of proteins based on their amino acid sequences. This work laid the foundation for the field of protein structure prediction[88]. Cyrus Levinthal (1968) proposed the "Levinthal paradox," which stated that the number of possible conformations of a protein is too large to be explored by brute force methods [65]. This helped to motivate the development of more efficient approaches to protein structure prediction. The first protein structure prediction algorithms were developed based on the SOLVE and COMPASS methods. These early approaches relied on heuristics and simple energy functions to guide the search for protein structures.

The first *ab initio* protein structure prediction methods were developed by using more complex energy functions and Monte Carlo sampling to search for protein structures [49]. In the first decade of the 21st century, machine learning methods began to be applied to protein structure prediction [3], leading to significant improvements in accuracy and efficiency. In the 2010s, structural prediction methods continued to evolve, with the development of new approaches for predicting the structures of RNA molecules, protein-ligand interactions, and protein-protein interactions.

Structural prediction methods for crystals are used to predict the arrangement of atoms in a crystal, which also can be determined by X-ray crystallography experimentally. However, the experimental

technique can be time-consuming and costly and is not always practical for all materials. On the other side, any detailed computational study must start from atomic configurations close in energy to the global minimum structure. Finding this global minimum structure within a reasonable amount of computational time and effort is still a significant challenge. If we suppose a system including N atoms, we need a 3N-dimensional vector for describing the atomic positions. As it is mentioned before, the potential energy of the system (N atoms) as a function of their position is known as the potential energy surface (PES). Finding the global minimum structure of a set of atoms is thus equivalent to finding the lowest energy point on the PES [129]. Since atomic forces are strongly nonlinear functions of the atomic coordinates, the number of local minima scales exponentially with N, and therefore only for a very limited number of simplified models, the global minimum can be computed analytically. This is the reason why different sophisticated methods and algorithms come into play.

There are several different approaches to crystal structure prediction (i.e. finding the global minimum on the PES). These algorithms can be divided into thermodynamically motivated methods and evolutionary ones. Also, the thermodynamic algorithms can be divided into two well-known approaches, molecular dynamics, and Monte Carlo. The molecular dynamics approach follows a temporal evolution of the atoms at a given temperature, and then lowering the temperature can be used to condensate to the hypothetical global minimum structure [19]. The other approach is the "Basin Hopping method" which is based on a Metropolis sampling technique, random displacements, and relaxations (Monte Carlo algorithm) [131].

On the other hand, the evolutionary genetic algorithm is based on a population of candidates that are evolved through mutual pairing [129]. This method uses a process of natural selection, crossover, and mutation to generate and optimize crystal structures.

The other very recent branch of these types of study is machine learning methods. These methods use artificial neural networks and other machine learning techniques to predict crystal structures based on data from known materials [77].

2.4.1 Genetic Algorithm Method

As mentioned, a genetic algorithm (GA) is a type of optimization algorithm that is inspired by the process of natural evolution. It is commonly used to find solutions to problems that are too complex to be solved by traditional algorithmic approaches.

In general, GA works by starting with a population of possible solutions (called "individuals" or "chromosomes") and iteratively improving them through a process of selection, crossover, and mutation. Selection involves choosing the most fit individuals from the current population to be parents for the next generation. Crossover involves combining the genetic material of the selected individuals to create offspring that inherit characteristics from both parents. Mutation involves introducing random changes to the genetic material of the offspring to introduce diversity into the population. These steps are repeated until the algorithm converges on a satisfactory solution or until a predetermined number of iterations have been reached.

The main idea is that, in each generation, the total energy of individuals in the population will be calculated, and then they are ordered based on their energies. The most stable individuals are considered parents for the next generation. We should notice that finding the most stable individuals can be done by employing empirical potentials [5] or by employing first-principles methods [2]. In other words, GA is searching all the possible minima in the free energy surface of the system.[4] Using cheap methods (i.e. empirical potentials in molecular dynamics) to approximate free energy leads to a misguided search. On the other hand, *ab initio* free energy calculations are highly accurate but computationally expensive.

Since we want to reach a reliable result compatible with experimental outcomes, *ab initio* calculation of free energy is more favorable. After a careful look, the well-established code to reach our desirable accuracy is USPEX (Universal Structure Predictor: Evolutionary Xtallography). A very brief introduction of this code and its features are listed below [85]:

- USPEX uses the negative of the *ab initio* free energy of the locally optimized structure as fitness value, considered as the evaluation function.
- It features three different variation operators: heredity, mutation, and permutation.
- Every produced candidate is scaled to a certain unit cell volume, V_{UC}, prior to testing against hard constraints and to local optimization.
- Local optimization can be found based on *ab initio* free energy comparison. Although this step increases the cost of each individual, it reduces the search space to the local optima, enhances comparability between different structures, and provides locally optimal structures as well.

4 Free energy comes from potentials in a computational context. So speaking about free energy surface is equal to considering interatomic potentials.

- Different high-pressure exposure is possible (suitable for structural prediction in experimentally unreachable conditions).
- Reliable interface with other codes, such as Quantum ESPRESSO, VASP, LAMMPS, etc.

Taking advantage of using this code, interfaced with Quantum ESPRESSO, we are able to find some new configurations of the subjected system.

3 PRISTINE BOROPHENE ON AL(111)

The best that most of us can hope to achieve in physics is simply to misunderstand at a deeper level. —– Wolfgang Pauli.

3.1 INTRODUCTION

2D boron allotropes are attracting increasing attention due to their promising electronic and chemical properties [80, 140]. 2D metallicity, massless Dirac fermions [151], charge-density waves, superconductivity, and zero-tunneling barriers are some of the properties that make these materials extremely attractive for applications in the fields of quantum electronics, energy storage, catalysis, and sensing [72, 80]. Since the specific electron-phonon coupling characteristic of the (honeycomb) 2D B layers in borides accounts for the observed superconductive properties [37, 142], pure B materials would potentially pave the way to the design of boron-based 2D superconducting structures. In addition, interesting (photo)-catalytic properties of B-based monolayers have been reported for the hydrogen evolution reaction, a strategic reaction in the field of green hydrogen energy [148], and in the case of carbon dioxide reduction for the synthesis of energy vectors [71].

Many of these previous statements are closely related to the electronic properties of a honeycomb 2D structure, whose stability in the case of borophene is however compromised by the electron deficiency of boron with respect to carbon. Ever since the first theoretical studies on borophene have appeared [80, 92, 138, 152], it became apparent that this instability could be leveraged to tune its geometric, electronic, and chemical properties through self-doping, whereby the addition of an extra B atom to a honeycomb lattice releases three electrons to the planar skeleton [72], thus helping stabilize it.

The variety of structures that can be thus obtained is best described by introducing a *filling parameter* (f), representing the fraction of hexagons hosting an extra boron atom [56]. Correspondingly, the honeycomb structure (hB) is characterized by $f = 0$, while the

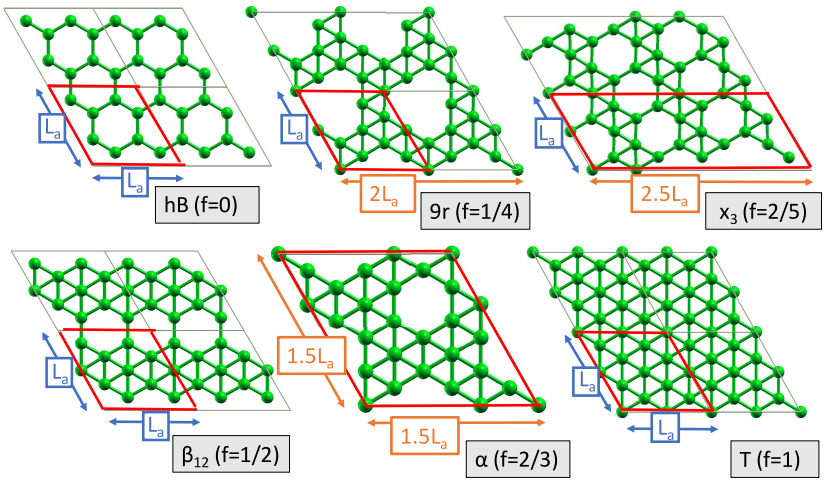

Figure 3.1: Representation of the honeycomb structure (hB) with zero filling factor ($f = 0$), $9r : f = \frac{1}{4}$, $\chi_3 : f = \frac{2}{5}$, $\beta_{12} : f = \frac{1}{2}$, $\alpha : f = \frac{2}{3}$, and the triangular layer (T) with $f = 1$ (scales are in units of L_a = 5.71 Å, which is lattice constant of borophene@Al(111)). The conventional cell of each polymorph is delimited with the red parallelogram.

triangular layer (T) has $f = 1$, representing the two self-doping extremes among a large family of structures ($9r : f = 1/4$, $\chi_3 : f = 2/5$, $\beta_{12} : f = 1/2$, $\alpha : f = 2/3$) (see Fig. 3.1). Most of these polymorphs are metallic and have hexagonal or triangular structures (with the exception of the 9r structure, which displays nonagonal rings), while the bulk boron allotropes are generally semiconducting or insulating [62, 147]. Amongst these structures, free-standing χ_3 and β_{12} were successfully synthesized [97], while 9r and α are also considered as potentially stable without a support [56]. On the other hand, the honeycomb structure attracts the most attention, because of its special features. In this regard, it is our main focus.

A different, less disruptive, way of coping with electron deficiency is by charge transfer from a supporting metal substrate. Indeed, at variance with what is observed for Ag(111) [34, 78], honeycomb borophene (hB) has been successfully grown on an Al(111) termination, providing sufficient charge transfer [69] to stabilize a flat, planar structure. The overlayer-substrate interaction resulting from this charge transfer, however, is so strong that an AlB_2 monolayer is unintentionally formed at the interface [39]. The question then naturally arises as to how the strength of the overlayer-substrate interaction can be tuned. Chemical doping of the interface can provide such a means, namely through oxidation, towards borophene oxide [142, 145, 149] (see chapter 4), or reduction, towards chemically stable borophane phases [67, 83, 111, 135] (see chapter 5).

Although various structures have been theoretically predicted for borophene, the experimental realization of supported borophene appears quite challenging [145]. As a step forward with respect to conventional atomic-layer deposition approaches for B, a possible novel route to the chemical synthesis of 2D B layers has been reported only very recently [25].

The rest of this chapter is organized as follows: in Sec. 3.2 I present a thorough theoretical investigation that combines state-of-the-art electronic structure methods, based on DFT, and novel genetic prediction approaches [85, 153] to find the most stable configuration of borophene, and predict some new (meta)stable phases of borophene on Al(111) (Subsec. 3.2.1), followed by a discussion of the related charge-transfer mechanisms in Subsec. 3.2.2. The discussion will be continued with thermodynamical consideration, to take into account the environmental situation in the synthesizing process (Sec. 3.3). The experimental results, performed by our colleagues, are reported as a complementary section (Sec. 3.4). Finally, the results are summarized in Sec. 3.5. Note that the computational details have been explained in appendix A. Since this chapter involves experimental and theoretical results, looking at appendix B, for a very brief overview of experimental methods and techniques, will help to follow the discussion.

3.2 BOROPHENE ON AL(111)

Al(111) provides a lattice-matched substrate, as well as an electron-charge reservoir, for the growth of the borophene polymorphs examined in the introduction, with the potential of stabilizing the sought-after honeycomb one, hB (see Fig. 3.2) [69].

3.2.1 Structure Prediction of Borophene on Al(111)

In order to find the most stable structures of borophene on Al(111), we have computed the surface energies, e_α, of the polymorphs shown in Fig. 3.2, defined as:

$$e_\alpha = \Big(E_\alpha\big[B@Al(111)\big] - E\big[Al(111)\big] - N_B \times E_b\big[B\big] \Big) \Big/ S, \qquad (3.2.1)$$

where E_α is the total energy, with the label 'α' indicating the polymorph, $E_b[B]$ is the energy per atom of a B bulk crystal, and N_B is the number of B atoms contained in the area S of the surface. We then focused on the stability of the honeycomb structure with respect to other allotropes with the same stoichiometry and ran a thorough structural search using a genetic algorithm (an overview of

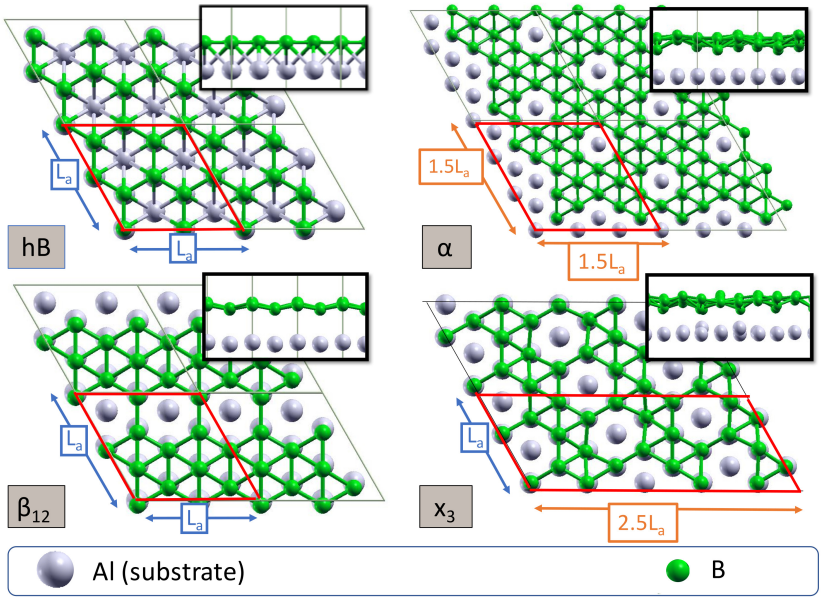

Figure 3.2: The geometrical structure of different borophene polymorphs on Al(111). The double arrows indicate the size of the unit cells, in units of $L_a = 5.71$ Å. The conventional cell of each polymorph is delimited with red parallelogram.

Table 1: Filling factors (FF), boron coverage (BC), and surface energies (e_a with unit $[\ \text{eV} / \text{Å}^2\ ]$) of various borophene polymorphs grown on Al(111). See text for more information.

	hB	α	β_{12}	χ_3	U_1	U_2	U_3	U_4
FF	0	0.666	0.5	0.4	—	—	—	—
BC	2	2.666	2.5	2.4	2	2	2	2
e_a	0.086	0.114	0.096	0.093	0.104	0.113	0.112	0.097

the computational details is presented in appendix A). A summary of our results is presented in Table 1, [1] including four newly discovered polymorphs (dubbed U_n, with $n = 1, \cdots 4$, see Fig. 3.3).

One of the defining features of these new polymorphs is the presence of a variety of polygonal rings (pentagons, octagons, and decagons), besides the triangular, hexagonal, and nonagonal stable configurations. This fact proves that boron is flexible enough to accept a wide variety of combinations of bonding electrons as well. The surface energies, defined in Table 1, equal the static contributions to the surface free energies [100, 108], when the B chemical potential equals its value in the bulk, *i.e.* at growth pT conditions where bulk B is in equilibrium with its own atomic vapor. The positive

1 The table parameters are:
Filling factor, which is the number of filled rings of borophene (visualized in Fig. 3.1), and Boron coverage, which is the ratio of the number of atoms in the B overlayer to the number of Al atoms in the first substrate layer.

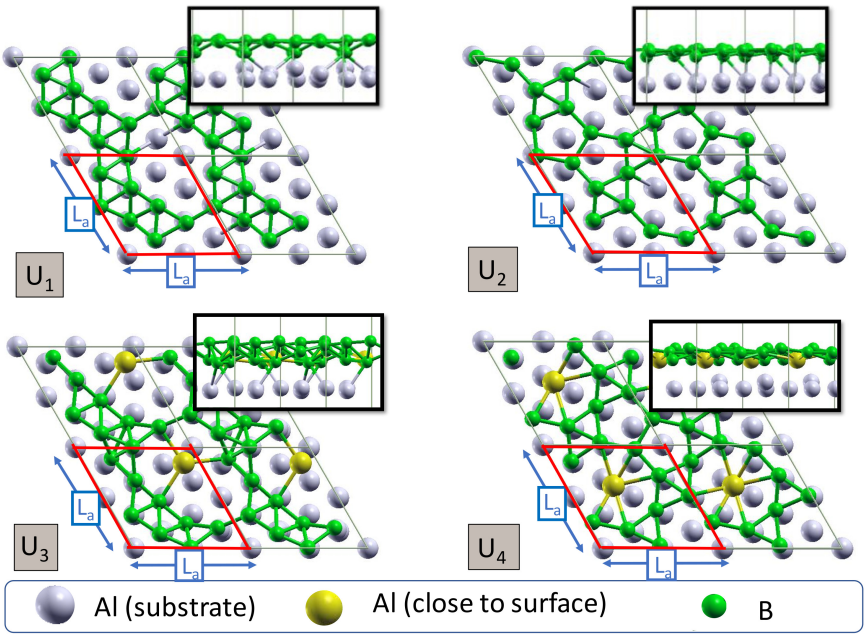

Figure 3.3: Top and side view of U_1, U_2, U_3, and U_4 polymorphs of borophene. The gold color of aluminum is considered to show the aluminum atoms trapped in surface rings, or separate from the substrate and tend to adsorb by surface because of the higher electronegativity of boron (the length scale is $L_a = 5.71$ Å). The conventional cell of each polymorph is determined with red parallelogram.

values of these energies show that the formation of borophene on Al(111) is endothermic; a comparison of the various surface energies indicates that the hB phase (shown in Fig. 3.2) would be favored energetically. More on the stability of various borophene phases on Al(111) at varying growth conditions is presented in Sec. 3.3.

3.2.2 Charge-transfer mechanisms

In order to figure out the charge transfer processes occurring at the B/Al interface and their effects on structural stability and experimental findings, we consider the planar average of the displaced charge distribution of the system, defined as:

$$\Delta\rho(z) = \frac{1}{S}\int_S \left(\rho_{AlB}(\mathbf{r}) - \rho_{Al}(\mathbf{r}) - \rho_B(\mathbf{r})\right) dxdy, \tag{3.2.2}$$

where ρ_{AlB} denotes the electron charge-density of the B@Al(111) system, ρ_{Al} and ρ_B those of the two constituents with their atoms clamped at the positions they would have at the interface, and the integral is performed over planes perpendicular to the growth direction (z).

In Fig. 3.4, we display the planar average of the displaced charge-density distribution, Eq. 3.2.2, for the honeycomb, U_2, and U_4 structures. This charge-displacement pattern can be qualitatively described as resulting from the balance of two effects. The first one is the charge transfer between the aluminum substrate and the more electronegative boron overlayer. The second effect is the formation of chemical bonds between the substrate and the overlayer, which determine a charge accumulation in-between at the expense of charge depletion in the atomic layers. The second effect is larger than the first one, always resulting in a strong charge-accumulation peak in the bonding region[2]. The first effect determines an asymmetry in the charge depletion in the two atomic layers, which is stronger in aluminum than in boron. This asymmetry is greatest in the hB structure and almost vanishes in U_4—as apparent in the figure and from the integrated charges reported in Table 2—thus confirming the stabilizing effect of charge transfer on the hB structure.

2 These regions are determined based on average atomic positions in real space and mapped on Fig. 3.4. It helps to approximate corresponding charge depletion and accumulation with atomic types and bond area.

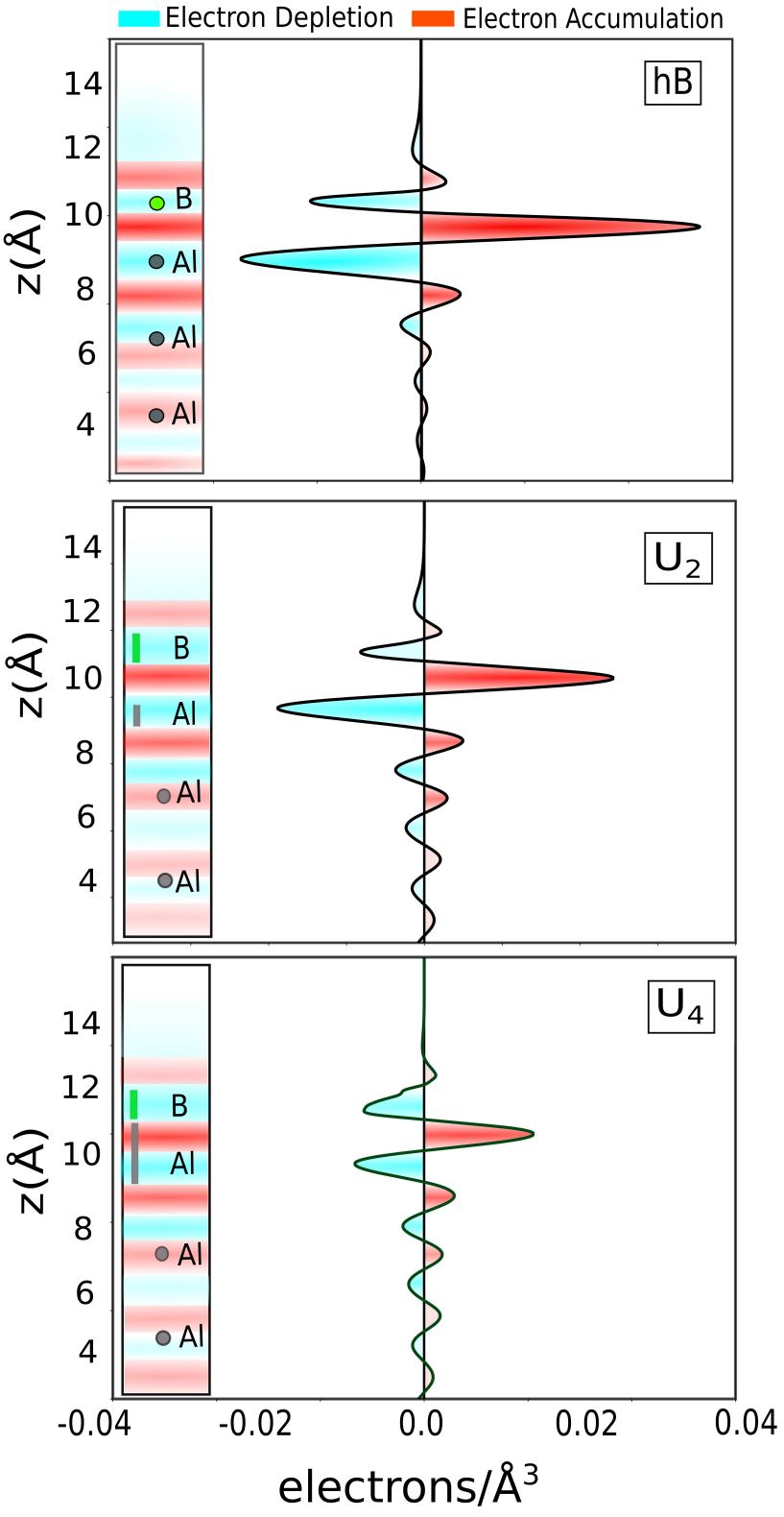

Figure 3.4: Charge density differences between aluminum and borophene in honeycomb phase, U_2, and U_4. The intensity of color associated with higher values, and red and cyan denote electron accumulation and depletion, respectively. The vertical bars next to the chemical symbols of the various elements indicate the spread in the vertical positions of the corresponding atoms.

Table 2: Charge transfer between the Boron and outer Aluminun layers and the bond region in-between (explained in the text) for different B@Al(111) polymorphs, as obtained by integrating the planar averages of the charge-density differences displayed in Fig. 3.4 over the corresponding peaks. Units are milli-electrons/Å^2.

	hB	U_2	U_4
Bond	+20.8	+14.5	+8.2
Boron	−6.1	−3.3	−4.9
Aluminum	−16.9	−12.0	−5.3

3.3 PHASE DIAGRAM FROM *AB INITIO* THERMODYNAMICS

All of the considerations made so far are based on purely energetic arguments and only apply to isolated systems, whose total energy and number of atoms of each chemical species are held fixed. The actual structures observed in an experiment result from a combination of kinetic and thermodynamic effects. While the former is very difficult to model, they are nevertheless driven by the tendency towards thermodynamic equilibrium between the sample and its environment (essentially, the vapor present in the growth chamber), with which it can exchange atoms and heat. In order to account for these effects, we make use of concepts from *ab initio thermodynamics*, a methodology made popular by Scheffler and co-workers in the late nineties [100, 102].

In a nutshell, the thermodynamically stable structure is the one that—for given values of temperature, T, and chemical potential of each atomic species, μ_X—minimizes the surface (grand) free energy per unit area. At equilibrium, the chemical potentials of the various elements at the surface should equal those in the vapor phase. Assuming an ideal-gas law, which always holds at low pressure, the chemical potential of the atomic species X reads $\mu_X(p,T) = \mu^\circ(T) + k_B T \log(p/p^\circ)$, where p° is the pressure at *standard conditions* (*e.g.* the pressure at which the vapor is in equilibrium with the bulk or some specific surface structure at a given temperature) and $\mu^\circ(T) = \mu(p^\circ, T)$ the corresponding chemical potential. A commonly adopted approximation is to neglect the vibrational contribution to the surface free energy, so that *e.g.* the surface grand free energy of polymorph α in the absence of oxygen reads:

$$\varphi_\alpha(\mu_B) = e_\alpha - n_B \mu_B, \tag{3.3.1}$$

where e_α is the polymorph's surface energy per unit area, Eq. (3.2.1), n_B the number of B atoms per unit area, and the B chemical potential

is referred to the B vapor in the growth chamber, which is supposed to be in equilibrium with its own bulk (this implies that we take the bulk thermodynamic parameters in our calculation as the reference). The reference data for the B chemical potential entering Eq. (3.3.1) are taken from Ref. [122].

In the upper panel of Fig. 3.5, we display the adsorption free energy per unit area, Eq. (3.3.1), of various borophene polymorphs grown on Al(111), as a function of the B chemical potential. Energies are referred to that of the hB allotrope, whereas the B chemical potential is referred to its bulk value. According to these data, the hB polymorph is dominant at low chemical potential. Then, at intermediate chemical potential ($\mu_B \simeq 0.13$ to 0.77 eV), the β_{12} phase becomes dominant, whereas the α structure of B@Al(111) is formed when the B concentration further increases, *e.g.* at even higher chemical potential. The lower panel of Fig. 3.5 reports the p-T phase diagram obtained with the method used by Molinari *et al.* [81] and implemented in the Surfinpy package [121]. Since the phase diagram only shows the most stable structures, other local minima in configuration space have no chance to show off, but their relative stability is relevant to understanding the mechanisms determining the structures observed experimentally, and thus worth studying. The lower panel of Fig. 3.5 summarizes these findings in a phase diagram with respect to pressure and temperature. The lower panel reports the phase diagram of borophene on Al(111) deduced from these data. While the relevance of these data to the growth of B on Al(111) is limited by both the overall accuracy of the theoretical calculations and the actual growth conditions [1] (which are certainly far from thermodynamical equilibrium), our results indicate that at low temperature and pressure, there exists a window of thermodynamical stability of the hB phase.

3.4 EXPERIMENTAL OVERVIEW

Disclaimer: The experimental work was performed by our colleagues at the Elettra synchrotron-radiation center and the University of Trieste.

To produce borophene in a laboratory setting, elemental boron can be deposited onto the pristine Al(111) surface under ultra-high vacuum (UHV) conditions. The process involves heating the Al(111) surface to 500 K and applying physical vapor phase deposition techniques. This methodology follows a previously established procedure for borophene synthesis [39, 69, 96].

A distinct pattern of Low-Energy Electron Diffraction (LEED) is achieved, as shown in Figure B.2 (b,c). The pattern clearly displays

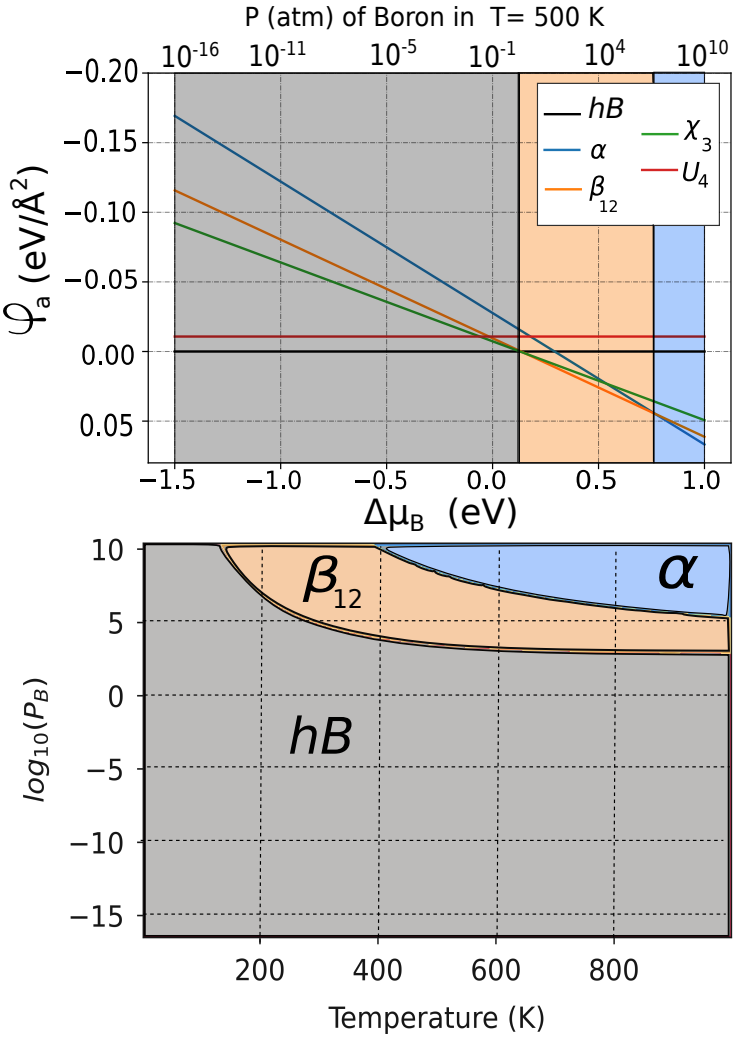

Figure 3.5: Upper panel: dependence of the surface grand free energy (Eq. (3.3.1)) on the B chemical potential, for various borophene allotropes grown on Al(111). The hB surface energy and the B chemical potential of the bulk are taken as references. Lower panel: phase diagram of borophene on Al(111). Temperature is expressed in Kelvin and pressure in bar .

the Al(111) surface, the honeycomb boron phase, and the Moiré coincidence lattices, in line with the $(24 \times 24)/(25 \times 25)$ unit cells ratios between the AlB_2 superstructure and the underlying metal surface (inset of Fig. B.2). For best clarity, here is a selected LEED pattern where a contribution from a second B layer, rotated by 30° with respect to the hB phase, is also present. Indeed, the growth of the second layer starts before completion of the hB monolayer and, depending on the selected absolute B surface coverage, a certain contribution can be therefore expected (Fig. B.2 (c))[3].

The corresponding B 1s (Fig. B.4 column (a) middle row) and Al 2p (Fig. B.4 column (b) middle row) X-ray Photoelectron Spectroscopy (XPS) core level spectra perfectly agree both qualitatively and quantitatively with previously published data [96]. The B 1s spectrum reveals the presence of three components at $B_1 = 187.76$ eV as the main component, $B_2 = 187.47$ eV (with -0.29 eV difference compared to B_1), and $B_3 = 187.10$ eV (with -0.66 eV difference compared to B_1), associated respectively with honeycomb boron of the AlB_2 layer in close contact with the Al(111) substrate, with the topmost AlB_2 layer elevated due to the presence of a B underlayer, and with the B underlayer itself. A minor contribution may be present at 188.46 eV (with $+0.70$ eV difference compared to B_1) and ascribed to residual oxygen contamination (of the order 1% ML) interacting with B atoms.

Consistently, the Al 2p region (Fig. B.4 column (b) middle row) is characterized by three spin-orbit doublets (separation of 0.41 eV) with the $2p_{3/2}$ components at 72.70, 73.30, and 73.92 eV associated with bulk Al, interface, and topmost AlB_2 layers, respectively. In Fig. B.4 column (b) middle row, the best fit was obtained globally on an extended data set that included spectra collected with photon energies ranging from 145 to 155 eV. In order to reduce the number of degrees of freedom, important constraints were imposed on the fitting parameters, yielding solid results even in the framework of a model. In particular, the spin-orbit split energy was globally optimized (0.41 eV) and the $2p_{1/2}$ to $2p_{3/2}$ intensity ratios were fixed to 1:2. Also the lineshape was globally optimized (Lorentzian width, asymmetry parameter) while the Gaussian width was optimized separately for the main (bulk) and B-related components. The best fit for Gaussian and asymmetry parameters are different for the pristine and hydrogenated AlB_2 components (the hydrogenated case will be investigated in chapter 5). Finally, it was not possible to resolve with statistical significance any clean Al surface and B-Al interface component close to the main feature at 72.70 eV. The fit of the bare hB/Al(111) spectra is in full agreement with previous literature [96].

3 As it is utilized in theoretical part, the B coverage expressed in ML (monolayers) is referred to the terminal Al(111) surface, where 1 ML corresponds to one B ad-atom for each surface Al atom.

Furthermore, the Near-Edge X-ray Absorption Fine Structure (NEXAFS) spectra at the B edge (Fig. B.4 column (c) middle row) are in agreement with the previous report [96], while the intensity below 191.3 eV is associated with transitions from the B 1s level to unoccupied π^* states, a distinct feature is observed at 188.0 eV due to the specific $1s \longrightarrow 2p(\pi^*)$ resonance. Sigma transitions are visible above 191.3 eV, with a sharp $1s \longrightarrow 2p(\sigma^*)$ feature at 192.4 eV, yielding an overall $\pi^* - \sigma^*$ energy separation of 4.4 eV.

When probed by means of InfraRed-Visible Sum-Frequency Generation (IR-Vis SFG) vibronic spectroscopy, the bare hB layer on Al(111) does not contribute with any resonant signal ascribable to its internal vibrational modes (Fig. B.3 middle curve), either in ppp or ssp polarization configurations. Keeping in mind that the technique, on metal, is sensitive exclusively to the dipole components normal to the surface.

3.5 CONCLUSIONS

By combining *ab initio* methods and structure prediction algorithms, we have performed an extensive search for the most energetically stable borophene polymorphs on Al(111) substrate to gain insight into the role of electron-deficiency compensation through both self- and charge-doping processes. This was the starting point to investigate geometric- and electronic-structure modifications induced by redox reactions (introduced in the following chapters) as an alternative route to tune the coupling between borophene and the substrate, with respect to self-doping. The study confirms that honeycomb borophene, in p-T interval of experimental conditions, is the most stable structure on the aluminum substrate, which is consistent with experimental findings.

Finally, while our arguments are based on energetic considerations, it should be kept in mind that kinetic effects, including surface diffusion, segregation, and B gas temperature and pressure, affect and actually determine the effective experimental accessibility and observation of each proposed allotropic phase.

4 OXIDIZED BOROPHENE ON AL(111)

Somewhere, something incredible is waiting to be known. —- Carl Sagan.

4.1 INTRODUCTION

As we explained in chapter 3, the intricate geometric and electronic structure of boron allotropes is closely linked to their properties and is primarily caused by the difference in electron count between boron and carbon. This difference, known as the "electron deficiency" of boron, leads to the formation of multiple bonding centers and gives rise to the various forms of boron polymorphism. When boron is confined to a two-dimensional (2D) structure, its properties are influenced by the limitations in both its structure and electronic behavior. This results in the formation of a group of materials called borophenes. The properties of borophenes are determined by the combination of their inherent electronic structure and their interactions with the underlying substrate and the surrounding environment, which can be controlled by adjusting the chemical potential.

Unlike 2D materials like graphene, which can be readily separated from a substrate, borophene is a special case where the interaction between the boron sheet and the substrate or environment cannot be ignored. The substrate and environment play a crucial role in determining the specific structural, electronic, and chemical properties of each individual 2D boron phase. In general, the different boron phases have a relatively small energy difference compared to the confined allotropes. They are often (meta)stabilized due to unavoidable kinetic hindrance effects.

The experimental observation of the honeycomb boron phase on the Al(111) single crystal termination is a significant achievement in understanding the characterization of the borophenes family. By studying the B/Al(111) system, which forms the honeycomb AlB_2 layer [96], we can observe the intricate interactions between boron and aluminum. On the other hand, the phenomena shaping

2D boron allotropes (such as charge transfer, substrate bonding, segregation, diffusion, alloying, etc.) can be influenced by the chemical potential associated with the presence of a gas phase, with possible consequences on the decoupling and redox reactions[1]. The interactions between substrate, boron, and gases (in this thesis, oxygen and hydrogen) give rise to various phases such as borophane and aluminum oxide (beneath borophene phases), with different nanostructural properties like striped patterns, multi-layered structures, and one-dimensional arrangements.

In the case of oxygen adsorption, the interaction with the metal can be strong enough to induce relevant mechanisms of surface metal segregation, responsible for the formation of surface oxide films. Kinetic restrictions apply to the mechanism, which involves the ejection of Al atoms from the surface to form the oxide film and the formation of a low-density Al interface layer [128]. The relevant example is the growth of aluminum oxide on Al(111), governed by the motion of the buried metal-oxide interface [46]. In this context, the outward growth refers to the movement of Al^{3+} ions from the metal's bulk to the oxide phase. This mechanism is operational even at room temperature.

In this chapter, I present a thorough theoretical investigation that combines electronic structure methods, DFT, and novel genetic prediction approaches [85, 153] to predict the impact of interface oxidation on the electronic properties and structural stability of borophene allotropes grown on Al(111). Our extensive search for the stable structures of B_xO_y/Al(111) allows us to draw some conclusions on the phase diagram of this system. Depending on the oxygen chemical potential, we find that Al atoms are extracted from the surface and incorporated into the hB phase which becomes progressively rougher as a function of the oxygen concentration. We also observe that a significant redistribution of charge within the layer itself, along with the buckling caused by the distortion of bonding orbitals, also contributes to the overall behavior.

The rest of this chapter is organized as follows: The effects of oxygen doping are presented in Sec. 4.2: I first introduce the predicted structures in Subsec. 4.2.1, and then describe the corresponding charge-transfer mechanisms in Subec. 4.2.2. In Sec. 4.3 the phase diagram of the oxidized B@Al(111) interface is presented.

Although various structures have been theoretically predicted for both borophene and borophene oxides, the experimental realization of supported borophene and its oxides still appears quite challenging [145]. As a step forward with respect to conventional atomic-layer

1 Redox (reduction-oxidation) reaction refers to chemical reactions involving the transfer electrons between species. Here, boron and aluminum have different chemical affinities towards participating in redox reactions.

deposition approaches for B, a possible novel route to the chemical synthesis of 2D B layers has been reported only very recently [25]. This fact motivate me to report the experimental results, performed by our colleagues, as a complementary section (Sec. 4.4), which is in line with my calculations. Finally, the results are summarized in Sec. 4.5. Note that the computational details have been explained in appendix A. Since this chapter involves experimental and theoretical results, looking at appendix B, for a very brief overview of experimental methods and techniques, will help to follow the discussion.

4.2 OXIDATION OF THE B/AL (111) INTERFACE

Oxygen, a highly reactive gas and one of the most abundant elements in the Earth's atmosphere, plays a crucial role in surface chemistry and oxidation processes. Its interactions with materials can have significant effects on their structure, properties, and reactivity. Oxygen can participate in dissociative chemisorption, leading to the formation of surface compounds and the modification of surface morphology. Understanding the influence of oxygen on materials systems is essential for exploring their stability, reactivity, and potential applications.

The presence of oxygen can have diverse effects on different materials. In some cases, such as in ZnO [107] and B_2O [148], oxygen can influence the crystalline structure and properties of the substrate, leading to altered electronic properties or enhanced stability. However, oxygen can also induce disruptive effects, as seen in the corrosion process of iron, where the reaction with oxygen leads to the formation of oxides and degradation of the material.

Understanding the role of oxygen in the borophene-aluminum (111) system is of great importance, as it provides insights into the interfacial phenomena and the stability of the borophene layer. The question then naturally arises as to which effects the presence of oxygen may have on borophene formation, and on their dependence on the details of oxygen surface incorporation. Indeed, by combining experimental investigations with theoretical simulations, we can unravel the complex mechanisms underlying oxygen-induced changes in borophene and pave the way for its controlled synthesis and functionalization.

4.2.1 Structural prediction in the presence of oxygen

In order to study the tendency of oxygen and borophene to combine at an aluminum surface, we perform several genetic structural optimizations starting from different initial configurations mimicking

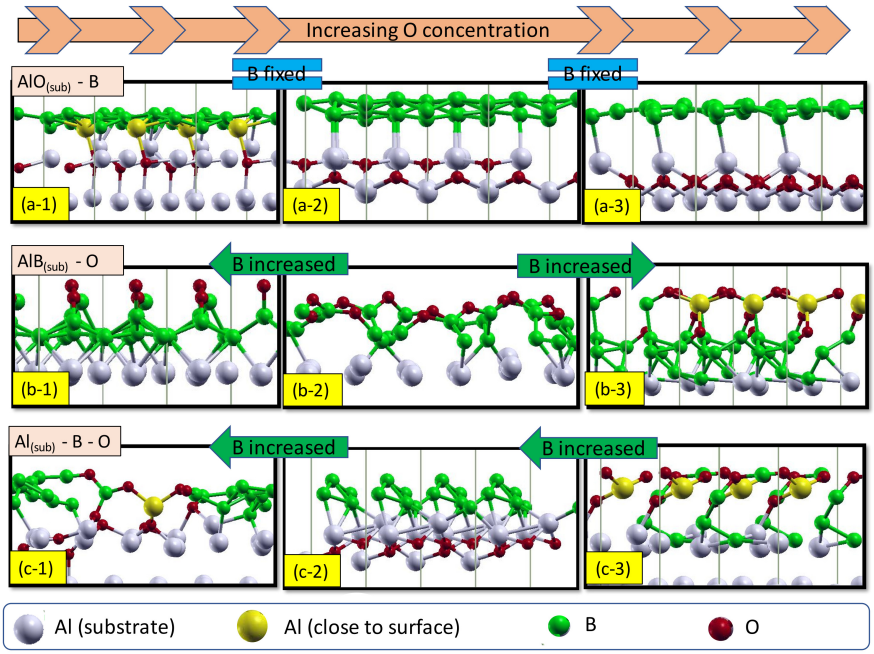

Figure 4.1: Three different setups of structure prediction: (a) Structures with AlO_x substrate (fixed B coverage 2 ML), with oxygen coverages of $^1/_2$ ML (a-1), $^3/_4$ ML (a-2), and 1 ML (a-3). (b) Structures with AlB_x substrate, with oxygen coverage of $^1/_2$ ML (b-1), $^2/_3$ ML (b-2), 1 ML (b-3) (boron coverags: 2, $^4/_3$, and 2 ML, respectively). (c) Structures with Al substrate, with oxygen coverage of $^2/_3$ ML (c-1), $^3/_4$ ML (c-2), 1 ML (c-3) (boron coverages: $^4/_3$, $^5/_4$, and 1 ML, respectively). Aluminum atoms completely extracted from the substrate and incorporated in the overlayer are shown in yellow.

different experimental conditions (details in section A.2). In the following, we will sometimes refer to each one of these initial configurations as a *setup*. In all cases we seek the lowest-energy configuration accessible from a given setup for a given stoichiometry, without, at this stage, accounting for any thermal or kinetic effects, such as temperature or the different partial pressures of the elements being adsorbed from the gas phase. Three qualitatively different setups are considered in the structural exploration, leading to the structures illustrated in Fig. 4.1. The surface coverage, expressed in monolayer (ML), is defined here as the ratio between the number of adsorbed atoms (boron and oxygen) with respect to the number of Al atoms of the terminal substrate layer (in initial configuration) per unit cell.

First, we suppose the aluminum surface to be passivated by pre-exposure to oxygen, corresponding to different O:Al re-coverages (a-1: $^1/_2$ ML; a-2: $^3/_4$ ML, and a-3: 1 ML). Boron atoms are then allowed to form the most stable configuration on top of these oxidized substrates. This setup mimics the effects of oxygen passivation of

the aluminum substrate on borophene formation, and also sheds light on the possible formation of honeycomb structure on aluminum oxide. The trend with respect to increasing oxygen concentration is clear: with higher oxygen coverage, the topmost aluminum atoms tend to bind preferably to oxygen and boron atoms are increasingly decoupled from the oxidized substrate. However, they tend to form triangular bonds, forming α, χ_3, and β_{12} structures rather than the honeycomb polymorph. As mentioned earlier, although these structures can be considered as energetically stable, the polymorph actually observed in an experiment will depend on the specific pressure/temperature growth conditions, as discussed in Sec. 4.3.

In a second setup, we investigate the stability of a pre-formed borophene overlayer to oxygen exposure. In this case (second row of Fig. 4.1), boron overlayers on Al(111) with two surface ratios, B:Al = 2 for b-1 and b-3, and B:Al = $^4/_3$ for b-2, are exposed to an increasing amount of atomic oxygen (with O:Al ratios ranging from $^1/_2$ in b-1, to $^2/_3$ in b-2, to 1 in b-3). Upon oxygen adsorption, a significant disruption of the borophene overlayer occurs as the highly electronegative oxygen tries to catch electrons as much as possible from its neighbors. The borophene layer reorganizes to the point that, at high oxygen concentration, channels are created through which aluminum atoms are close to the borophene layer, which are already observed in some low energy borophene-on-Al structures even in the absence of oxygen adsorption (see section 3.2.1 and Fig. 3.3), and migrate to the surface and directly bind to oxygen.

Finally, simultaneous adsorption of both oxygen and boron is considered, with different relative concentrations for a fixed combined (B + O) coverage of 2 ML (O:Al = $^2/_3$ and B:Al = $^4/_3$ in c-1, O:Al = $^3/_4$ and B:Al = $^5/_4$ in c-2, and O:Al = 1 and B:Al = 1 in c-3). In this setup, the two adsorbed species compete for bonding with the substrate atoms. This case is also designed to detect the possible creation of a boron oxide overlayer on the aluminum substrate [145]. Our results dismiss this possibility: when in excess, boron tends to cluster while oxygen binds preferably to aluminum forming an aluminum oxide layer. Occasionally, some boron-oxygen bond is observed but boron atoms clearly prefer to attach to aluminum or cluster on their own. This trend makes us conclude that borophene resists oxidation, at least in the presence of aluminum.

Overall, our simulations indicate that oxygen preferentially binds to aluminum rather than to boron, except when access to the substrate atoms is hindered by the pre-deposition of a boron layer. Even in this case, the interaction with the strongly electronegative oxygen atoms tends to disrupt the borophene overlayer that would need electron donation to be stabilized in a flat configuration. No tendency toward the formation of a boron oxide layer is observed. Boron atoms prefer

instead to cluster on their own, mostly forming triangular bonds or bonding to aluminum atoms.

4.2.2 Charge transfer in the presence of oxygen

As seen in the previous section, a different sequence in the surface exposure to boron and oxygen leads to different final configurations. This can be further analyzed by examining the corresponding charge-transfer profiles. Charge depletion and accumulation for the three structures from the first row of Fig. 4.1 are displayed in Fig. 4.2, which shows the planar averages of the charge density difference between the full systems and the superposition of the individual components of overlayer (combination of Al, B, and O, based on configurations) and of the substrate (in other words, we consider different substrates and overlayers in different structures. This separation is considered based on distance of atoms in z directions, meaning that the first distinguished gap in z coordination is considered for separation between substrate and overlayer, see equation 4.2.1).

$$\Delta\rho(z) = \frac{1}{S}\int_S \left(\rho_{tot}(\mathbf{r}) - \rho_{substrate}(\mathbf{r}) - \rho_{surface}(\mathbf{r})\right) dxdy, \qquad (4.2.1)$$

The main feature resulting from this figure is the accumulation of bonding charge between the overlayer and the substrate, counterbalanced by a depletion on Al and B layers. The charge density depletion around Al atoms is enhanced with increasing oxygen concentration.

Total-energy comparison of similar structures illustrated in Fig. 4.1, such as comparison of $AlO_{1/2}$–B_2 (a-1) with AlB_2–$O_{1/2}$ (b-1) or comparison of $AlB_{4/3}$–$O_{2/3}$ (b-2) with Al–$B_{4/3}$–$O_{2/3}$ (c-1), suggests that oxygen tends to bind to Al atoms, rather than to boron, a fact that could in principle be exploited to reduce the strength of the B–Al interaction. This is confirmed by Löwdin charge population analysis in Table 3, where we report the deviation from the atomic nominal valence charge. The order of the structures listed in the table follows the one used in Fig. 4.1. We can follow the trend of charge transfer across the table. For systems where oxygen is pre-adsorbed on the Al substrate (first row of figure 4.1), a strong transfer from aluminum to oxygen is observed, consistently with the large difference in electronegativity between the two species. Some donation from Al to B is also observed for low oxygen concentration, which is blocked as the oxygen fraction increases, and the borophene layer becomes more detached.

In the second setup (second row of Fig. 4.1), oxygen is adsorbed on top of an Al–B system and a strong reduction in the charge transfer

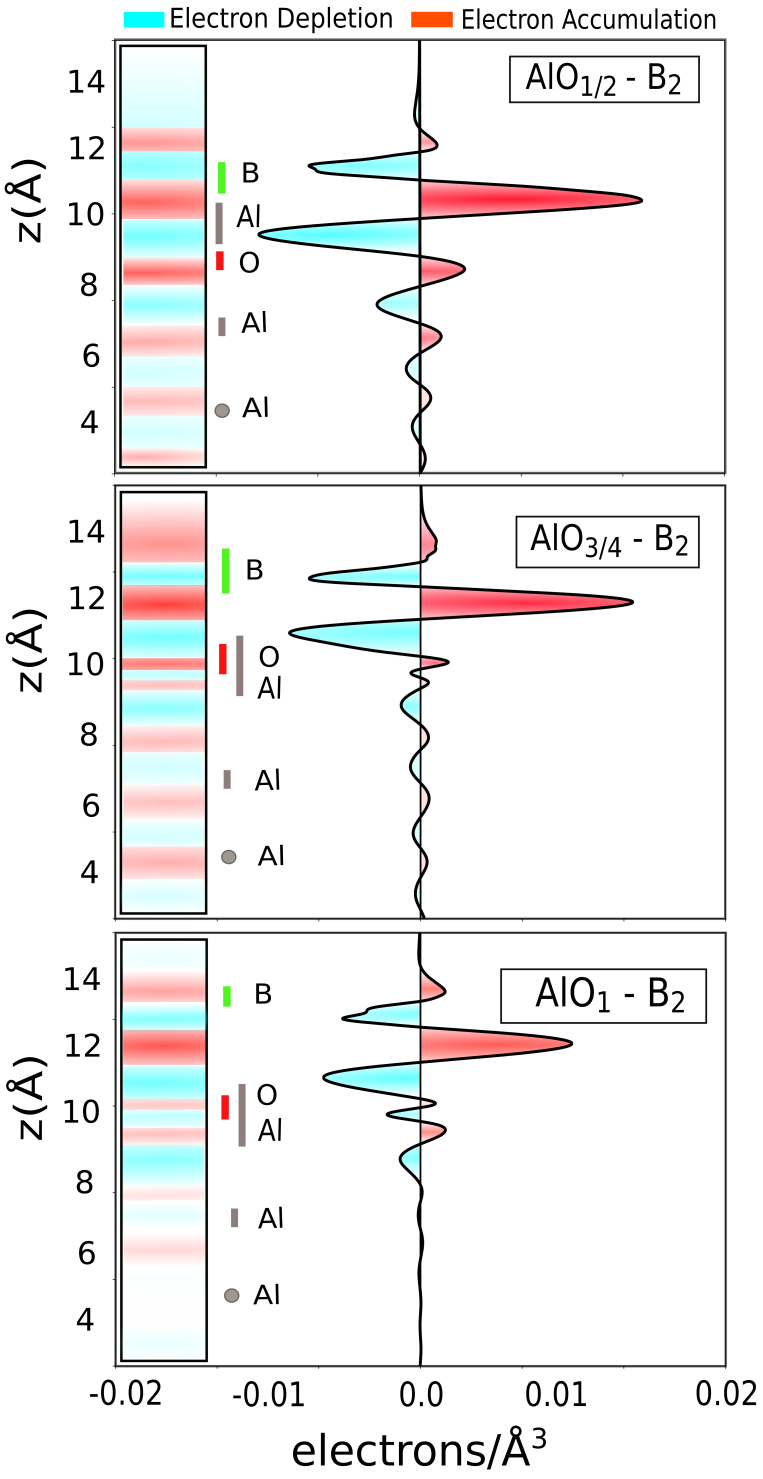

Figure 4.2: Charge density differences between aluminum and borophene in the presence of oxygen in the first setup (AlO_x–B_2) and second setup (AlB_x–O_y). The green span denotes the boron position and the red span shows the oxygen location of each structure. The vertical bars next to the chemical symbols of the various elements indicate the spread in the vertical positions of the corresponding atoms.

Table 3: Average values of accumulated and depleted electron per atom, calculated based on Löwdin population analysis, in different structures. For some structures, the average Löwdin charge of Al atoms can be further divided into two parts. The first part represents the contribution from Al atoms that are strongly bonded to atoms in the overlayer (either B or O, depending on the structure), shown as yellow in Figure 4.1. The second part includes the remaining Al atoms, which are depicted as light gray.

	(a-1)	(a-2)	(a-3)
Löwdin O (avg./atom)	0.767	0.804	0.808
Löwdin B (avg./atom)	0.225	0.037	0.002
Löwdin Al (avg./atom)	−0.875	−0.874	−1.061
Löwdin Al-yellow (avg./atom)	−1.231	...	...
Löwdin Al-gray (avg./atom)	−0.757	−0.874	−1.061
	(b-1)	(b-2)	(b-3)
Löwdin O (avg./atom)	0.330	0.341	0.538
Löwdin B (avg./atom)	0.065	−0.049	0.047
Löwdin Al (avg./atom)	−0.446	−0.268	−0.748
Löwdin Al-yellow (avg./atom)	...	...	−1.490
Löwdin Al-gray (avg./atom)	−0.446	−0.268	−0.501
	(c-1)	(c-2)	(c-3)
Löwdin O (avg./atom)	0.650	0.809	0.554
Löwdin B (avg./atom)	−0.002	0.228	0.013
Löwdin Al (avg./atom)	−0.536	−1.034	−0.650
Löwdin Al-yellow (avg./atom)	−1.137	....	−1.313
Löwdin Al-gray (avg./atom)	−0.462	−1.034	−0.430

can be observed. Again, Al atoms lose electrons to oxygen while B atoms remain largely unaffected merely shuttling the charge from the metallic substrate to oxygen. As the oxygen content increases and oxygen atoms find ways to directly bind to Al (figure 4.1 panel b-3), the Al–O charge transfer becomes significant again.

Finally, if O and B atoms are adsorbed at the same time in different concentrations (third row of Fig. 4.1, panels c-1 to c-3), B atoms prefer to form clusters with triangular bonds rather than competing with oxygen to bind to aluminum. Strong Al–O charge transfer results across the direct Al–O bonds while some Al–B charge transfer occurs only when B is directly in contact with aluminum. Aluminum is clearly the less electronegative of the three species and always loses electrons to its neighbors, especially when forming close bonds with the atoms in the overlayer (yellow atoms in fig. 4.1). These findings confirm that—because of the reduced charge transfer from aluminum to borophene due to the competing adsorption of the more electronegative oxygen—charge-doping of borophene is less likely to occur. Stabilization of the borophene layer occurs therefore through self-doping and the hB borophene polymorph has less chance to form.

4.3 PHASE DIAGRAM FROM *AB INITIO* THERMODYNAMICS

All the points discussed above are based solely on energetic reasoning and are relevant only for isolated systems, where the total energy and the number of atoms for each chemical species are kept constant. As explained in the previous chapter, the structures observed in an experiment are influenced by both kinetic and thermodynamic factors. Modeling the kinetic effects can be challenging, but overall, they are guided by the drive toward thermodynamic equilibrium between the sample and its surrounding environment, which includes the vapor in the growth chamber. This equilibrium allows for the exchange of atoms and heat. In order to account for these effects, we make use of concepts from *ab initio* thermodynamics [100, 102].

In simple terms, the thermodynamically stable structure is the one that, considering a specific temperature (T) and chemical potential (μ_X) of each atomic species, minimizes the surface (grand) free energy per unit area. At equilibrium, the chemical potentials of the various elements at the surface should equal those in the vapor phase. Assuming an ideal-gas law, which always holds at low pressure, the chemical potential of the atomic species X reads $\mu_X(p, T) = \mu^\circ(T) + k_B T \log(p/p^\circ)$, where p° is the pressure at *standard conditions* (*e.g.* the pressure at which the vapor is in equilibrium with the

bulk or some specific surface structure at a given temperature) and $\mu^\circ(T) = \mu(p^\circ, T)$ the corresponding chemical potential. A commonly adopted approximation is to neglect the vibrational contribution to the surface free energy, so that *e.g.* the surface grand free energy of the polymorph α, reads:

$$\varphi_\alpha(\mu_B) = \Big(E_\alpha^{tot}[sys] - E_{clean}[Al] - N_B \times E_{bulk}[B] - \frac{1}{2} N_O \times E_{gas}[O_2] \Big) \Big/ S - n_B \mu_B - n_O \mu_O, \tag{4.3.1}$$

where n_O and n_B are the numbers of O atoms and B atoms per unit area, respectively. The B chemical potential is referred to the bulk, *i.e.* the B vapor in the growth chamber is supposed to be in equilibrium with its own bulk. The reference data for the B chemical potential entering Eq. (4.3.1) are taken from Ref. [122]. These considerations will be used to analyze of the stability of B@Al[111] in the presence of oxygen. Our results are reported in Fig. 4.3, which displays the adsorption-free energies of various structures as functions of the B and O chemical potentials, and the corresponding phase diagram. The top panel reports the free-energy hyperplanes corresponding to the most stable phases found for the different stoichiometries we have explored. The lower panel shows the resulting stability phase diagram.

The structure, characterized by the adsorption sequence Al_{sub}–O_1–B_1 (c-3 in Fig. 4.1), is the dominant structure at low B chemical potential (low pressure) and any O pressure. An increase of the B chemical potential determines the transition to structures with higher B content, following the sequence $AlO_{1/2}$–B_2 (a-1), $AlO_{3/4}$–B_2 (a-2), and AlO_1–B_2 (a-3) (see Fig. 4.1) depending on the oxygen partial pressure. For low O partial pressure and intermediate B chemical potential a stability region for the Al_{sub}–$O_{3/4}$–$B_{5/4}$ structure (c-2 in Fig. 4.1) is present. In order to clarify and link all the results in one shot, charge transfer and configurations of the stable structures are mapped in Fig. 4.4.

By considering Fig. 4.4, we validate that oxygen has a tendency to intercalate itself between the boron sheets, while also forming strong bonds with aluminum at the interface between boron and aluminum layers. By exploring an extensive range of relative B vs. O coverage configurations, together with the optimization of a variety of local structures and bonding geometries, we find evidence that confirms the interpretation of the experimental findings in the next section.

For lower local B loading or for low $\Delta\mu_O$, detachment of Al atoms from the substrate is observed (yellow atoms in Fig. 4.4), forming Al–O structures and minor Al–B–O bonds at the boron layer, which is compatible with the 1D stripes imaged with STM (Fig. 4.5 in experimental section). However, a variety of intermediate bonding

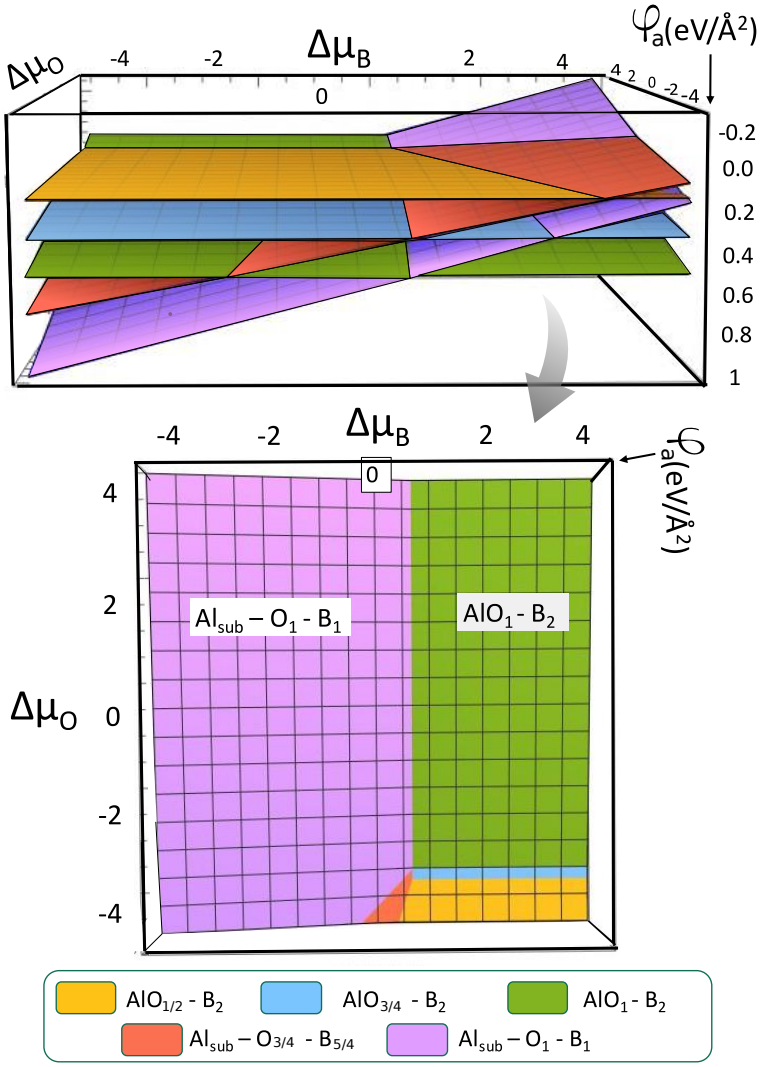

Figure 4.3: 3D phase diagram, showing the adsorption Gibbs free energy of the system as a function of B and O chemical potentials.

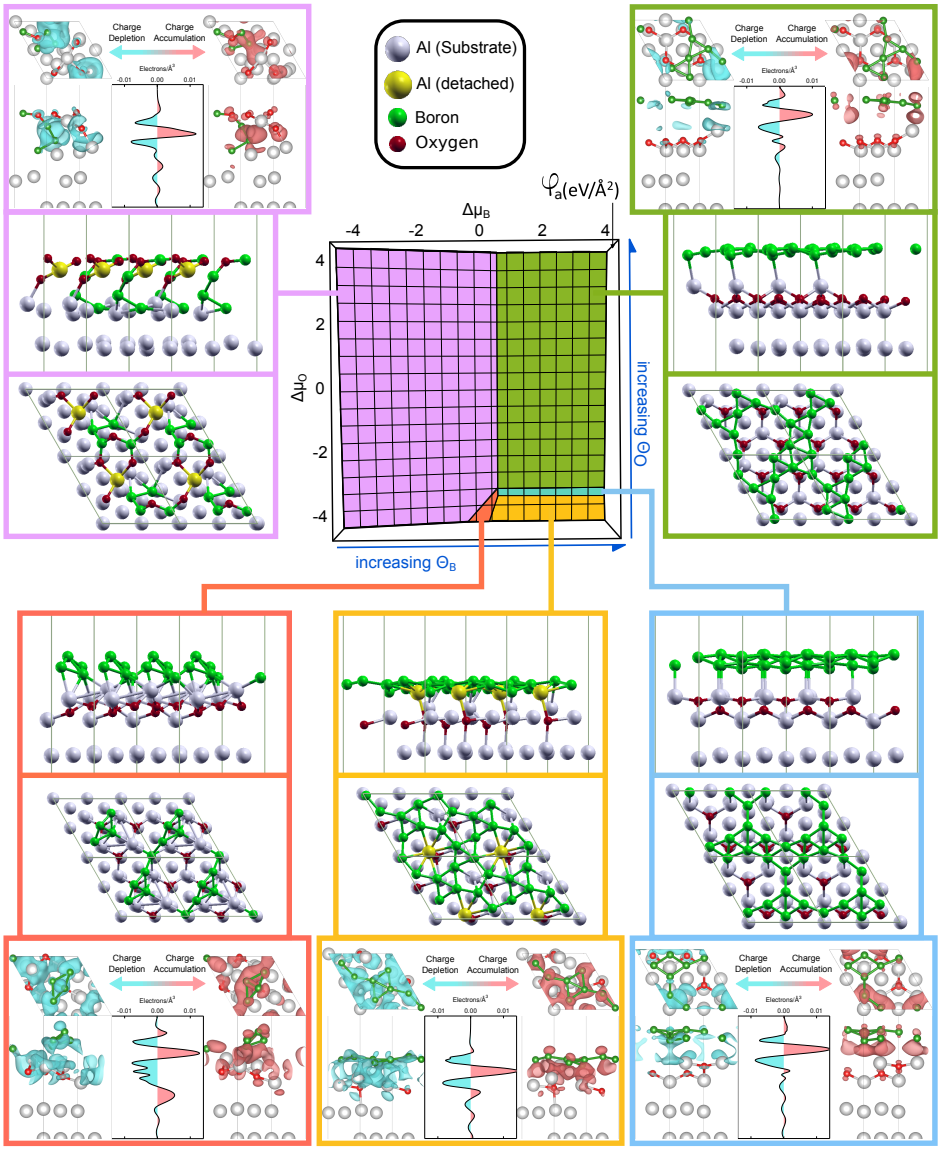

Figure 4.4: Best structures predicted by DFT combined with genetic algorithm methods for the oxygen + boron on Al(111). A phase diagram, from *ab initio* thermodynamic, is performed as a function of B and O coverage in relation to the chemical potential, confirming the tendency of oxygen to bind with aluminum and, under selected conditions, to promote its segregation to the topmost layer. The most stable structures' geometry and charge transfer plots with corresponding charge density isosurfaces are shown in the boxes.

geometries is achieved when spanning across the (μ_B - μ_O) chemical potential and (Θ_B - Θ_O) coverage spaces. Nevertheless, in all cases, preferential bonding of oxygen to Al rather than to B is observed, yielding oxidation of the substrate termination, oxidation of Al atoms segregated across the B layer, and formation of only minor ternary Al–B–O phases.

When looking at the charge transfer, we observe that in the pristine case, electronic charge gathers at the B–Al interface, reaching around $+0.035$ $e^-/Å^3$ (reported in chapter 3). This is mainly due to the terminal Al atoms. However, during oxidation, the charge distribution changes, resulting in a density modulation of approximately $+0.015$ $e^-/Å^3$ (indicated by boxes in Fig. 4.4). In general, when oxygen is adsorbed, it takes electrons from both the B termination of the film and from the interface (as shown in the cyan-shaded profiles within the boxes). This leads to an accumulation of electronic charge within the boron layer (as seen in the red-shaded profiles within the boxes).

In general, in the presence of several co-adsorbed species and with the variety of structures with similar energies that we have identified, these findings should be taken as only qualitative indications of the complexity of the structural landscape accessible in realistic conditions. The actual structures obtained in the lab likely depend on the growth protocol and associated kinetic effects, no less than on thermodynamic stability.

4.4 EXPERIMENTAL OVERVIEW OF OXIDIZED BOROPHENE

Disclaimer: The experimental work was performed by our colleagues at the Elettra synchrotron-radiation center and the University of Trieste.

To decouple or (ideally) exfoliate AlB_2 from the Al(111) termination, one can take advantage of the distinct chemical and electronic properties of boron (B) and aluminum (Al). As observed above, preliminary calculations within the framework of DFT already indicate that dissociative oxygen chemisorption on the B-covered Al termination would lead to the oxidation of the aluminum substrate, with Al showing a larger chemical affinity to O with respect to B [106].

Based on energy considerations and depending on the relative concentration of oxygen and boron, it was predicted that the boron layer could either remain on top of the oxidized aluminum termination or, alternatively, form a mixed ternary Al–O–B alloy locally. The specific outcome would depend on the amount of boron

present (referred to η, hexagonal hole concentration, see chapter 1: footnote 1) and the kinetic effects during the growth and oxidation processes [106].

Upon exposure of AlB_2/Al(111) to an oxygen background flux (up to 10^3 L) at room temperature, the B 1s core level revealed by XPS (Fig. B.4 column (a), top row) showed that most of the boron remains metallic, being only indirectly affected. Indeed, there is a small spectroscopic shoulder emerging at 188.46 eV (referred to as B6, $\Delta E = +0.70$ eV). This shoulder corresponds to boron species at the interface that directly interact with oxygen [86]. Although present, its contribution to the overall intensity is minimal, accounting for only about 1%.

No thick bulk oxide is observed, nor any other B_xO_y phase that would be anticipated to appear at much higher binding energies [86, 134]. Actually, this small sign of B oxidation occasionally appeared already at the stage of growing pristine AlB_2 and is not exclusively related to the oxidation treatment but to the presence of O contaminant species.

Another fingerprint of boron oxidation involving only a minor fraction of the layer is evident in the NEXAFS B K-edge profiles (B.4 column (c), top row), where a small feature with π character can be seen at 194.0 eV. It is associated with BO_3 planar groups on the basis of literature data [21, 95, 115].

The IR-Vis SFG spectrum of the layer in Fig. B.3 (upper panel) supports this observation. Upon oxidation, we observe three small peaks (low-amplitude resonances) at 1200, 1213, and 1231 cm^{-1}. These peaks have a common linewidth (3 cm^{-1}) due to decoherence and different phases with respect to the non-resonant background (78°, 329°, and 142°, respectively), indicating the presence of B–O bonds [114]. Based on the spectroscopic data, we can conclude that direct B oxidation is only marginal.

Indeed, upon exposure to oxygen, the XPS intensity of the B1 component (Fig. B.4 column (a), middle and top rows) diminishes in favor of a new component (B4) developing at 187.0 ($\Delta E = -0.72$) eV. The latter grows gradually with increasing O_2 exposure, saturating at high doses (1000 L). This component can be assigned to the patches where AlB_2 has lost contact with the metallic substrate and is lying on the buried Al_xO_y termination.

It is possible that after partial oxidation, a honeycomb B monolayer, rather than the AlB_2 monolayer, is on top of the Al_xO_y surface. However, from a chemical stability perspective, the latter scenario is less favorable. By examining the corresponding LEED images (Fig. B.2 (a)), it can be observed that even with prolonged oxidation, the LEED pattern characteristic of the pristine AlB_2 phase remains intact. This demonstrates the inherent high chemical stability of AlB_2.

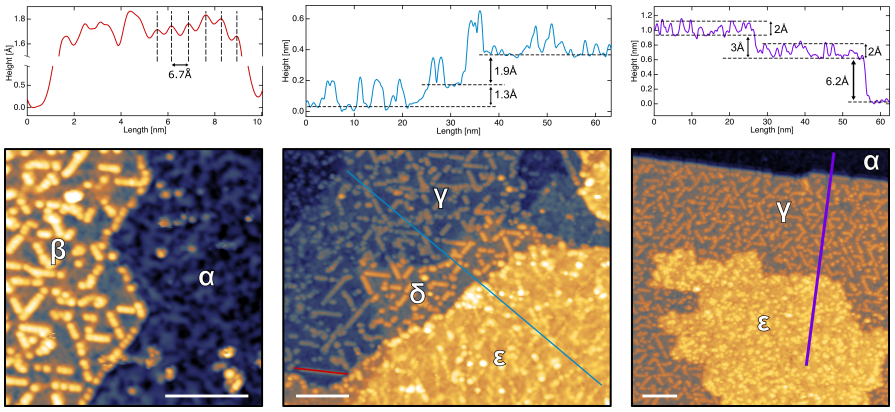

Figure 4.5: Line profiles (a-c) obtained by STM imaging (d-f) after room temperature oxidation of the $AlB_2/Al(111)$ surface with 45 L O_2. Scale bars in (d-f): 10 nm. Measuring parameters: (d) V_{bias} = +1.5 V, I = 300 pA; (e) V_{bias} = +1.0 V, I = 300 pA; (f) V_{bias} = +1.0 V, I = 300 pA.

In the case of Al 2p region from XPS spectra (Fig. B.4 column (b), top row), two not-fully-resolved spin-orbit doublets at higher binding energies can be anticipated (74.5 and 75.5 eV, black arrows in column (b), top row of the figure). These are typical signs of aluminum oxidation on surfaces [84]. In addition, a small shoulder appears at lower binding energy ($2p_{3/2}$ at 72.4 eV) with respect to the main Al bulk peak ($2p_{3/2}$ at 72.6 eV), possibly due to low coordinated Al atoms associated with the roughening of the surface.

NEXAFS B K-edge spectra (Fig. B.4 column (c), top row, including the difference spectra in blue) show that the main π- and σ-character resonances at 187, 189, and 193 eV, respectively, remain dominant after oxidation. This result supports the conclusion that the topmost AlB_2 layer retains its electronic structure to a large extent. Moreover, the growth of π and σ character resonances at 187.4 and 197.2 eV, respectively, indicates increased trigonal boron coordination [29].

All pieces of spectroscopic and diffraction information are in agreement with the STM images (Fig. 4.5), showing the development of Al_xO_y phases on the remaining clean Al islands (α), with their typical appearance [17]. Additionally, 1D stripes are seen growing on top of the β, δ, and γ phases, aligning mainly along the primary crystallographic directions (Fig. 4.5, d-f).

The unidimensional structures that appear on top of the pristine AlB_2 exhibit a noticeable, though irregular, height corrugation of the order of 1-2 Å and a precise periodicity of 6.7 Å (Fig. 4.5 (a)). However, on the AlB_2/AlB_2 (ϵ) phase, much of the order is lost. The AlB_2 layer behaves in a way that is very similar to the case of small B_mAl_n clusters, for which it has been recently observed that endohedral boron forms upon post-oxidation. The chemical treatment promotes

B dilution into the bulk and Al segregation to the surface, yielding a sort of alumina-caged boron [113, 116].

Similarly, the 1D stripes forming on the AlB_2 surface could be attributed to chains of Al_xO_y clusters, which is supported by both STM observations and Al 2p core level data. However, in contrast to borophene on Ag(111) [73], only minimal oxidation of borophene is noticed here, where individual oxygen ad-atoms can be clearly identified [66]. These findings are in line with the larger electron affinity of aluminum with respect to boron, governing the actual surface chemistry and composition under oxidizing conditions.

As explained previously, our theoretical results, from DFT and *ab initio* thermodynamic approach, validate the tendency of oxygen to intercalate itself between the boron sheets, while also forming strong bonds with aluminum at the interface between boron and aluminum layers. These results are summarized in Fig. 4.4, confirming the interpretation of the experimental findings.

In summary, the formation of boron oxide is not observed or predicted. Instead, it can be found that oxidation of the Al termination and the creation of 1D cluster arrays are more likely due to the different affinities of oxygen towards Al and B. The process is influenced by the segregation of Al and the diffusion of oxygen across the B layers.

4.5 CONCLUSIONS

By combining *ab initio* methods and structure prediction algorithms, we have performed an extensive search for the most energetically stable oxidized borophene polymorphs on Al(111) substrate to gain insight into the role of electron-deficiency compensation through both self- and charge-doping processes. This knowledge helps us to investigate geometric- and electronic-structure modifications induced by oxidation as an alternative route to tune the coupling between borophene and the substrate. We conclude that oxygen, due to its high affinity with aluminum, yields passivation of the metal surface and tunes the charge transfer from the metal to borophene. The formation of B–O bonds is hardly observed in the decoupled borophene layers, mostly showing triangular bonding geometries close to the α, χ_3, and β_{12} structures rather than to the honeycomb layout. Since oxygen hinders the charge transfer from Al to borophene, the resulting electron deficiency is compensated by the formation of other bonding geometries with a higher average filling factor and pronounced buckling. Thus, our results reasonably put in evidence that, in the view of decoupling and stabilizing a honeycomb borophene phase by means of oxidation, the bonding energy between

boron and metal substrate, oxygen and boron, and oxygen and metal substrate should be carefully balanced by a proper choice of the growth substrate. This may be accomplished e.g. by diluting Al and choosing an Al alloy, as a supporting template, with reduced Al–O interaction but, still, with sufficient available charge transfer attitude.

5 HYDROGENATED BOROPHENE ON AL(111)

It doesn't matter how beautiful your theory is, it doesn't matter how smart you are. If it doesn't agree with experiment, it's wrong. —-

Richard P. Feynman.

5.1 INTRODUCTION

As explained in previous chapters, the recent interest in studying different forms of 2D boron has resulted in claims of successfully stabilizing a honeycomb phase that exhibits a conical Dirac-like electron dispersion. Nonetheless, achieving the synthesis of chemically stable, single, and consistent 2D boron phases remains a considerable experimental obstacle. This is attributed to the inherent electronic configuration of boron, which, unlike carbon, results in the formation of covalent bonds with multiple centers. External charge compensation by substrate-induced doping can steer the geometry of the layer, both in the buckling and in the density of B vacancies, like in the case of the recently achieved stabilization of honeycomb boron layers on Al(111). However, the drawback is that there is a strong interaction between boron and the supporting material, which generally hinders the synthesis of homogeneous single phases due to kinetic limitations. In the case of Al(111), an AlB_2 layer is known to form on the surface, which is quite different from the desired configuration of a quasi-free-standing borophene monolayer. This is in contrast to graphene, which can be easily synthesized in an almost free-standing configuration, such as on Ir(111). Thus, while a honeycomb boron sheet is too unstable to exist in a free-standing form, its stabilization on a substrate is possible due to considerable electron donation, although at the cost of a strong B-surface chemical interaction.

On the other hand, hydrogenated hB (H-hB), namely borophane, has a dynamically stable structure and is expected to maintain (anisotropic) Dirac cones between the Γ and X points in its electronic configuration, at least within a model tight-binding picture with terminal H atoms [83]. Moreover, it was experimentally observed

that chemical stability is enhanced upon hydrogenation [67, 111, 135]. The recent successful synthesis of a variety of supported hydrogenated boron polymorphs on Ag(111), including short-range ordered honeycomb islands, has thus fuelled the efforts towards the search for monophasic hydrogenated boron monolayers [67]. Indeed, the chemical modification of borophene reveals quite complex aspects, associated with the multicentred bonding configuration and anisotropic features of borophene. The tuning of the electronic properties and the chemical passivation of boron monolayers through redox reactions were addressed as optimal routes toward the stabilization and possible decoupling of new 2D boron-based materials. However, as mentioned in chapter 4, while the process of oxidation was influenced by the competing affinities of boron and the supporting metal for oxygen electrons [106], hydrogenation still seems a more straightforward route [55, 67, 141].

To date, hydrogenated borophene layers are characterized by the co-presence of distinct polymorphs, with most of the lattice geometries remaining elusive due to the wide configurational space [141]. Different hydrogenation patterns on the boron layers at surfaces could be mainly characterized only locally by means of Scanning Tunnelling Microscopy (STM) imaging or Scanning Tunnelling Spectroscopy (STS) associated with *ab initio* theoretical simulations [55, 67, 141].

Furthermore, the preferred sites for hydrogen adsorption on various borophene allotropes, such as β_{12}, χ_3, and α, are determined by both the ratios of B and H elements and the local overlap between B p_z and H s orbitals [55]. Based on this understanding, a recent development involves a Hückeloid model for planar boranes. This model takes a Kekulé structure of a planar conjugated hydrocarbon and transforms it into a borane structure by replacing carbon atoms with boron atoms and adding a transverse H_2 molecule in the middle of each double bond. This results in B(κ(S)) structures with additional bridge hydrogen atoms [59].

This chapter is about the reversible formation of well-ordered honeycomb borophane through hydrogenation of the honeycomb boron phase on Al(111). By combining theoretical modeling and simulations with experimental techniques, we can unravel the intricate dynamics of the hydrogenation process and elucidate the underlying mechanisms that drive the observed changes in borophene properties. Indeed, this hydrogenation process not only modulates the boron-substrate interaction but also moves towards achieving a stable and almost free-standing honeycomb phase with interesting electron conductivity properties[1].

1 The expected electron conductivity properties are similar to the properties observed in the bulk MgB_2 high-temperature superconductor.

The rest of this chapter is organized as follows: The effects of hydrogenation are presented in Sec. 5.2: I first introduce the predicted structures in Subsec. 5.2.1, and then describe the corresponding charge-transfer mechanisms in Subsec. 5.2.3. In order to see the dynamical stability and phonon frequencies, the result of DFPT calculation is reported for this system in Subsec. 5.2.4. The experimental results, performed by our colleagues, are reported as a complementary section (Sec. 5.3), which is in line with my calculations. Moreover, the characterization of the electronic configuration of hydrogenated borophene on Al(111) from experimental and theoretical points of view is presented in Sec. 5.3.1. Finally, the results are summarized in Sec. 5.4. Note that the computational details have been explained in appendix A. Since this chapter involves theoretical and experimental results, looking at appendix B, for a very brief overview of experimental methods and techniques, will help to follow the discussion.

5.2 HYDROGENATED BOROPHENE ON AL(111)

This section delves into the intriguing effects of hydrogenation on borophene when it interacts with Al(111). Indeed, we explore theoretically the consequences of introducing hydrogen atoms to the boron layer. Firstly, we discuss the predicted structures, presenting different arrangements. Then, we explore the fascinating charge-transfer mechanisms associated with hydrogenation. These insights will shed light on the complex interactions and behaviors of the hydrogenated borophene on the Al(111) surface.

5.2.1 Structural prediction in the presence of hydrogen

Utilizing the genetic algorithm implemented in USPEX [85], we can predict the geometric features of hydrogenated borophane (for the computational details, see Appendix A). The procedure is to consider different ratios of hydrogen and boron on fixed aluminum substrates. One of the systems is with 1H:2B ratio, which results in the most stable structure illustrated in panel (a) of Fig. 5.1. But the next closest structure with just 0.002 eV/atom difference is shown in panel (b) of Fig. 5.1 ("atom" refers to all the atoms in the supercell). This fact shows that the system, with small fluctuations in kinetic energy, tends to have a lower concentration of hydrogen (1H:4B). Theoretically, this confirms that this coverage represents saturation since denser H loading turns out to be energetically stable but tends to be less concentrated with small kinetic energy (If the sample temperature increases from 0° C ($k_BT = 0.023$ eV) to 17° C ($k_BT = 0.025$ eV), this

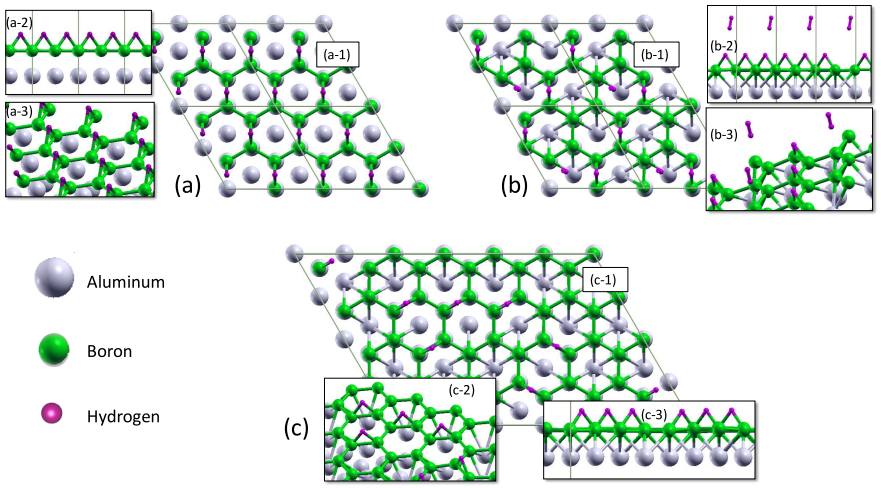

Figure 5.1: Top and side views of the most stable structures of borophane on aluminum substrate (B:Al ratio equals 2): (a) the most stable structure of 1H:2B ratio, (b) the second most stable structure of 1H:2B which tends to be 1H:4B, and (c) the stable structure of 1H:6B.

sample gains enough thermal energy to convert from 1H:2B to 1H:4B concentration).

Interestingly, it has recently been observed that a partially dehydrogenated borophane phase (1H:2.5B) shows the highest catalytic activity of HB sheets in ethanol reforming (HB sheets act as solid-acid catalysts[2]) [36]. This implies that adjusting the degree of borophene reduction could serve as a means to customize the stability, electronic characteristics, and catalytic properties of the sheet. These results also confirm that the charge successfully transfers from aluminum substrate to borophene, which means the system needs less hydrogen ad-atom to stabilize. The next case scenario is the system with 1H:6B ratio, as the stable structure illustrated in panel (c) of Fig. 5.1, which is the ratio of the experimental setup as well.

5.2.2 Symmetrized Borophane

As it is observed, the genetic algorithm does not lead to a long-range ordered (1H:6B) hydrogenated borophene, which is expected based on low H concentration. Indeed, the concentration is extremely low, to the point where hydrogen atoms do not interact significantly with one another. This outcome is in line with the expectations for the PBE functional, which we have employed in our investigation.

2 HB sheets catalyze the conversion of ethanol to ethylene and water above 493 K with high selectivity, independent of the contact time, and with an apparent activation energy of 102.8 ± 5.5 kJ/mol.

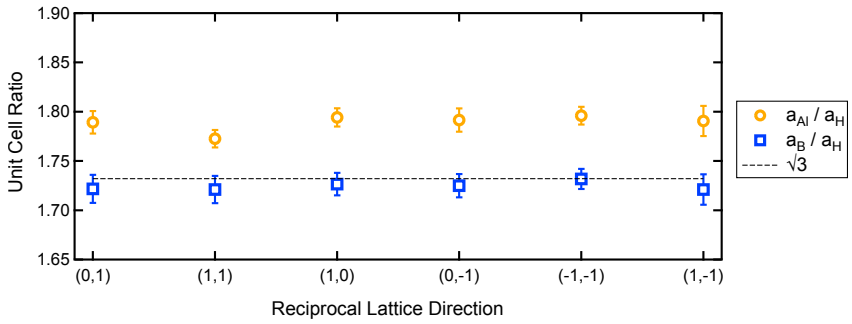

Figure 5.2: Compatibility of the H-induced unit cell size with the proposed $(\sqrt{3} \times \sqrt{3}) - R30°$ superstructure referred to the hB phase obtained from LEED.

Nevertheless, experimental efforts have successfully synthesized such structures. Indeed, after reduction, additional diffraction spots appear in the LEED pattern (Fig. B.2 (d)), indicating the formation of a well-ordered, long-range $(\sqrt{3} \times \sqrt{3})$-R30° superstructure (lattice parameter 5.10 $\pm$ 0.02 Å) with respect to the hB (2.96 $\pm$ 0.01 Å) layer (Fig. 5.2).

In detail, this means that the data points tend to align in a triangular pattern with a specific periodicity, leading to the observed $\sqrt{3}$ correlation. This triangular symmetry is likely to be caused by the underlying atomic arrangement in the material. This piece of evidence convinces me to theoretically investigate such symmetrized (and well-ordered) hydrogenated system.

5.2.3 Charge transfer in the presence of hydrogen

Following a similar pattern to previous chapters, I recall a brief explanation about how to calculate the charge transfer in the hydrogenated case. To understand the charge transfer mechanisms taking place at AlB_2 interface with hydrogen ad-atoms, and their impact on structural stability and experimental observations, we examine the planar average of the displaced charge distribution of the system. This average is defined as:

$$\Delta\rho(z) = \frac{1}{S}\int_S \left(\rho_{BH@Al}(\mathbf{r}) - \rho_{AlB}(\mathbf{r}) - \rho_H(\mathbf{r})\right) dxdy \,, \tag{5.2.1}$$

where $\rho_{BH@Al}$ denotes the electron charge-density of the Borophane@Al(111) system, while ρ_{AlB} and ρ_H correspond to those of the two constituents with their atoms clamped at the positions they would have at the interaction, and the integral is performed over planes perpendicular to the growth direction (z).

To make a more clear picture of charge transfer, the 3D isosurfaces, separated in depletion and accumulation, are also

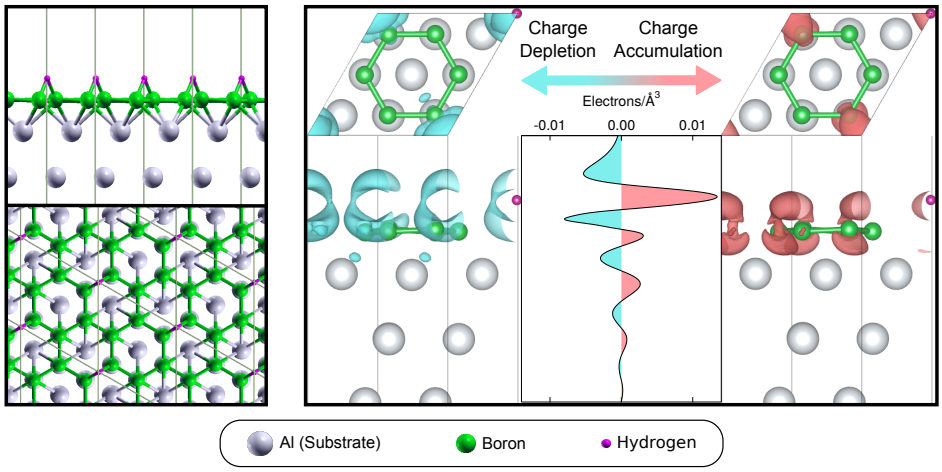

Figure 5.3: Best geometry for the hydrogen-induced $(\sqrt{3} \times \sqrt{3})$-R30° superstructure, together with the associated planar average of charge transfer and corresponding charge density 3D isosurfaces (0.02 $e^-/Å^3$).

depicted. Comparing this information put in evidence that H coordination to the boron layer yields the slight n-doping of B atoms (H-coordinated) implying depletion around hydrogen atoms, while the Al layer is hardly affected by the reduction (Fig. 5.3).

To have a new insight into charge transfer, we reconsider equation 5.2.1, with a different arrangement of substrate and surface, i.e. solely aluminum is considered as the substrate and borophane (and borophene) as the surface. This reconsideration is formulated as:

$$\Delta\rho(z) = \frac{1}{S}\int_S \left(\rho_{B(H)@Al}(\mathbf{r}) - \rho_{Al}(\mathbf{r}) - \rho_{B(H)}(\mathbf{r})\right) dxdy\,, \qquad (5.2.2)$$

where B(H) refers to borophene or borophane (H stands for the hydrogenation process).

By utilizing this formula (Eq. 5.2.2) to calculate the planar average of charge transfer reported in Fig. 5.4 (c), the small differences with respect to borophene charge transfer is observed, as we expect here. Indeed, with one hydrogen atom per cell, this amount of change is valuable, implying that increasing H atoms lead to more charge accumulation in bond regions of B and H. We can also observe 3D charge depletion and accumulation isosurfaces (0.006 $e^-/Å^3$) for both borophane (5.4 panel (a)) and borophene (5.4 panel (b)). At these isosurfaces, the depletion around H atom is obvious, while accumulation sites of boron atoms are distorted. This analysis provides valuable insights into the effects of hydrogenation.

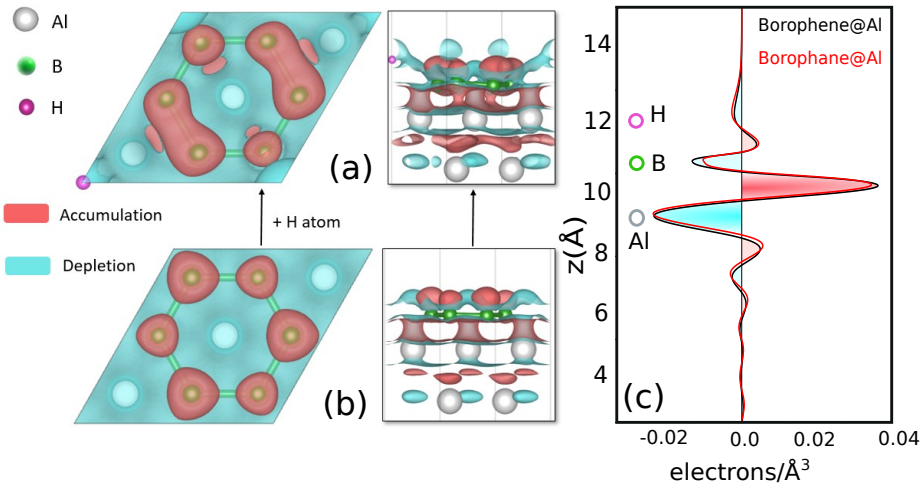

Figure 5.4: Charge transfer in the form of 3D isosurfaces (0.006 $e^-/Å^3$) from Al(111) to (a) borophane - top and side view and to (b) borophene - top and side view. (c) planar averages of charge transfer from Al to borophene (in black) compared with borophane (in red).

5.2.4 Vibrational Properties of Borophane on Al(111)

In this subsection, we explore the vibrational properties of borophane on the Al(111) surface using Density Functional Perturbation Theory (DFPT) described in Sec. 2.3. Vibrational properties play a crucial role in understanding the dynamic behavior of materials and can provide valuable insights into the stability and reactivity of the system.

Since the system has a relatively large number of atoms (22 atoms, including hydrogen) and 2D confinements, the phonon calculation is very time-consuming. On the other hand, the experimental vibrational outcomes mostly correspond to Γ point frequencies. Note that vibrational properties are investigated experimentally by IR-vis SFG spectroscopy, which only samples long-wavelength vibrations. These facts lead me to calculate the Phonon frequencies at Γ point as well. To compute phonon frequencies, we determine the dynamical matrix using dynmat.x and enforce the implementation of the Acoustic sum rule. After conducting the calculations, the system's stability was confirmed, showing no imaginary frequencies. The highest frequency observed for the system at the Γ point is 1973 cm^{-1}. As additional technical details, it is noteworthy that the latest version of QUANTUM ESPRESSO enables phonon frequency calculations using GPU [43], which was employed for this study.

On the other hand, experimentalists have measured the vibrational frequency with the IR-Vis Sum Frequency Generation (SFG) spectra. Based on experimental observation, this high frequency is associated with the B–H stretching mode, indicating that hydrogen atoms are

attached to the bridge positions within the boron network [67]. The dispersive vibronic resonance is observed in the IR-Vis SFG spectra at 1934 cm^{-1}, close enough to theoretical data.

5.3 BOROPHANE: EXPERIMENTAL OVERVIEW

Disclaimer: The experimental work was performed by our colleagues at the Elettra synchrotron-radiation center and the University of Trieste.

Recently it was shown that, by directly adding hydrogen to borophene on Ag(111), extended borophane phases can be synthesized [141]. Various hydrogenated boron phases were present together, and it was challenging to avoid their co-existence. Among them, a small portion consisted of honeycomb borophane, while the most abundant polymorph displayed a combination of two-center-two-electron B–H and three-center-two-electron B–H–B bonds [67]. The positions where hydrogen atoms bind are influenced by the arrangement of neighboring boron atoms, and the interaction with the metal substrate is crucial in determining these sites [55]. Additionally, reducing borophene leads to beneficial chemical passivation, especially lowering the rates of oxidation [67].

To synthesize borophane, the prepared hB/Al(111) phase was subjected to atomic hydrogen at room temperature. The same outcomes were achieved using two different methods: thermal cracking of H_2 with a hot tungsten filament placed in front of the sample [18], and dosing hydrogen from a Bischler and Bertel atomic hydrogen source [14, 30].

The B 1s spectrum (Fig. B.4 column (a) bottom row) is modified on the low binding energy side, where a new component (BH) grows at 187.27 eV between B_2 and B_3. Since B_2 is associated with the B atoms of AlB_2 above a buried B layer, we can conclude that H atoms bind to this elevated fraction of the structure [96]. According to the symmetry of the hydrogenated honeycomb boron superstructure observed with LEED, we do not expect that all B atoms get involved in the formation of a bond with hydrogen. Concerning the aluminum 2p core level (Fig. B.4 column (b) bottom row), only minor changes are observed, which can hardly be quantitatively distinguished within the experimental error bar. Specifically, when the hB/Al(111) layer is subjected to hydrogenation, the B-related Al 2p components show a broadening characterized by a Gaussian distribution. This broadening is accompanied by an increased asymmetry, which arises from the geometric inhomogeneity of the system. However, unlike boron, hydrogen adsorption does not lead to significant charge transfer to the aluminum substrate.

Upon hydrogenation, we also find that the B 1s absorption edge (NEXAFS spectra in Figs. B.1 and Fig. B.4 column (c) bottom row) is modified in both its π^* and σ^* structures. At the edge, there is a noticeable change in the behavior of resonance at 187.3 eV, displaying strong π^* dichroism. This change occurs at the cost of a non-varying resonance observed at 189.3 eV in the case of the bare AlB_2 layer.

Concerning the σ^* structure, the spectra are modified at 201 eV, showing an opposite angular dependence with respect to the π^* transition. A dispersive vibronic resonance appears in the IR-Vis SFG spectra at 1934 cm^{-1} frequency[3], with a phase of 25° relative to the non-resonant background (Fig. B.3 bottom curve). We associate this feature with the B–H stretching mode, indicating that hydrogen atoms are attached to the bridge positions within the boron network, which also is drawn from our *ab initio* calculations, as mentioned before. Indeed, the genetic algorithm search for the best H structure on hB/Al(111) always yields bridge coordination sites for the H ad-atoms. The optimized structure that correctly reproduces the observed symmetry constraints is reported in Fig. 5.3 left side.

In terms of stability, we have observed that the hydrogenated boron layer remains stable at room temperature. However, when heated to the borophene growth temperature (500 K), dehydrogenation can occur, causing hydrogen desorption and recovering all spectroscopic features of the pristine hB phase, together with the associated LEED pattern.

The above process was accompanied by a decrease in both resonant and non-resonant amplitudes and an increase in the Gaussian width of the signals. These changes indicated the development of disorder in the hydrogen superstructure due to the increasing temperature, leading to the eventual complete desorption of hydrogen [13].

5.3.1 Electronic configuration of Borophane

The influence of the exposure to atomic hydrogen on the electronic configuration of the layer is best evidenced by the comparison between spectroscopic information and theoretical calculations. In the energy range slightly below the Fermi edge, the dominant contribution comes from the boron σ component (as shown in Figure 5.5 (a) and (c)), which is not strongly affected by the reduction process. However, above the Fermi level, we observe several changes that can be attributed to the formation of B–H bonds.

As observed above, in the B edge π^* region, a dichroic feature grows at an energy of 187.3 eV, which is 0.3 eV higher than the energy

3 As it is explained above, the DFTP results conclude to a value of 1973 cm^{-1} for this stretching mode and is supported by comparing it to previously estimated values (1920 cm^{-1}) [67].

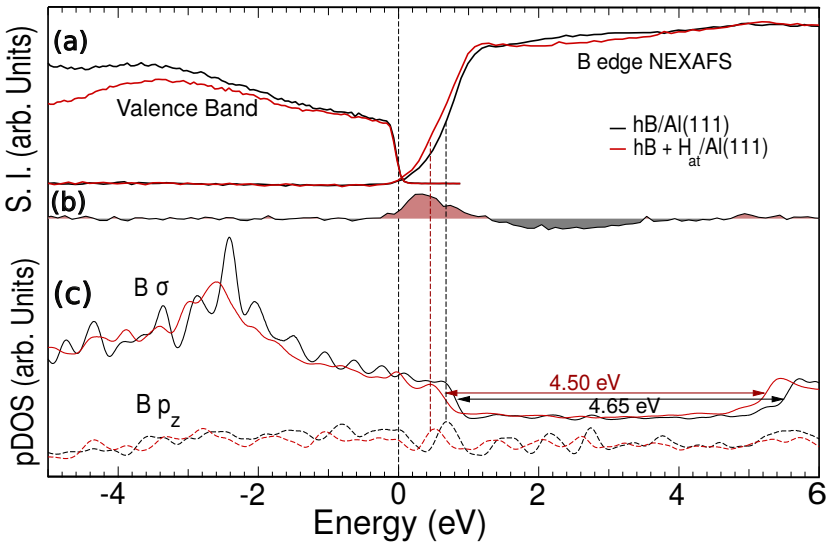

Figure 5.5: Experimental and theoretical characterization of the electronic configuration of the layer. (a) Experimental valence band (left, hν= 80 eV) and B edge NEXAFS spectra (E vs. z 20°) of the pristine (black) and hydrogenated (red) layers; (b) difference NEXAFS spectrum obtained from the spectra in (a); (c) calculated pDOS on the σ (top) and p_z orbitals of the B layer. The alignment of the Fermi levels of the valence band spectra and pDOS with the NEXAFS spectra were obtained according to recent work on the B mono- and multi-layers on Al(111) [96].

zero point shown in Fig. 5.5 (a). This can be clearly observed in the difference spectrum reported in panel (b) of the figure.

Moreover, our *ab initio* calculations reveal a shift of 170 meV towards lower energies in both the p_z and σ (p_x and p_y) density of states upon hydrogenation, as shown in Fig. 5.5 (c). This shift is accompanied by narrowing the σ gap from 4.65 to 4.50 eV.

5.4 CONCLUSION

We present here the theoretical study of hydrogenated borophene while considering applicability and availability and report corresponding (complementary) experimental results. Both theoretical and experimental aspects agree that reduction involves only boron atoms, generating a stable, long-range ordered honeycomb structure and showing bridge-coordinated H atoms. Due to the strong B–Al interaction and sufficient charge transfer from the Al substrate, the H-hB layer does not yield a fully H-covered borane structure, with H atoms sitting at the surface-exposed bridge sites on the hB layer. The vibrational properties of borophane show its stability. All of these key findings confirm that hydrogenation can be addressed as a promising chemical passivation treatment (which was done also by others) to reduce the boron-substrate interaction, thus stepping towards the synthesis of a stable, more decoupled honeycomb phase with interesting electron conductivity properties.

6 LONG-RANGE CORRECTION IN NNIP

The most important thing is to never stop questioning. —- Albert Einstein.

6.1 INTRODUCTION

In chapters 3, 4, and 5, we have reported results of a complex system with standard methods such as DFT, *ab initio* thermodynamics, and DFPT. By constructing a temperature-pressure phase diagram and Gibbs free energy-chemical potential, we obtained valuable insights into the influence of environmental conditions on stability and synthesizing process. Our results were followed and confirmed with experimental findings. Although these results are valuable and trustworthy, we cannot obtain all the properties of interest in a reasonable time scale, at least not with the same precision. Indeed, these techniques have limitations that hinder their applicability in studying large systems, with such a big number of atoms.

For instance, the investigation of phonon dispersion in crystals and surfaces holds vital significance in gaining insights into their structural and dynamic characteristics. Phonons, which represent quantized vibrations of the crystal lattice, play a pivotal role in numerous physical phenomena encompassing thermal transport, optical properties, phase transitions and are the focus of many spectroscopies and structural characterization techniques. Precise calculations of phonon dispersion are necessary for a comprehensive understanding of these phenomena.

However, conducting phonon calculations can be a time-consuming process, particularly as the number of atoms in the system increases. State-of-the-art approaches like DFPT for phonon calculations become increasingly inconvenient in such cases.

Therefore, alternative methods, such as force-field Molecular Dynamics (MD) or Monte Carlo (MC) based phonon calculations, can be employed to obtain phonon dispersion and reduce the computational time using some empirical force fields. These alternative methods are fast but their reliability is based on the accuracy and transferability of the employed force field, which is often limited due to the rigid functional form they implement.

In recent years a new approach has emerged based on the development of machine learning (ML) potentals that implement very flexible functional forms and can be trained on *ab initio* data thus combining, when successful, the computational efficiency of an empirical potential and the accuracy of the *ab initio* treatment.

However, the accurate prediction of certain phonon properties, such as the LO-TO splitting in polar materials, presents challenges which are not met by the locality assumptions usually adopted in machine learning schemes. In fact, the LO-TO splitting in the vibrational properties of polar materials results from the long-range nature of Coulomb interaction, while the state-of-the-art neural network interatomic potentials (NNIP) are directly constructed based on descriptors of the local chemical environment that are truncated at a finite spherical cutoff. This approach, by construction, neglects the electrostatic interactions whose long-wavelength limit contains the ingredients to account for the so-called non-analytic correction in the interatomic force constants.

To overcome these limitations, a refined approach is needed to construct an accurate and computationally efficient machine learning interatomic potential capable of describing long-range interaction for general atomic environments. Here, we apply the recently developed [109] incorporation of long-range electrostatics in NNIP to the description of the LO-TO splitting in polar materials and, as a first example, compute the full phonon dispersion of NaCl.

In the rest of the chapter, we provide the theoretical framework in section 6.2: The long-range interactions and the LO-TO splitting phenomenon in crystal structures are summarized in subsection 6.2.1, and a short review of the development and use of machine learning artificial neural network interatomic potentials (ANNIPs) is given in subsection 6.2.2. The modifications of the methodology adopted in order to include treatment of long-range interaction are reported in subsection 6.2.3. Data generation and training set preparation as well as the neural network architecture used for the phonon dispersion calculations are explained in the computational details section (6.3). In section 6.4, we start with an analysis of the effect of long-range interactions on the LO-TO splitting. We continue with a comparison of phonon dispersion calculations with and without considering long-range interactions. Then, we end up incorporating long-range interactions into the potential model. In the conclusions (section 6.5) we summarize our key findings, the importance of considering long-range interactions in accurate phonon dispersion calculations, and the potential impact and future prospects of the research.

6.2 THEORETICAL BACKGROUND

In this section, we assume familiarity with the *ab initio* lattice dynamics concept (DFPT), as discussed in Section 2.3 and we refer to it in due time. The primary focus of this chapter is to explore the long-range interactions and the LO-TO splitting phenomenon in crystal structures. Following that, a concise introduction to artificial neural network interatomic potentials (ANNIPs) will be provided.

6.2.1 Long range interactions and the LO-TO splitting phenomenon

In the theoretical section 2.3, I discussed the methods employed to calculate the vibrational properties of materials. Building upon that discussion, we can now explore the characteristics of long-wavelength vibrations in polar materials.

In polar semiconductors and insulators, the long-range nature of the Coulomb forces results in the emergence of macroscopic electric fields for longitudinal optic (LO) phonons in the limit of long wavelengths.

At finite wavelengths, the treatment of polar semiconductors is similar to that of non-polar materials. However, in the long-wavelength limit, the phonons become coupled to macroscopic electric fields, requiring careful consideration due to the non-lattice-periodic nature of the corresponding electronic potential, $V_E(\mathbf{r}) = e\mathbf{E}\cdot\mathbf{r}$.

A comprehensive understanding of the interaction between zone-center phonons and macroscopic electric fields can be attained through Huang's phenomenological model [15]. Here, we briefly discuss this model within the context of a cubic (or tetrahedral) lattice consisting of two atoms per unit cell. The general quadratic expression for the energy, as a function of the phonon optic coordinates ($\mathbf{u}$) and the electrical degrees of freedom ($\mathbf{E}$), is given as follows:

$$E(\mathbf{u},\mathbf{E}) = \frac{1}{2}M\omega_0^2 u^2 - \frac{\Omega}{8\pi}\epsilon_\infty E^2 - Z^*\mathbf{u}\cdot\mathbf{E}\,. \tag{6.2.1}$$

In this equation, M represents the nuclear-reduced mass, Ω denotes the volume of the unit cell, ϵ_∞ corresponds to the electronic dielectric constant of the crystal (i.e., the static dielectric constant with fixed nuclei, $\mathbf{u} = 0$), and the coupling term between $\mathbf{u}$ and $\mathbf{E}$ is defined as Z^*, referred to as the Born effective charge of the ions (see section 1.5 of Ref. [16] for more details). The variables conjugate to $\mathbf{u}$ and

$\mathbf{E}$ are the force acting on the ions ($\mathbf{F}$) and the electrical induction ($\mathbf{D}$), respectively. These vectors can be defined as:

$$\mathbf{F} \equiv -\frac{\partial E}{\partial \mathbf{u}} = -M\omega_0^2\mathbf{u} + Z^*\mathbf{E}\ , \tag{6.2.2}$$

$$\mathbf{D} \equiv -\frac{4\pi}{\Omega}\frac{\partial E}{\partial \mathbf{E}} = \frac{4\pi}{\Omega}Z^*\mathbf{u} + \epsilon_\infty\mathbf{E}\ . \tag{6.2.3}$$

When there are no free external charges present, Maxwell's equations yield the following results:

$$\boldsymbol{\nabla}\times\mathbf{E} = 0 \quad \sim \quad i\mathbf{q}\times\widetilde{\mathbf{E}} = 0, \tag{6.2.4}$$

$$\boldsymbol{\nabla}\cdot\mathbf{D} = 0 \quad \sim \quad i\mathbf{q}\cdot\widetilde{\mathbf{D}} = 0. \tag{6.2.5}$$

For transverse modes ($\widetilde{\mathbf{E}} \perp \mathbf{q}$), from 6.2.4 and 6.2.2, we obtain $\widetilde{\mathbf{E}}_T = 0$ and $\mathbf{F}_T = -M\omega_0^2\mathbf{u}$, and the transverse optical frequency is therefore $\omega_T = \omega_0$. For longitudinal modes ($\widetilde{\mathbf{E}} \parallel \mathbf{q}$), on the other hand, the equation 6.2.5 and 6.2.3 result in $\widetilde{\mathbf{D}}_L = 0$ and $\widetilde{\mathbf{E}}_L = -\frac{4\pi Z^*}{\Omega\epsilon_\infty}\mathbf{u}$. This leads to $\mathbf{F}_L = -(M\omega_0^2 + \frac{4\pi Z^*}{\Omega\epsilon_\infty})\mathbf{u}$. The longitudinal optical frequency is therefore $\omega_L = \sqrt{\omega_0^2 + \frac{4\pi Z^*}{\Omega\epsilon_\infty M}}$. These findings, which hold exactly for cubic and tetrahedral systems, can be readily extended to crystals with any arbitrary symmetry [16].

To obtain ϵ_∞ and Z^* through first-principles calculations, one can start from Eqs. 6.2.2 and 6.2.3. Expressing Eq. 6.2.3 in terms of the macroscopic electric polarization of the medium and extending to systems with multiple atoms per cell, one arrives at:

$$\mathbf{P} = \frac{1}{\Omega}\sum_s Z_s^*\mathbf{u}_s + \frac{\epsilon_\infty - 1}{4\pi}\mathbf{E}\ . \tag{6.2.6}$$

Note that, in general, for a low-symmetry case, Eq. 6.2.6 should be interpreted as a tensor equation, indicating that the Born effective-charge tensor of the s-th atom in the unit cell is obtained as the partial derivative of the macroscopic polarization with respect to a periodic displacement of all ions belonging to the s-th sublattice, with zero macroscopic electric field applied:

$$Z_s^{*\alpha\beta} = \Omega\frac{\partial P_\alpha}{\partial u_s^\beta(\mathbf{q}=0)}\bigg|_{E=0}\ , \tag{6.2.7}$$

and the electronic dielectric constant tensor is obtained from the derivative of the macroscopic polarization with respect to the macroscopic electric field when the nuclei are kept fixed:

$$\epsilon_{\infty}^{\alpha\beta} = \delta_{\alpha\beta} + 4\pi \frac{\partial \mathbf{P}_{\alpha}}{\partial \mathbf{E}_{\beta}}\bigg|_{\mathbf{u}_s(\mathbf{q}=0)=0} . \tag{6.2.8}$$

In the long wave-length limit, the force constant matrix can be divided into the combination of an analytical component and a non-analytical contribution [15, 22].

$$\widetilde{C}_{st}^{\alpha\beta} = \widetilde{C}_{st}^{(an)\ \alpha\beta} + \widetilde{C}_{st}^{(na)\ \alpha\beta} . \tag{6.2.9}$$

The analytical part of the matrix, $\widetilde{C}_{st}^{(an)\ \alpha\beta}$, can be obtained from the response to a zone-center phonon, computed with no macroscopic electric field applied. The non-analytical part takes on the general form [22], as below:

$$\begin{aligned} \widetilde{C}_{st}^{(na)\ \alpha\beta} &= \frac{4\pi}{\Omega} \frac{\sum_{\gamma} Z_s^{*\gamma\alpha} q_{\gamma} \sum_{\nu} Z_t^{*\nu\beta} q_{\nu}}{\sum_{\gamma,\nu} q_{\gamma} \epsilon_{\infty}^{\gamma\nu} q_{\nu}} \\ &= \frac{4\pi}{\Omega} \frac{(\mathbf{q} \cdot \mathbf{Z}_s^*)_{\alpha} (\mathbf{q} \cdot \mathbf{Z}_t^*)_{\beta}}{\mathbf{q} \cdot \epsilon_{\infty} \cdot \mathbf{q}} . \end{aligned} \tag{6.2.10}$$

Equation 6.2.10 demonstrates that all the essential information required to handle the non-analytical portion of the dynamical matrix can be found in the system's macroscopic dielectric constant (ϵ_{∞}) and the Born effective charges (Z^*). On the other hand, the analytic contribution can be computed by disregarding any macroscopic polarization linked to the phonon. All of these quantities can be readily obtained through Density Functional Perturbation Theory (DFPT) [42].

It is important to note that effective charges can also be computed using a method for the electrostatics of quantum dielectrics, relying on topological concepts, known as Berry's phase approach to macroscopic polarization [57, 99]. When both the linear response and Berry's phase approaches are applied with the same level of precision, they produce identical outcomes within numerical uncertainties [7].

6.2.2 Artificial Neural Network Interatomic Potential

In recent years, machine learning (ML) techniques are gaining popularity in computational material science, particularly concerning the creation of interatomic potentials suitable for studying extended systems [4, 103]. This popularity arises from their ability to effectively approximate high-dimensional potential energy surfaces. In essence, an ML model is built starting from the atomic coordinates of a given configuration, which are fed to a flexible representation of the corresponding energy whose parameters are adjusted to fit ab initio data.

Actually, employing a direct energy mapping approach with atomic coordinates as input is problematic, as ML algorithms typically assume an input of a fixed dimension, and systems with different numbers of atoms would not be easily dealt with; moreover coordinate translations, rotations, and permutations between atoms of the same species are all operations on the atomic configuration that should leave the predicted energy unchanged which is hard to impose if the energy predictor directly depends on the atomic coordinates. Therefore the atomic configuration is pre-processed in order to obtain a (fixed dimension) representation (of the local atomic environment) that complies with known symmetries. Several examples of such representations can be found in the literature, including vectors relative to local frames [132], symmetry-based descriptors [9, 11, 38], graphs [139], matrices [104], lists of bonds [48], chemical formulas [64], or molecular structures [127].

Once a suitable representation is selected, it becomes possible to construct a fast and precise interatomic potential using machine learning models like neural networks [10, 53, 144] or Gaussian processes [27, 70, 103]. In this scenario, the total energy of a specific atomic configuration is derived by summing up the atomic energy contributions, with each atomic energy relying on the representation of the chemical environment surrounding that particular atom. Since 2007 [11], this atomic decomposition approach has utilized artificial neural networks in conjunction with atom-centered symmetry descriptors to approximate the potential energy of many materials.

Subsequently, other machine learning (ML) approaches have emerged in the literature. These include the Gaussian Approximation Potential (GAP) [8, 9], wherein the atomic energy of a specific environment is expressed as a linear combination of the Gaussian kernel between the test environment and all the environments in the training dataset. Additionally, the Spectral Neighbor Analysis Potential (SNAPs) [123] method has been developed which represents a linearized version of the GAP method in the descriptors, with a recent extension to include quadratic dependence [137]. Another noteworthy approach is the Moment Tensor Potentials (MTPs) [112], where the interatomic potential is obtained from a linear combination of symmetry-abiding polynomial basis functions related to atomic environments, constructed from a set of moment polynomials, and so on. A recent (2020) study, which compared these methods, reached the conclusion that the GAP method exhibits the highest accuracy, albeit at the expense of the highest computational cost, which grows with the size of the training dataset [154]. In contrast, SNAP and MTP employ lower-cost regression strategies to establish correlations between the local atomic environment and its impact on the total

energy. Even more recent studies advocate superior performance for interatomic potentials based on graph neural networks.

In this study, we utilize the ANN approach in combination with Behler and Parrinello's atom-centered descriptors [11] and their modifications [75, 117], as implemented in the in-house developed PANNA code [75]. The resulting ANN interatomic potentials exhibit flexibility and can be efficiently computed. They offer continuity and are relatively inexpensive when compared to the other methods mentioned earlier [8, 9, 112, 123, 137]. Additionally, their derivatives can also be efficiently computed.

The ANN architecture considered is a simple feed-forward neural networks (FFNNs), where the input layer (the atomic environment descriptor) is processed by a number of hidden layers and results in the atomic energy estimate (in the output layer). Each node in a layer receives signals from the preceding layer through weighted connections; the signals are processed through non-linear functions before being passed to the next layer until reaching the output layer for the atomic energy prediction.

The complex relationship between the input and output nodes, facilitated by the multilevel processing of the input layer and the high connectivity among consecutive nodes in a fully connected FFNN, enables the construction of a high-dimensional potential energy surface.

As already mentioned, in this study we utilize the atomistic neural network approach proposed by Behler and Parrinello [11]. This approach defines the total energy of an N-atom system as the sum of atomic energy contributions:

$$E = \sum_{i=1}^{N} E_i(G^{(i)}) \, . \tag{6.2.11}$$

In this equation, E_i represents the energy contribution of an atom i, while $G^{(i)}$ denotes its local environment descriptor vector [75, 109].

To make the discussion clear, we can consider a small architecture with 2 hidden layers containing 4 and 3 nodes, respectively, and an output layer with a single node (illustrated in Fig. 6.1).

In this architecture, the atomic environment of atom i is described by a 3-dimensional vector and fed into the NN architecture. The prediction of the atomic energy E_i by the network is given by the following equation [1]:

$$E_i = g_3\left(b_1^{(3)} + \sum_{j=1}^{3} W_{1j}^{(3)} g_2\left(b_j^{(2)} + \sum_{k=1}^{4} W_{jk}^{(2)} g_1\left(b_k^{(1)} + \sum_{m=1}^{3} W_{km}^{(1)} G_m^{(i)}\right)\right)\right) , \tag{6.2.12}$$

1 In this equation, we employ a feed-forward all-to-all connected ANN architecture.

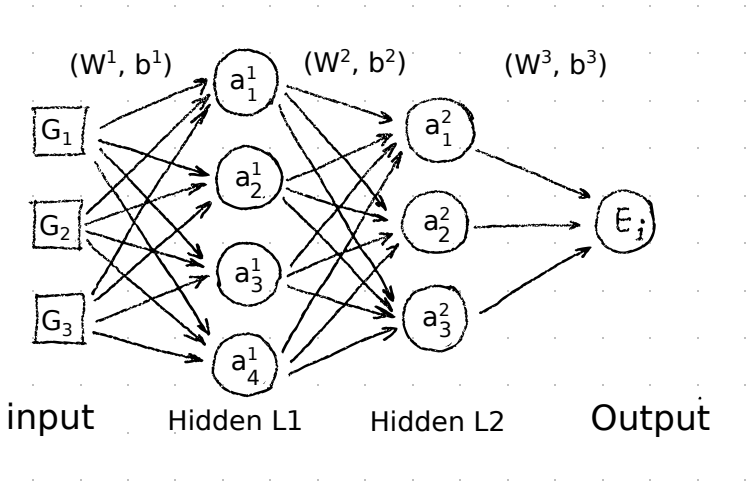

Figure 6.1: A schematic representation of an ANN with three inputs, two hidden layers, and an output layer that gives the atomic energy in this case. Each passing of information between layers l and $l+1$ is defined by the pair $(W^{(l+1)}, b^{(l+1)})$

where g_1, g_2, and g_3 are non-linear functions in general called the activation functions. The activation function for each node is specified by two parameters, the weight matrix W and the bias scalar b. Note that: (i) The non-linear function g_n (n: the number of layers) is differentiable with respect to its argument. (ii) Gaussian or hyperbolic tangent functions are commonly used for the hidden layers. (iii) In practice, a linear activation function is typically employed for the output layer, allowing for an arbitrary shift in the energy.

After building the ANN model, the weights and biases are determined by minimizing an objective function that quantifies the difference between the predicted value and the reference value.

To complete the definition of the trainable ANN model the "Atomic Environment Descriptors" must be specified, and various types of descriptors are available, each with its own strengths and weaknesses. In our implementation with PANNA we primarily concentrate on two widely used descriptors, initially proposed by Behler and Parrinello [11] with subsequent modifications proposed in [75, 117].

Both descriptors encapsulate the chemical environment of an atom through a fixed-size vector, which is determined by considering all other atoms found within a specified spherical cutoff, defined by the user.

The radial descriptor function, describing a two-body term, is defined as:

$$G_i^{Rad}[s] = \sum_{j \neq i} \exp\Big(-\eta(R_{ij} - R_s)^2\Big) f_c(R_{ij}) \tag{6.2.13}$$

In this expression, the descriptor involves user-defined resolution parameter η and a set of Gaussian centers, R_s. The summation over j

accounts for all atoms located within the cutoff distance R_c from the central atom i. The cutoff function, denoted by f_c, ensures a gradual decay to zero at the cutoff radius, and its definition is as follows:

$$f_c(R_{ij}) = \begin{cases} \frac{1}{2}\left[\cos\left(\frac{\pi R_{ij}}{R_c}\right) + 1\right] & R_{ij} \leqslant R_c \ , \\ 0 & R_{ij} > R_c \ . \end{cases} \tag{6.2.14}$$

The angular descriptor function, describing a three-body term, associated with the central atom i, is defined as:

$$\begin{aligned} G_i^{Ang}[s] =& 2^{1-\zeta} \sum_{j,k\neq i} \left(1 + \cos(\theta_{ijk} - \theta_s)\right)^{\zeta} \\ & \times \exp\left(-\eta(R_{ij}/2 + R_{ik}/2 - R_s)^2\right) f_c(R_{ij}) f_c(R_{ik}) \ . \end{aligned} \tag{6.2.15}$$

Here, the summation encompasses all pairs of neighboring atoms of atom i, denoted by j and k, where their distances R_{ij} and R_{ik} fall within the specified cutoff radius R_c, and forming an angle θ_{ijk} with atom i. The descriptor incorporates user-defined resolution/shape parameters, η and ζ, and a sets of reference angles, θ_s, and distances, R_s.

It is important to note that in Eq. 6.2.13, the summation over j is performed for each species type separately, resulting in the dimension of the radial part of the descriptors growing linearly in the number of species. Similarly, in Eq. 6.2.15, the double sum is selectively conducted over pairs of species types. Therefore, the dimension of the angular part of the descriptor scales quadratically with the number of species (i.e., $n_s \times (n_s + 1)/2$ for n_s species). The accuracy of an ANN interatomic potential relies heavily on an accurate description and sampling of the relevant chemical environments. Therefore, constructing a flexible and transferable ANN interatomic potential when many chemical species are present may be challenging as it necessitates a thorough account of the possible chemical environments and a careful sampling of the corresponding configuration space.

6.2.3 Artificial Neural Network with Long-Range Considerations

The ANN interatomic potentials described in the previous section define the total energy of the system as a sum of environment-dependent atomic contributions based on short-range information (up to R_c), they cannot therefore describe long-range interactions that extend beyond the specified spherical cutoff distance, R_c. Indeed, they neglect interactions in systems involving charge transfer (e.g., ionic systems like sodium-chloride or Li adsorption in carbon networks) that decay with distance according to a $1/r$ decay. Similarly, short-range atom-centered schemes fail to accurately

describe systems with significant van der Waals interactions resulting from non-local density fluctuations (e.g., molecular crystals or graphite). While the current study will not address van der Waals interactions, despite their significant importance for the stability of certain systems, we will discuss the development needed in order to account for long-range electrostatic interactions that primarily stabilize ionic systems, such as for instance Na-Cl.

Soon after Behler and Parrinello introduced atom decomposition of the total energy allowing the application of ML-based potentials to extended systems, it was recognized that these high-dimensional NNP (HDNNP) potentials lack the ability to describe long-range electrostatic interactions.

In 2012, Morawietz *et al.* [82] made an attempt to address this limitation by developing an interatomic potential for the water dimer. Their approach involved incorporating long-range electrostatic interactions through environment-dependent atomic charges, in addition to short-range atomic energies. Two distinct neural network models were created: one for the atomic charges, and the other for the model's parameters. In this approach, the training of the total energy is conducted in two stages: (i) The electrostatic Coulomb energy is calculated based on the environment-dependent charges, trained using Hirshfeld charges [50]. This Coulomb energy is then subtracted from the total energy. (ii) The remaining energy, assumed to be short-ranged in nature, is trained using short-ranged atomic neural network. In this approach training on a specific, though arbitrary, charge decomposition, in the specific example the Hirshfeld decomposition [50], is needed and charges are trained to be a function of the local chemical environment only.

An alternative method for incorporating long-range electrostatic interactions into artificial neural network interatomic potentials is through the utilization of the charge equilibration scheme introduced by Ghasemi *et al.* [40]. While initially designed as a general method for constructing artificial neural network potentials (ANNP) that encompass both short-range and long-range contributions, it has predominantly demonstrated success in constructing ANNP for ionic systems [32, 40, 47]. The core concept revolves around the notion that environment-dependent atomic charges can be derived from short-ranged environment-dependent atomic electronegativities using a charge equilibration scheme [98].

Through its design, this approach permits non-local charge redistribution, unlike the scheme proposed in Reference [82], where charges are solely determined by the local environment. The total energy expression is similar to the conventional total energy in the charge equilibration scheme (see Reference [98]), with the exception that the Coulomb energy from point charges is replaced by the

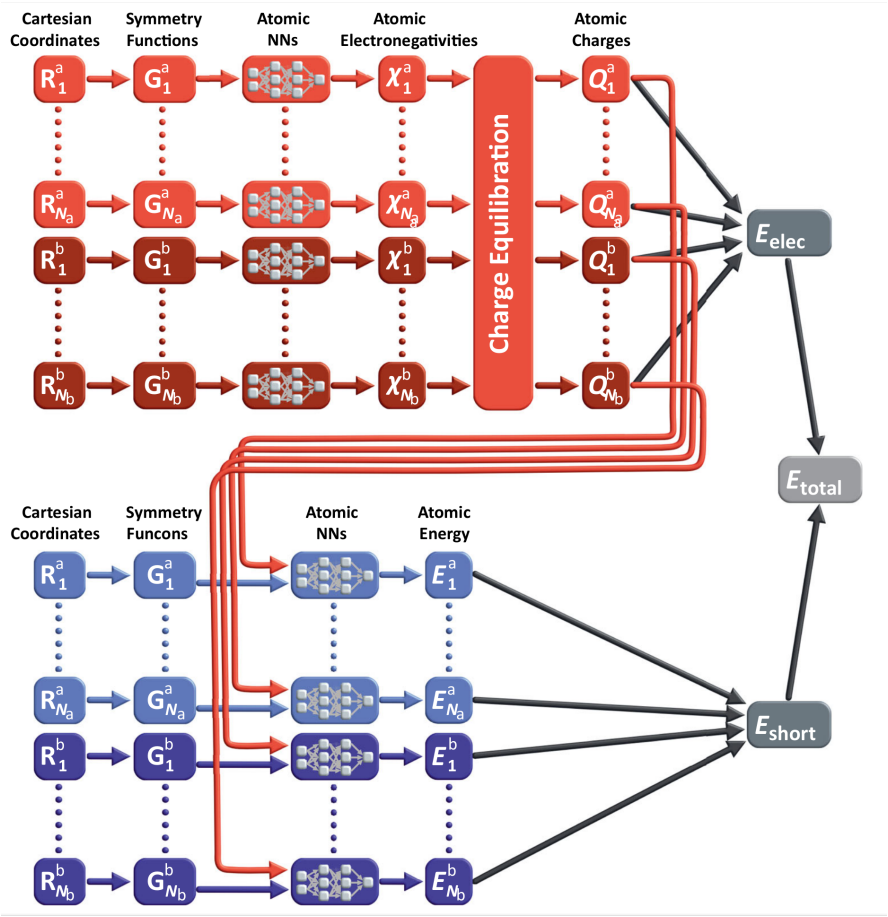

Figure 6.2: Diagram of a 4G-HDNNP structure applied to a binary system with N_a and N_b atoms. The system's total energy comprises short-range energy (E_{short}) from atomic energies (E_i) and long-range electrostatic energy (E_{elec}) determined by atomic charges (Q_i). Atomic charges are found using a method involving atom-specific electronegativities (χ_i) produced by atomic neural networks (red). These charges are used to compute electrostatic energy and serve as input for short-range atomic neural networks (blue), generating atomic energies. Atomic configurations are represented by symmetry function vectors (G_i) based on atom positions (R_i), which are used as inputs for the atomic neural networks. (Image is adapted from Tsk wai Ko *et al.* (2021) [60])

Hartree energy originating from a Gaussian charge Hirshfeld-like decomposition of the self-consistent density. The steps involved in predicting the total energy are as follows: (i) develop a neural network for the environment-dependent electronegativity, χ, and (ii) use a linear system to calculate the atomic charges, q. The linear system arises from minimizing the total energy while adhering to charge neutrality conditions, and subsequently, (iii) calculates the total energy based on χ and q.

In a recent development the two approaches have been combined in the so-called fourth generation high-dimensional NNP (4G-HDNNP) [60] where the electrostatic energy, computed from atomic charges obtained from the charge equilibration scheme, is supplemented by a short-range neural network interatomic potential whose input includes, in addition to the usual chemical environment description, also the previously determined local atomic charges. A schematic representation of the workflow involved in this approach is given in Fig. 6.2, reproduced from Reference [60].

One annoying feature of this scheme is the fact that the minimization problem the local charges are obtained from is not the total energy they contribute to define. Apart from the lack of neatness, this has as a consequence that when computing forces on atoms the variation of the charges with atomic positions needs to be explicitly accounted for, since no Hellmann-Feynman-like theorem applies.

In this study, to depict long-range electrostatic interactions we opt for the charge equilibration scheme as recently implemented in the PANNA code [75, 109, 110] due to its several advantages:

- It eliminates the need to choose an arbitrary decomposition of the *ab initio* charge density into atomic components and train on them, although charges can still be constrained during training if such information is available.
- By construction, it ensures charge neutrality is fulfilled.
- The scheme allows for long-range charge transfer.
- The local charges are obtained from the minimization of the total energy functional they contribute to define, thus simplifying force calculations.

The total energy of a specific configuration is split into two components: a charge-dependent short-range part, described by standard atomic energy contributions, and a long-range part, making use of the charge equilibration scheme. Consequently, the total energy can be expressed as follows:

$$E_{tot} = E_{SR} + E_{LR} \, . \tag{6.2.16}$$

The short-range energy (E_{SR}) can be generally expressed as the sum of environment-dependent atomic energies ($E_i(G(\{r_i\}), q_i)$), whose charge dependence can be conveniently expanded up to second order as:

$$E_{SR} = \sum_i \left[E_i^{(0)}(G_i) + \left(E_i^{(1)}(G_i) + \chi_i^0 \right) q_i + \frac{1}{2} \left(E_i^{(2)}(G_i) + J_i^0 \right) q_i^2 \right] , \tag{6.2.17}$$

where $\chi_i = E_i^{(1)}(G_i) + \chi_i^0$ represents the environment-dependent atomic electronegativity, while $J_i = E_i^{(2)}(G_i) + J_i^0$ denotes the environment-dependent atomic hardness. The Long-range part of the energy is the Coulomb energy defined in terms of the total charge density $\rho(r)$ as:

$$E_{LR}[\rho] = \frac{e^2}{8\pi\epsilon_0} \sum_R \int \frac{\rho(\mathbf{r})\rho(\mathbf{r'})}{|\mathbf{r} - \mathbf{r'} + \mathbf{R}|} d^3r d^3r' \, . \tag{6.2.18}$$

This energy term, E_{LR}, is composed of atom-specific components and a Hartree term (specifically for periodic systems), which characterizes the effective interaction between the charge density at r and r'.

The total charge density results from the superposition of spherical Gaussian functions centered on each atom i located at position r_i. These functions are normalized to ensure that the charge density integrates with the total number of electrons in the system. Consequently, the atom-centered charge density is described as follows:

$$\rho_i(\mathbf{r}) = \frac{q_i}{\alpha_i^3 \pi^{3/2}} \exp\left\{ -\frac{|\mathbf{r} - \mathbf{r}_i|^2}{\alpha_i^2} \right\} , \tag{6.2.19}$$

where q_i denotes the charge on atom i, and α_i represents the Gaussian width of atom i, determining the spatial extent of the charge density surrounding it. The resulting total density at location r is expressed as follows:

$$\rho(\mathbf{r}) = \sum_{i=1}^{N} \rho_i(\mathbf{r}) \, . \tag{6.2.20}$$

Charge equilibration is obtained by minimizing the charge-dependent total energy expression, containing

environment-dependent learned parameters, χ_i and J_i, and some atom-dependent constants, γ_{ij}:

$$E_{Qeq} = \sum_i \left[\chi_i q_i + \frac{1}{2}(J_i + K\frac{2\gamma_{ij}}{\sqrt{\pi}})q_i^2\right] + \frac{K}{2}\sum_{i\neq j} q_i q_j \frac{erf(\gamma_{ij}|\mathbf{r}-\mathbf{r'}|)}{|\mathbf{r}-\mathbf{r'}|} . \quad (6.2.21)$$

Note that in systems lacking periodicity, the Hartree energy can be computed analytically in real space. Indeed, upon conducting the integration, and considering $K = \frac{1}{4\pi\epsilon_0}$ and $\gamma_{ij} = \frac{1}{\sqrt{\alpha_i^2+\alpha_j^2}}$ we can obtain equation 6.2.21.

For periodic systems, on the other hand, the Hartree energy term in this study is calculated in reciprocal space with an Ewald-like expression. The resulting long-range term is then given by:

$$E_{Qeq} = \sum_i \left[\chi_i q_i + \frac{1}{2}J_i q_i^2\right] + \frac{K}{2}\sum_{i\neq j} q_i q_j \frac{4\pi}{\Omega}\sum_{G\neq 0}\frac{\exp(i\mathbf{G}.\mathbf{r}_{ij})}{G^2}\exp\left(-\frac{G^2}{4\gamma_{ij}^2}\right) . \quad (6.2.22)$$

By introducing a generic potential V_{ij}, which differs according to the relevant periodic boundary conditions, we can express E_{LR} concisely as:

$$E_{Qeq} = \sum_i \left[\chi_i q_i + \frac{1}{2}J_i q_i^2\right] + \frac{K}{2}\sum_{i,j} q_i q_j V_{ij} , \quad (6.2.23)$$

where V_{ij}, for a system with periodic boundary conditions, is:

$$V_{ij}^{(PBC)} = \frac{4\pi}{\Omega}\sum_{\mathbf{G}\neq 0}\frac{\exp(i\mathbf{G}\cdot\mathbf{r}_{ij})}{G^2}\exp\left(-\frac{G^2}{4\gamma_{ij}^2}\right) , \quad (6.2.24)$$

and, for a system without periodic boundary conditions, it becomes:

$$V_{ij}^{(NoPBC)} = \frac{erf(\gamma_{ij}|\mathbf{r}-\mathbf{r'}|)}{|\mathbf{r}-\mathbf{r'}|}(1-\delta_{ij}) + \frac{2\gamma_{ij}}{\sqrt{\pi}}\delta_{ij} . \quad (6.2.25)$$

To determine the atomic charges, we minimize the total energy with respect to q_i while maintaining charge conservation constraint ($\sum_i q_i = q_{tot}$) by using a Lagrange multiplier:

$$\frac{\partial}{\partial q_i}\left[E_{tot} - \lambda(q_{tot} - \sum_i q_i)\right] = 0 , \quad (6.2.26)$$

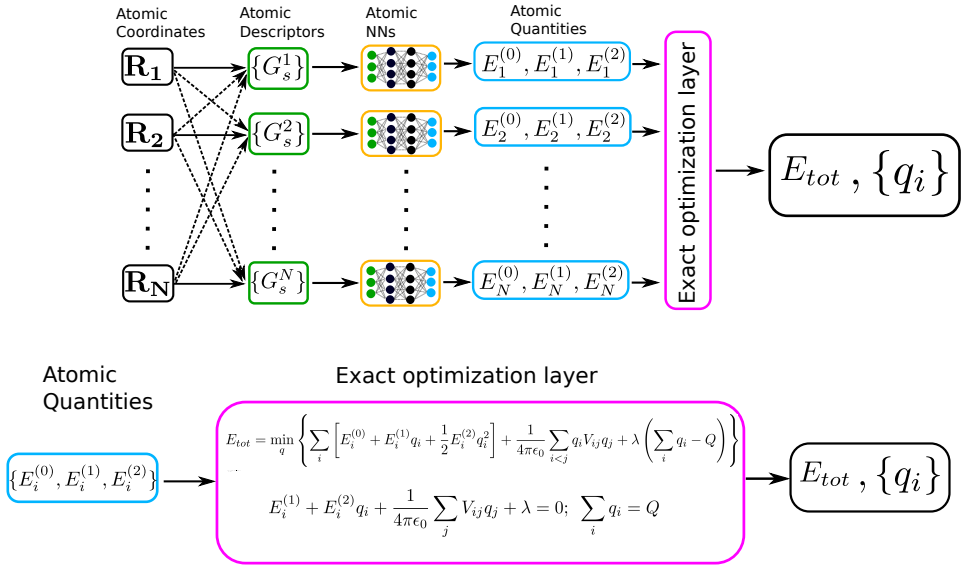

Figure 6.3: A schematic representation of long-range workflow from Ref. [110] (implemented in PANNA) for a system consisting of N atoms is as follows: For each atom i with Cartesian coordinate R_i, a descriptor G_i is constructed and serves as input to the atomic neural network. Each atomic network generates three atomic quantities, $E_i^{(0)}$, $E_i^{(1)}$, and $E_i^{(2)}$. These outputs are then utilized to compute the atomic charges using the charge equilibration scheme as described in Eq. 6.2.27. Subsequently, the short-range energy contribution E_{SR} is obtained from Eq. 6.2.17, and the Coulomb energy, E_{LR}, is computed based on the atomic charges. The sum of these energies represents the prediction for the total energy.

which leads to:

$$\sum_j \left[J_i(G_i)\delta_{ij} + V_{ij} \right] q_j + \chi_i(G_i) + \lambda = 0 \, . \tag{6.2.27}$$

Using the environment-dependent atomic electronegativity and hardness, χ_i and J_i, and the charge neutrality condition, $\sum_i q_i = q_{tot}$, the atomic charges can be calculated by solving the system of equations for the specific values of the atomic Gaussian width, α_i.

The complete procedure for computing the total energy using this approach, as implemented in PANNA, consists therefore in the following steps (illustrated in Fig. 6.3):

- Utilize the neural network to predict the atomic electronegativity and hardness based on each atomic environment descriptor.
- Calculate the atomic charges by solving the linear system described in equation 6.2.27.

- Compute the charge equilibration energy term, E_{Qeq}, by using the computed charges in equation 6.2.23.
- Predict the environment-dependent atomic energy term, $E_i^{(0)}(G_i)$.
- Finally, obtain the predicted total energy, E_{tot}, using equation 6.2.16.

The short-range contribution to the force on each atom can be computed as:

$$F_i^{SR} = -\sum_{\alpha=0}^{2}\sum_{j,\mu}\frac{\partial E_j^{(\alpha)}}{\partial G_{j\mu}}\frac{\partial G_{j\mu}}{\partial \mathbf{R}_i}\, q_j^{\alpha}\,, \tag{6.2.28}$$

where j sums over atoms, μ over the elements of the environment vectors, and α over the network outputs. Then the Coulomb component of the force is:

$$\begin{aligned} F_i^{Coul} &= \sum_j F_{ij} q_i q_j\,, \\ F_{ij} &= \left[\frac{\mathrm{erf}(\gamma_{ik} R_{ij})}{R_{ij}^3} - \frac{2\gamma_{ij}}{\sqrt{2}R_{ij}^2}\exp\left(-\gamma_{ij}^2 R_{ij}^2\right)\right]\mathbf{R}_{ij}\,. \end{aligned} \tag{6.2.29}$$

Summing up these two contribution of forces leads to the total force on atom i. For more details see Refs. [109, 110] and references therein.

6.3 COMPUTATIONAL DETAILS AND METHODOLOGY

The interatomic potential used in the following experimental simulations on the impact of the long-range interactions on NaCl phonon dispersions was generated from a dataset of molten salt configurations previously generated and reported in [68] where it was used to generate an NNIP not including long-range term but using a very large cutoff radius of $R_C = 8$ Å.

Since the accuracy and variety of the training dataset configurations have an important impact on the resulting NNIP, I will briefly summarize the method, parameters, and generation strategy for this dataset.

As the selection of the training dataset plays a pivotal role in the construction of reliable NNIP and the target application involved molten salt properties, the main emphasis was placed on liquid properties, encompassing essential factors such as the melting point (T_m), heat capacity (C_P), thermal conductivity (λ), diffusion coefficient (D), density (ρ), molecular structure, and equation of state, among others. Moreover, a good NNIP should

be able to provide reasonably accurate predictions for common crystal properties as well. To achieve this, the training dataset was constructed by using an iterative augmentation approach that involved quick training-validation-augmentation cycles.

This approach, resembling active learning, enabled to effectively identify the configurations where NNIP predictions deviated most significantly from DFT results. Through the inclusion of these pertinent configurations into the training set, and subsequent retraining step, the robustness of the NNIP was enhanced with each iteration.

The final training dataset used in Ref. [68], and used to generate the long-range-aware NNIP (LR-NNIP) used in the following, includes a diverse set of configurations, covering normal liquids at different temperatures, compressed liquids, high-temperature liquids in confined volumes, non-1:1 ratio liquids, high-temperature crystals, zero-temperature crystals under various conditions, dimer configurations in the gas phase, and isolated atoms of Na and Cl. In total, the dataset contains approximately 112,000 configurations. For more information one should refer to Ref. [68].

The cutoff radius, R_C, used in the generation of the LR-NNIP was 5.3 Å and the size of local environment descriptors per atom was fixed to 80. A plug-in for the use of LR-NNIP in LAMMPS [124] was also available.

6.4 RESULTS AND DISCUSSION

As it is mentioned before, phonon calculations can be time-consuming, especially as the system size grows with more atoms. Traditional methods like DFPT (see Chapter 2, Subsec. 2.3) for phonon calculations become less practical in such scenarios. As an alternative, force-field-based phonon calculations can be used to obtain phonon dispersion. However, force-field-based vibrational methods have inherent inaccuracies, prompting the need to find ways to improve their precision.

In this study, we aim to enhance the accuracy and reliability of phonon dispersion calculations by using NNIP (see Subsec. 6.2.2). This approach is generally effective for metals but falls short in accurately predicting phonon dispersion for polar materials due to the neglect of long-range electric fields in NNIP. To address this challenge, several strategies can be employed, such as integrating long-range interactions into NNIP. The process of implementing the long-range correction in NN interatomic potentials has been detailed in Subsection 6.2.3. The expectation of this implementation is LO-TO splitting observation in polar material phonon dispersion [7].

As explained in Subsec. 6.2.1 LO-TO splitting is a manifestation of long-range interaction in polar material and insulators. It manifests itself in the long-wavelength limit ($q \to 0$) of phonon dispersion where longitudinally polarized vibrations can couple to a macroscopic electric field.

Although this phenomenon, LO-TO splitting at Γ point, is the natural effect of long-range correction, it needs some extra calculations to reach the manifestation of it in phonon dispersion. A well-known approach to add this extra calculation is still using a standard method like DFPT (explained in Subsec. 6.2.1). In this regard, we start with this consideration, which also helps us to confirm the accuracy of NNIP method, and keep the consistency with other results from other methods.

LAMMPS-interfaced libraries phonopy and phonolammps, as well as within fully *ab inito* DFPT calculations, cannot display LO-TO splitting when the standard periodic boundary conditions of zero macroscopic electric field are used, even when the interatomic force field used does sustain LR interactions, as illustrated in Fig. 6.4 (green lines) where the phonon dispersion of NaCl are shown as obtained from the LR-NNIP scheme described in the previous section without the inclusion of the non-analytic corrections (NAC): no LO-TO splitting is therefore present.

As an example of polar material, we investigate here the phonon dispersion of molten NaCl. The structure has been relaxed with NN potential trained by PANNA code, which is implemented in LAMMPS code[2]. After the relaxation process and reaching the ground state, phonon calculation is performed with phonopy and phonolammps libraries [126] of Python. These libraries are used to implement small displacement method to calculate phonon dispersion. One can add non-analytical correction (calculated with DFPT) as a flag to phonopy. Then it is possible to reach LO-TO splitting at Γ point (wave vector $q = 0$), as shown in Fig. 6.4.

Another approach to reaching correct vibrational properties in polar materials is to try to generalize the NNIP phonon calculation directly, which means using already existing building blocks to modify NNIP method. The first step was adding the long-range electric field to the NN interatomic potentials (explained in Subsec. 6.2.3). From Fig. 6.4, it is obvious that if we can implement the LO-TO splitting to phonon dispersion, we will reach the correct vibrational dispersion. By considering an analogy to DFPT method, we can write the total energy of the system as below:

2 For more information about LAMMPS and PANNA, see Refs. [124] and [75], respectively.

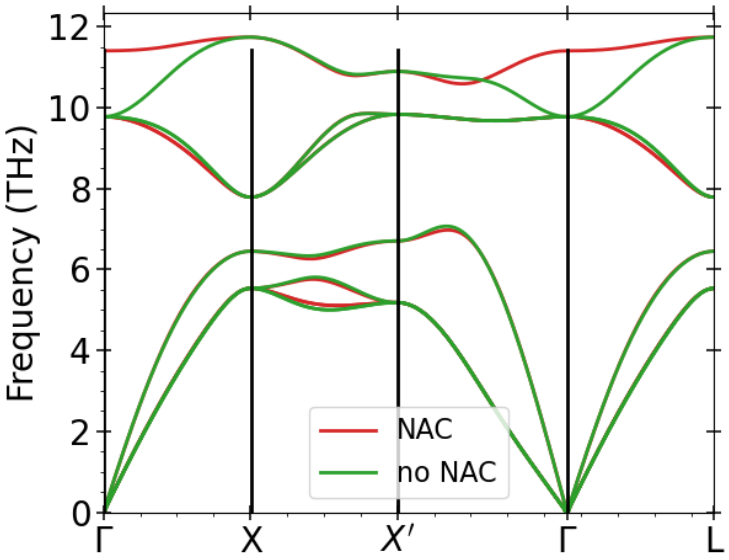

Figure 6.4: Phonon dispersion for NaCl subjected to NNIP, calculated with phonolammps, comparing the effect of non-analytical correction.

$$E^{VNN}(\{\mathbf{R}\}) = \min_{\{q\}} \Big[\sum_{I} E_I^0(\{\mathbf{R}\}) + \sum_{I} E_I^1(\{\mathbf{R}\})\ q_I + \frac{1}{2} \sum_{IJ} q_I \left(E_I^2(\{\mathbf{R}\})\delta_{IJ} + V_{IJ}(|\mathbf{R_I} - \mathbf{R_J}|) \right) q_J \Big], \tag{6.4.1}$$

This method can be completed by considering non-analyticity at $q = 0$ (Γ) and writing the matrix of force constant as splitting into analytical and non-analytical parts (Eq. 6.2.9). This separation lets us implement the desired correction to phonon dispersion. Then dynamical matrix is defined as the DFPT routine:

$$\widetilde{D}_{ij}^{\alpha\beta} = \frac{\widetilde{C}_{ij}^{\alpha\beta}}{\sqrt{M_i M_j}} \tag{6.4.2}$$

Finally, to generalize the results, our next step can be the implementation of atomic position perturbation, and the use of response theory to find effective charge (Z^*) and high-frequency static dielectric constant (ϵ^∞) directly. Using these quantities can lead to the non-analytical term, explained above, and consequently to the correct vibrational properties also for polar materials.

This hypothetic approach to generalizing the NNIP can succeed if and only if the long-range interaction is correctly implemented in the calculation. This fact motivates us to conduct simulation experiments to examine the method of NNIP with long-range correction.

First of all, we consider a slab of NaCl including 216 atoms. This slab will be subjected to different amounts of constant electric field

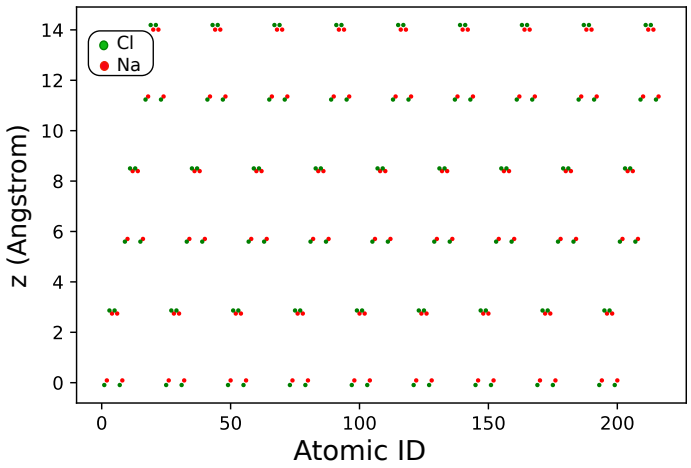

Figure 6.5: Displacements of Na^+ and Cl^- ions of slab subjected to NNIP with long-range correction after minimization without any external electric field.

(*e.g.* 0.005, 0.01, 0.02, 0.05, etc. (V/Å)), mimicking a capacitor with a polar insulator in between. This setup can examine the effect of the electric field on the slab, expecting polarization in the system. Due to the size of the slab, we also note that atoms are not completely in the bulk situation, meaning that they are subjected to displacement even without electric field effects (zero electric field) (see Fig. 6.5). The displacement of atoms subjected to 0.01, 0.02, and 0.05 V/Å electric fields along the z direction is plotted in Fig. 6.6. Then the charge variation in the presence of electric fields is investigated and illustrated in Fig. 6.7. Note that the values are normalized with respect to the corresponding electric field. The available evidence suggests that the partial screening of the electric field is insufficient to establish the polar behavior of the system when using NNIP with long-range correction. Further investigation and analysis are necessary to ascertain the true polar characteristics of the system.

6.5 CONCLUSION AND FUTURE DIRECTIONS

In summary, we calculate here the correct phonon dispersion for polar semiconductors, such as NaCl, governed by NNIP (trained by PANNA) with the manual and usual implementation of the non-analytical term. This is an indirect way to reach the LO-TO splitting in the Γ point and implies that we still need an *ab initio* code to calculate the Born effective charge and dielectric constant. The success of this modification is the starting point for thinking about the generalization of the existing method.

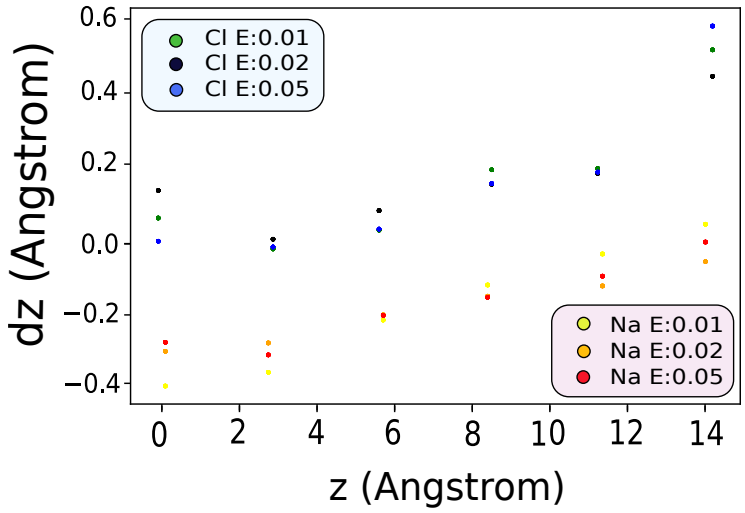

Figure 6.6: Displacements of Na^+ and Cl^- ions of slab subjected to NNIP with long-range correction, subjected to 0.01, 0.02, and 0.05 V/Å electric field.

Indeed, to reach the correct vibrational properties of materials, including metal and polar insulators, the next step can be the implementation of perturbation, and the use of response theory to find effective charge (Z^*) and high-frequency static dielectric constant (ϵ^∞) self-consistently. This method is only valid if the long-range interaction works properly, which is examined through a simulation experiment designed here. The evidence shows that ions of Na and Cl react to the implemented electric field and displace accordingly. However, this displacement does not mimic the bulk case, because of the size of the slab and surface effects. This is a good sign to urge us to investigate larger slabs in the future, and hopefully reach better results. On the other hand, since charge minimization, implemented in PANNA routine and introduced to LAMMPS, is required for long-range effects simulation, we try to understand the mechanisms and the effects of the electric field on charge in a slab of NaCl. Negligible charge transfer in this model confirms the partial screening of the electric field, which is not enough to prove the polar behavior of the system under NNIP with long-range correction.

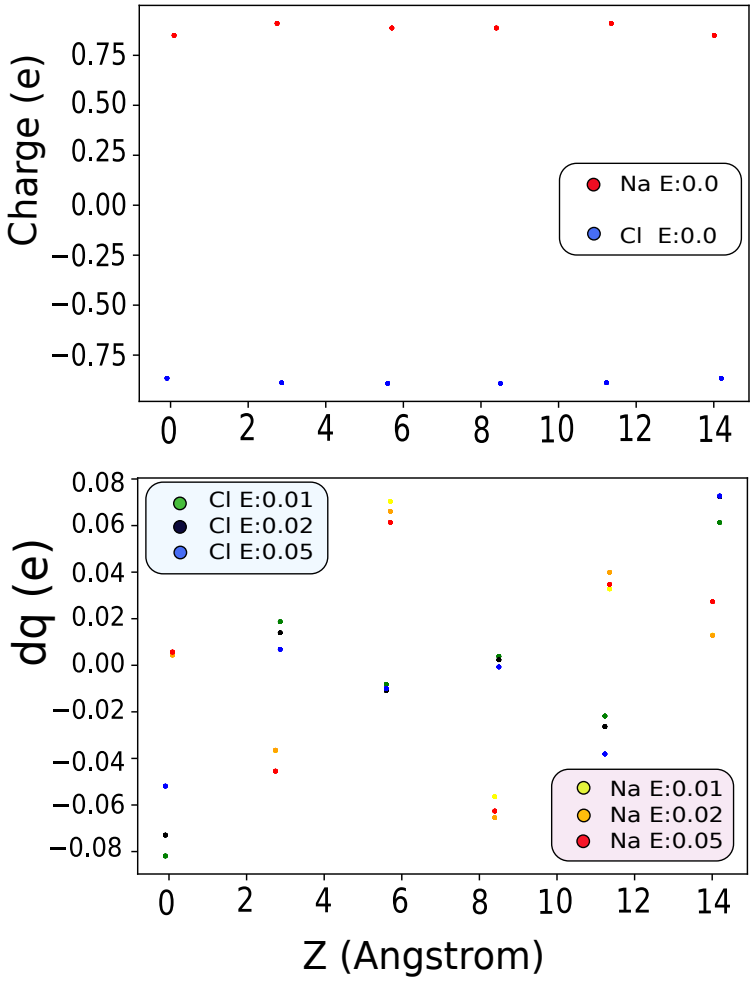

Figure 6.7: Variation of atomic charges after subjecting to different electric fields (0.01, 0.02, and 0.05 V/Å) (lower panel) with respect to the system with zero electric fields (upper panel).

7 CONCLUSION

By combining *ab initio* methods and structure prediction algorithm, we have performed an extensive search for the most energetically stable borophene polymorphs on Al(111) substrate to gain insight into the role of electron-deficiency compensation through both self- and charge-doping processes. This was the starting point to investigate geometric- and electronic-structure modifications induced by oxidation and hydrogenation as an alternative route to tune the coupling between borophene and the substrate, with respect to self-doping. In this thesis, by comparing our computational results with the (complementary) experimental findings of the growth of boron layers on the Al(111) termination, together with their oxidation and reduction, we unraveled the nature of the B–Al interaction, which ultimately defines the AlB_2 properties on this metal surface.

We conclude that oxygen, due to its high affinity with aluminum, yields passivation of the metal surface and tunes the charge transfer from the metal to borophene. The formation of B–O bonds is hardly observed in the decoupled borophene layers, mostly showing triangular bonding geometries close to the α, χ_3, and β_{12} structures rather than to the honeycomb layout. Since oxygen hinders the charge transfer from Al to borophene, the resulting electron deficiency is compensated by the formation of other bonding geometries with a higher average filling factor and pronounced buckling. Thus, our results reasonably put in evidence that, in the view of decoupling and stabilizing a honeycomb borophene phase by means of oxidation, the bonding energy between boron and metal substrate, oxygen and boron, and oxygen and metal substrate should be carefully balanced by a proper choice of the growth substrate. This may be accomplished *e.g.* by diluting Al and choosing an Al alloy as a supporting template with reduced Al–O interaction but, still, with sufficient available charge transfer attitude.

Moreover, both computational and experimental aspects agree that reduction involves only boron atoms, generating a stable, long-range ordered honeycomb structure and showing bridge-coordinated H atoms. Due to the strong B–Al interaction and sufficient charge transfer from the Al substrate, the H-hB layer does not yield a fully H-covered borane structure, with H atoms sitting at the surface-exposed bridge sites on the hB layer. The vibrational properties of borophane show its stability. All of these key findings confirm that hydrogenation can be addressed as a promising chemical

passivation treatment (which was done also by others) to reduce the boron-substrate interaction, thus stepping towards the synthesis of a stable, more decoupled honeycomb phase with interesting electron conductivity properties.

Given the specifics involved in phonon calculations, it is widely acknowledged that these simulations can be computationally demanding, particularly when dealing with larger systems containing more atoms. Traditional methods like DFPT for phonon calculations become less viable in such situations. In response, MD-based phonon calculations offer an alternative means to obtain phonon dispersion. Nevertheless, MD-based vibrational methods come with inherent inaccuracies, which highlight the importance of seeking methods to enhance their accuracy.

To tackle this problem, in this thesis, we try to calculate the correct phonon dispersion for polar semiconductors, such as NaCl, governed by NNIP (trained by PANNA) with the manual and usual implementation of the non-analytical term. This is an indirect way to reach the LO-TO splitting in the Γ point and implies that we still need an *ab initio* code to calculate the Born effective charge and dielectric constant. The success of this modification is the starting point for thinking about the generalization of the existing method.

Indeed, to reach the correct vibrational properties of materials, including metal and polar insulators, the next step can be the implementation of perturbation, and the use of response theory to find effective charge (Z^*) and high-frequency static dielectric constant (ϵ^∞) self-consistently. This method is only valid if the long-range interaction works properly, which is examined through a simulation experiment designed here. The evidence shows that ions of Na and Cl react to the implemented electric field and displace accordingly. However, this displacement does not mimic the bulk case, because of the size of the slab and surface effects. This is a good sign to urge us to investigate larger slabs in the future, and hopefully reach better results. On the other hand, since charge minimization, implemented in PANNA routine and introduced to LAMMPS, is required for long-range effects simulation, we try to understand the mechanisms and the effects of the electric field on charge in a slab of NaCl. Negligible charge transfer in this model confirms the partial screening of the electric field, which is not enough to prove the polar behavior of the system under NNIP with long-range correction.

A APPENDIX: COMPUTATIONAL DETAILS

In order to avoid repetition of calculation details in each chapter, this information is mentioned here.

All calculations conducted in this study were performed within the framework of density-functional theory and the plane-wave pseudopotential methods, which are well-established techniques for electronic structure calculations. The detailed methodology is provided in Section A.1 below, where we outline the specific procedures employed. Global structural search has been performed using genetic optimization algorithms, as described in Section A.2.

A.1 PLANE-WAVE PSEUDOPOTENTIAL TECHNIQUES

To ensure the accuracy and reliability of our calculations, we utilized the accurate projector augmented wave (PAW) method for pseudopotentials. The choice of pseudopotentials is crucial in accurately representing the electronic behavior of the system. In this regard, we followed the recommendations outlined in Ref. [94] and utilized the PAW pseudopotentials provided in Ref. [26].

The exchange-correlation (XC) functional used to account for electron-electron interactions was the generalized gradient approximation (GGA) parameterized by Perdew-Burke-Ernzerhof (PBE). This functional has been widely employed and has shown good performance in various systems [90]. Additionally, we incorporated van der Waals correction as proposed by Grimme and colleagues [45], which accounts for dispersion forces in systems where they are relevant.

In order to achieve accurate and converged results, appropriate energy cutoffs were chosen. The kinetic energy cutoff for the charge density was set to 350 Ry, while the energy cutoff for wavefunctions was set to 70 Ry. To reach these optimal values, the convergence calculations were performed carefully. These values ensure that the contributions from high-energy states are sufficiently included in the calculations, enabling accurate description of the electronic structure.

To account for any undesired dipole field that may arise at metal surfaces, we employed the dipole correction method introduced by

L. Bengtsson [12]. This correction effectively eliminates any artificial dipole moment that may affect the calculated properties of the system, thus enhancing the accuracy of the results.

Given the metallic nature of both borophene and aluminum, it was necessary to consider the partial occupation of energy levels around the Fermi level. To accomplish this, we employed the Marzari-Vanderbilt-DeVita-Payne cold smearing function [79] with a line-width of $\sigma = 0.01$ Ry. This approach allows for a smooth distribution of electrons within the occupied states, thereby ensuring a more accurate representation of the metallic behavior.

For Brillouin zone integration, a $(14 \times 14 \times 1)$ Monkhorst-Pack grid was utilized in the (2×2) surface unit cell of Al(111). This grid provides a suitable sampling of reciprocal space and ensures accurate integration of the electronic states over the Brillouin zone. In our investigation, we employed a sophisticated modeling approach for the aluminum substrate, utilizing a 5-layer slab model with the bottom 3 layers held fixed in their bulk positions. To account for the influence of slab edges, a 2-dimensional cutoff correction was implemented, ensuring an accurate representation of the system [118]. The purpose of this comprehensive setup was to accurately capture the interaction between borophane and the aluminum substrate.

To delve into the electronic characteristics of the borophene, borophene/aluminum, borophene/oxygen/aluminum, and borophane/aluminum system, we conducted extensive calculations of the density of states (DOS). By employing the occupation of tetrahedra method, we obtained a detailed DOS profile that offers valuable insights into the distribution and behavior of electronic states within the system. This information is crucial for understanding the material's band structure, magnetic properties, and transport phenomena. To ensure the reliability and consistency of our calculations, we utilized the same plane-wave basis set and pseudopotentials as those employed during the structural optimization phase. Convergence of the wavefunction was deemed achieved when the threshold was set to an impressively low value of 10^{-9} Ry, guaranteeing high precision and accuracy in our results.

In our pursuit of a comprehensive analysis, we extended our investigations to include partial density of states. This analysis allows us to discern the individual contributions of different atomic orbitals to the overall DOS, providing deeper insights into the electronic properties and bonding characteristics of the systems mentioned above. By unraveling the intricate interplay between atomic orbitals, we gain a clearer understanding of the material's electronic structure and its potential implications for various properties and phenomena.

Moreover, to explore the vibrational properties of the most stable configurations, we employed the powerful Density Functional

Perturbation Theory (DFPT) implemented in the widely used QUANTUM ESPRESSO package. By employing this method, we were able to determine the phonon frequencies at the Γ point of the Brillouin zone, offering critical insights into the material's vibrational behavior. Consistency was maintained by employing the same plane-wave basis set and pseudopotentials as in the structural optimization, ensuring reliable and meaningful comparisons.

Throughout the calculations, we paid careful attention to parameter optimization in order to achieve reliable and precise results. In particular, we ensured that the lattice parameter of the substrate was fixed at its bulk value of 4.038 Å, which is consistent with previous studies and experimental data. This choice maintains the structural integrity of the system and allows for a meaningful comparison with prior work.

By employing this comprehensive computational framework, and optimizing the relevant parameter, and analysis methodology, we aim to provide a thorough understanding of the electronic and vibrational properties of the borophane/aluminum system, we were able to obtain accurate and reliable results for the electronic and structural properties of the systems under investigation. These results also shed light on its potential applications and guide future experimental investigations.

A.2 GENETIC OPTIMIZATION

The investigation of the vast phase space and the exploration of various combinations of overlayer/surface structures were facilitated by the implementation of sophisticated (evolutionary) genetic methods in the USPEX software [85]. The genetic algorithm utilized in USPEX incorporates a range of variation operators, including heredity, mutation, and permutation, to efficiently explore the configuration space and identify energetically favorable structures.

In the initial stage of the genetic optimization process, multiple configurations are generated based on symmetry considerations rooted in crystallography principles. It more precisely means that for each stoichiometry, the genetic algorithm (GA) is initiated with randomly generated structures. The population size is determined as $2 \times N$ for N atom unit cells, or 50 when $2 \times N$ exceeds 50. The GA evolves through a combination of evolutionary operations, with 30% of structures produced through heredity, 10% through atomic mutation (also known as softmutation or coormutation), 10% through transmutation, and 50% as new random configurations. These configurations serve as the starting points for subsequent fully *ab initio* structural optimizations using the QE package [44]. The aim

is to determine the most energetically favorable structures accessible in the first generation. This goal will be achieved for each generation. The structures undergo two optimization steps. These steps include:

- (a) relaxation of atomic positions based on Hellmann Feynman theorem with 0.06 $Å^{-1}$ mesh resolution[1]. This relaxation continues until the total force components are less than 0.257 eV/Å (0.01 Ry/a.u.).
- (b) further relaxation of atomic positions again based on Hellmann Feynman theorem with 0.015 $Å^{-1}$ mesh resolution. This relaxation continues until the total force components are less than 0.025 eV/Å (0.001 Ry/a.u.).

Since this iterative process of generating new generations of structures, followed by *ab initio* optimizations, allows for the systematic exploration of the configuration space, enabling the identification of the most stable and promising structures.

The GA algorithm progresses for a maximum of 20 generations, following this procedure, resulting in a diverse range of polymorphs. Please note that 20 generations is the maximum threshold and will change based on the number of atoms we considered in the relaxation area.

Since the examined structures are surfaces, we need to specify the thickness of the surface (thickness of surface region (3.0 Å) as well as the thickness of buffer region in the substrate (4.0 Å)). The other atoms in the structure are fixed in their positions to mimic the bulk situation.

To ensure a comprehensive sampling of the configuration space and access to a wide variety of possible structures, different ratios of boron (or oxygen) to the aluminum surface were considered. This approach provides insight into the influence of different compositions on the stability and properties of the structures.

It is worth mentioning that the lattice parameters are optimized and the consistency with literature and other studies is preserved.

By utilizing the powerful genetic optimization methods implemented in USPEX, we were able to efficiently search the configuration space, identify the most energetically favorable

1 The determination and adjustment of the grid (k_1, k_2, k_3) depend on the dimensions of each lattice. This adaptation significantly improves the accuracy and efficiency of the calculations, resulting in overall faster computation. To calculate the value of k_i for a specific dimension in reciprocal space,

$$k_i = \frac{1}{l_i \times k_{resol}}$$

is employed, where l_i represents the length of a lattice vector, and k_{resol} is the reciprocal-space resolution defined by the user. The resulting value of k_i is then rounded up to the nearest integer value.

structures, and explore the relationships between composition, structure, and stability. This comprehensive approach contributes to a more comprehensive understanding of the system under investigation.

B APPENDIX: EXPERIMENTAL SUPPORT

Since the results of this work are compared and combined with experimental results held in collaboration with Dr. Vesselli's group at SFG laboratory (Elettra synchrotron-radiation center and the University of Trieste), a very brief overview of experimental methods and tools will help to follow the discussion.

B.1 EXPERIMENTAL OVERVIEW

The study of our experimental collaborators focuses on the synthesis and characterization of oxidation/hydrogenation of honeycomb boron (H-hB) on Al(111). This represents a significant advancement towards achieving a stable honeycomb borophene/borophane phases as well as new insight into the effect of oxygen on AlB_2 in the presence of aluminum substrate.

B.2 EXPERIMENTAL TECHNIQUES

In the field of surface science and material characterization, three widely used techniques for studying surface structures and electronic properties are Low-Energy Electron Diffraction (LEED), Infrared-Visible Sum Frequency Generation (IR-Vis SFG), and X-ray Photoelectron Spectroscopy (XPS). These methods provide valuable insights into the composition, morphology, and chemical state of surfaces and interfaces. Here, a very brief introduction to each technique is presented. Moreover, some general details of the corresponding experiments to the project are mentioned.

B.2.1 LEED

Low Energy Electron Diffraction (LEED) [52] is a surface-sensitive technique that utilizes the diffraction of low-energy electrons to determine the periodicity and symmetry of a crystalline surface. By measuring the intensity and angular distribution of the diffracted electrons, LEED can provide information about the surface unit cell,

surface reconstruction, and surface defects. LEED experiments are typically performed under ultra-high vacuum conditions, allowing for the investigation of clean and well-defined surfaces.

LEED is generally used in conjunction with other techniques, such as scanning electron microscopy (SEM), X-ray diffraction (XRD), Auger electron spectroscopy (AES), and X-ray photoelectron spectroscopy (XPS) to provide complementary information on the chemical composition of the surface [93].

B.2.2 IR-Vis SFG

As mentioned before, one of the powerful tools in the experimental investigation is Infrared-Visible Sum Frequency Generation (IR-Vis SFG) spectroscopy [54, 133], which offers unique capabilities for investigating molecular interactions at interfaces. IR-Vis SFG is a nonlinear optical technique that provides vibrational and electronic spectroscopic information with high sensitivity and specificity. By combining infrared and visible laser beams, this method allows the detection of vibrational modes and electronic transitions at surfaces and interfaces.

The advantages of IR-Vis SFG lie in its ability to selectively probe the surface region without interference from the bulk or solution phases. It provides molecular-level insights into surface adsorption, orientation, and conformational changes of molecules, as well as interfacial charge transfer processes. Additionally, IR-Vis SFG can be applied to a wide range of materials, including solid surfaces, liquid-liquid interfaces, and gas-solid interfaces. Notable advancements have been made in the understanding of interfacial water behavior.

At the Physics Department of the University of Trieste, a UHV (Ultra-High Vacuum) system with a base pressure of 5×10^{-11} mbar is available. This system accommodates standard surface science preparation and characterization techniques, such as LEED optics and an Auger spectrometer. Additionally, it is directly connected to a high-pressure reactor cell for *in situ* IR-Vis SFG (Infrared-Visible Sum Frequency Generation) spectroscopy, covering a pressure range of 10^{-10} - 10^{+3} mbar. The excitation source emits a visible beam at 532 nm (2.33 eV) with a pulse duration of 30 ps and a repetition rate of 50 Hz. It also offers tunable infrared radiation within the range of 1000-4500 cm^{-1}. To account for inherent modulations in the infrared intensity, the SFG spectra were normalized using the non-resonant signal generated by a clean reference Al(111) surface. The obtained data were then subjected to analysis using least-squares

fitting, employing a parametric, effective expression of the nonlinear second-order susceptibility described by equation:

$$\frac{I_{SFG}(\omega_{IR})}{I_{Vis}I_{IR}(\omega_{IR})} \propto \left| A_{NRes} + \sum_k \frac{A_k \exp\{i\Delta\phi_k\}}{\omega_{IR} - \omega_k + i\Gamma_k} \right|^2 .$$

B.2.3 XPS and NEXAFS

X-ray Photoelectron Spectroscopy (XPS) [31, 130] is a powerful tool for analyzing the elemental composition and chemical state of materials. It involves irradiating a sample with X-rays and measuring the kinetic energy of emitted photoelectrons. By analyzing the energy spectra of the emitted electrons, valuable information about the elemental composition, chemical bonding, and oxidation states of the surface or interface can be obtained. XPS is commonly used to investigate the surface chemistry of materials, including catalysts, semiconductors, and functionalized surfaces.

Near-Edge X-ray Absorption Fine Structure (NEXAFS) spectroscopy [119] is used to investigate the electronic and structural properties of materials at the atomic scale. It provides information about the unoccupied electronic states and the local chemical environment of atoms in a sample. This technique involves the measurement of the absorption of X-rays with energies close to and just above an absorption edge of an element of interest. The absorption spectrum contains characteristic features, including peaks and resonances, which arise from transitions between core-level and unoccupied states. These transitions are sensitive to the local bonding and electronic structure of the atoms in the material.

The experimentalists conducted X-Ray Photoelectron Spectroscopy (XPS) and Near-Edge X-ray Absorption Fine Structure (NEXAFS) spectroscopy at the FlexPES beamline located in the MAX IV synchrotron radiation facility in Lund, Sweden. They employed the same experimental setup previously used to characterize the pristine B layer at the University of Trieste. XPS measurements were performed using a SES-2002 photoelectron analyzer from Scienta-Omicron, while NEXAFS spectra were recorded using a custom-built partial electron yield multichannel-plate detector. For the B 1s edge in NEXAFS, the retardation voltage was set to -140 V. In XPS, the energy resolution was adjusted to 25 meV for Al 2p (with photon energies ranging from 145 to 155 eV) and 75 meV for B 1s (with photon energies ranging from 265 to 285 eV). In the case of B 1s NEXAFS spectra, the energy resolution was set to 15 meV.

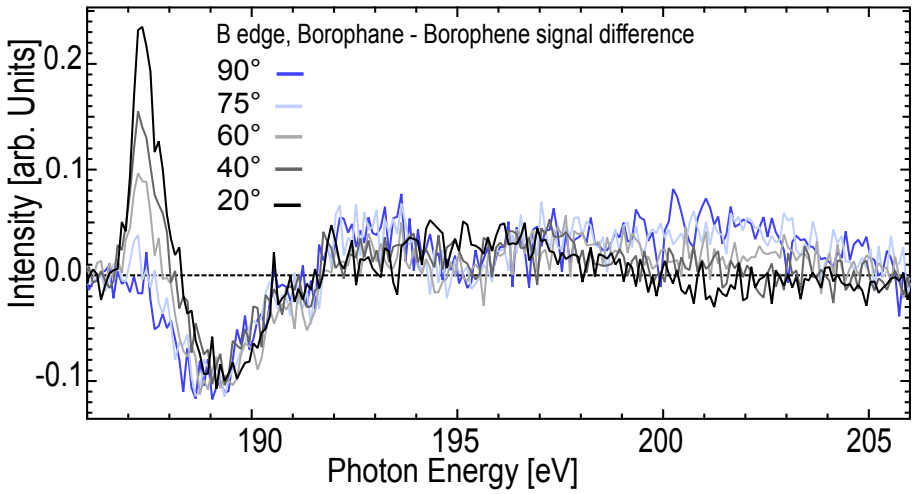

Figure B.1: Spectroscopic characterization of the B absorption edge. Dichroic behavior of the absorption intensity difference at the B edge between the hydrogenated and the bare hB/Al(111) layers. The directions refer to the angle between the electric field of the impinging, linearly polarized X-ray radiation and the normal to the surface. Data were collected in the partial electron yield mode.

B.3 REDOX COMPARISON

We will see in the following that oxidation with background O_2 and reduction with atomic H in UHV at room temperature steer the honeycomb AlB_2/Al(111) system towards opposite directions. Here for more clarity, we put the outcomes of different techniques in one frame. First, in Fig. B.2, the LEED patterns of pristine honeycomb AlB_2, AlB_2 after oxidation, and after hydrogenation are depicted. Technically, oxygen is exposed to the system as O_2 gas, while for hydrogen, H atoms are used (labeled as H_{at}), which are made by cracking H_2 at the tungsten (W) filament. Note that, colored spots in the enlarged regions indicate Al (yellow), B (violet), and moiré (green) spots.

Fig. B.3 shows the IR-Vis SFG spectra of the boron layer under different conditions: pristine, oxidized, and reduced. In the central row, the spectrum represents the pristine boron layer without any additional treatments. In the top row, the boron layer was subjected to oxidation by exposure to oxygen, while in the bottom row, it was reduced by treating it with hydrogen using a thermal cracker. The data in the graph have been normalized to facilitate comparison, and a line profile and non-linear susceptibility model have been used to fit and deconvolute the spectra. The line profile and non-linear susceptibility model are techniques commonly employed

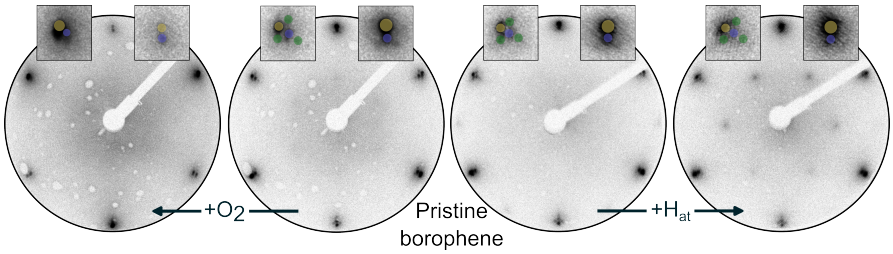

Figure B.2: LEED patterns of (a) AlB_2 after oxidation with 10^2 L O_2, pristine honeycomb AlB_2 obtained by depositing B at about (b) 0.15 ML/min and (c) 0.05 ML/min, and (d) after reduction with H_{at} (made by cracking 10 L H_2). Moiré patterns are spotted on enlarged parts. Electron energy: 47.5 eV.

in spectroscopy to analyze and interpret complex spectral data [24, 125].

By examining the spectra under different conditions, we can observe changes in the vibrational and electronic properties of the boron layer. The differences in the spectra provide valuable insights into the effects of oxidation and reduction on the boron layer's chemical structure and bonding behavior.

Figure B.4 indicates a good overview of photoelectron and X-ray absorption spectroscopy characterization of the pristine AlB_2 (central row) in comparison with oxidized (10^{+3} L O_2 top row), and reduced (10 L H_{at} through the thermal cracker, bottom row) AlB_2 phases. The deconvolution profiles[1] are shown together with the best fit for the B 1s core level in column (a). In the case of the Al 2p spectra (column (b)), the positions of the main $2p_{3/2}$ lines are indicated by the dashed lines. This data, aligned in columns (a) and (b), were collected with a photon energy of 270 eV. Moreover, the NEXAFS of the B 1s edge, shown in column (c), data are reported for two impinging photon polarization orientations with respect to the surface normal (90° and 20°, empty and filled markers, respectively) with spectral differences with respect to pristine AlB_2 plotted in blue. On the other hand, the dashed lines indicate the energy positions of the absorption features specifically induced by the oxidation/reduction reactions. Furthermore, differences (blue) with respect to bare AlB_2 are only plotted to put in evidence the spectral modifications.

1 Deconvolution is a computational method that treats the image as an estimate of the true specimen intensity and using an expression for the point spread function performs the mathematical inverse of the imaging process to obtain an improved estimate of the image intensity.

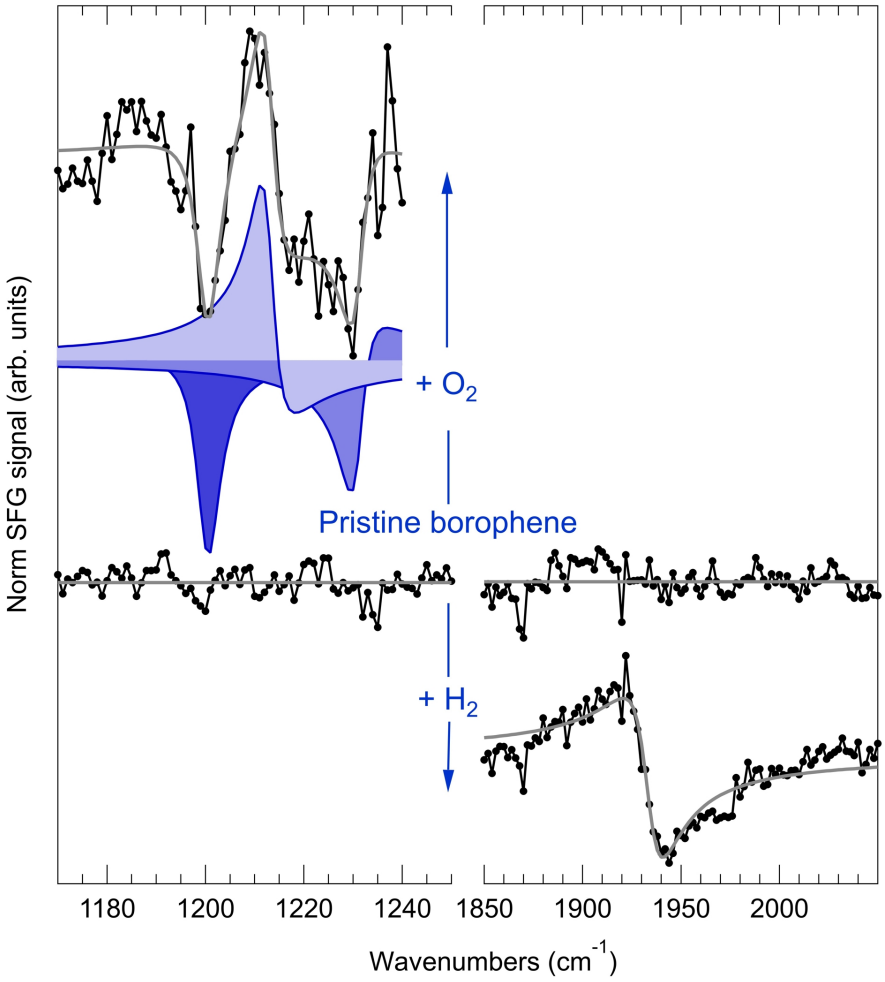

Figure B.3: IR-Vis SFG spectra of pristine (middle row), oxidized (top row), and reduced (bottom row) boron layers. The data were normalized and fitted using the line profile and non-linear susceptibility model [24, 125].

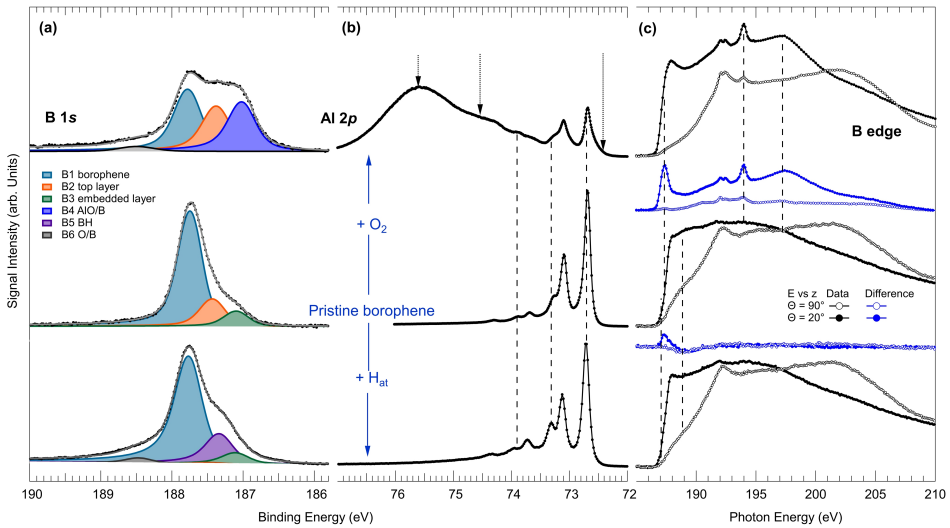

Figure B.4: Photoelectron with $h\nu$ = 270 eV (a,b) and X-ray absorption (c) spectroscopy characterization of pristine, oxidized, and reduced AlB2 phases. Profiles of B 1s core level (a) and Al 2p spectra (b) are shown with fitting details. NEXAFS of the B 1s edge (c) is presented for two photon polarizations (90° and 20°, empty and filled markers, respectively), with spectral differences shown in blue. Dashed lines indicate energy positions affected by oxidation/reduction reactions. Blue differences with respect to bare AlB_2 highlight spectral modifications.

BIBLIOGRAPHY

[1] The growth temperature is of the order of 500 K and the M flux is $\approx$ 0.1 ML/min, roughly corresponding to a pressure $\lesssim 10^{-8}$ mbar.

[2] Anastassia N. Alexandrova and Alexander I. Boldyrev. "Search for the Lino/+1/-1 (n = 5-7) Lowest-Energy Structures Using the ab Initio Gradient Embedded Genetic Algorithm (GEGA). Elucidation of the Chemical Bonding in the Lithium Clusters". In: *Journal of Chemical Theory and Computation* 1.4 (2005). PMID: 26641677, pp. 566–580. DOI: 10.1021/ct050093g. eprint: https://doi.org/10.1021/ct050093g. URL: https://doi.org/10.1021/ct050093g.

[3] Mohammed AlQuraishi. "Machine learning in protein structure prediction". In: *Current Opinion in Chemical Biology* 65 (2021). Mechanistic Biology * Machine Learning in Chemical Biology, pp. 1–8. ISSN: 1367-5931. DOI: https://doi.org/10.1016/j.cbpa.2021.04.005. URL: https://www.sciencedirect.com/science/article/pii/S1367593121000508.

[4] Nongnuch Artrith and Jörg Behler. "High-dimensional neural network potentials for metal surfaces: A prototype study for copper". In: *Physical Review B* 85.4 (2012), p. 045439.

[5] Behnam Assadollahzadeh and Peter Schwerdtfeger. "A systematic search for minimum structures of small gold clusters Aun (n=2–20) and their electronic properties". In: *The Journal of Chemical Physics* 131.6 (2009), p. 064306. DOI: 10.1063/1.3204488. eprint: https://aip.scitation.org/doi/pdf/10.1063/1.3204488. URL: https://aip.scitation.org/doi/abs/10.1063/1.3204488.

[6] Stefano Baroni et al. "Phonons and related crystal properties from density-functional perturbation theory". In: *Reviews of Modern Physics* 73 (2 July 2001), pp. 515–562. DOI: 10.1103/RevModPhys.73.515. URL: https://link.aps.org/doi/10.1103/RevModPhys.73.515.

[7] Stefano Baroni et al. "Phonons and related crystal properties from density-functional perturbation theory". In: *Reviews of Modern Physics* 73 (2 July 2001), pp. 515–562. DOI: 10.1103/RevModPhys.73.515. URL: https://link.aps.org/doi/10.1103/RevModPhys.73.515.

[8] Albert P Bartók et al. "Gaussian approximation potentials: The accuracy of quantum mechanics, without the electrons". In: *Physical review letters* 104.13 (2010), p. 136403.

[9] Albert P. Bartók, Risi Kondor, and Gábor Csányi. "On representing chemical environments". In: *Physical Review B* 87 (18 May 2013), p. 184115. DOI: 10.1103/PhysRevB.87.184115. URL: https://link.aps.org/doi/10.1103/PhysRevB.87.184115.

[10] Jörg Behler. "Atom-centered symmetry functions for constructing high-dimensional neural network potentials". In: *The Journal of Chemical Physics* 134.7 (2011), p. 074106. DOI: doi:10.1063/1.3553717.

[11] Jörg Behler and Michele Parrinello. "Generalized neural-network representation of high-dimensional potential-energy surfaces". In: *Physical Review Letters* 98.14 (2007), p. 146401.

[12] Lennart Bengtsson. "Dipole correction for surface supercell calculations". In: *Physical Review B* 59 (19 May 1999), pp. 12301–12304. DOI: 10.1103/PhysRevB.59.12301.

[13] Pietro Biasin et al. "From borophene polymorphs towards a single honeycomb borophane phase: reduction of hexagonal boron layers on Al(111)". In: *Phys.* 6 (1 Nov. 2023), p. 1. DOI: 10. URL: https://link.

[14] U. Bischler and E. Bertel. "Simple source of atomic hydrogen for ultrahigh vacuum applications". In: *Journal of Vacuum Science & Technology A* 11.2 (Mar. 1993), pp. 458–460. ISSN: 0734-2101. DOI: 10.1116/1.578754. eprint: https://pubs.aip.org/avs/jva/article-pdf/11/2/458/11853287/458_1_online.pdf. URL: https://doi.org/10.1116/1.578754.

[15] Max Born and Kun Huang. "Dynamical theory of crystal lattices Oxford University Press". In: *London, New York* (1954).

[16] H Böttger. "Principles of the Theory of Lattice". In: *Dynamics (Weinheim: Physik-Verlag, 1983) Ch* 2 (1983).

[17] H. Brune et al. "Interaction of oxygen with Al(111) studied by scanning tunneling microscopy". In: *The Journal of Chemical Physics* 99.3 (Aug. 1993), pp. 2128–2148. ISSN: 0021-9606. DOI: 10.1063/1.465278. eprint: https://pubs.aip.org/aip/jcp/article-pdf/99/3/2128/11160897/2128_1_online.pdf. URL: https://doi.org/10.1063/1.465278.

[18] T. Bürgi et al. "Reactions of gas phase H atoms with ethylene, acetylene and ethane adsorbed on Ni(111)". In: *Surface Science* 501.1 (2002), pp. 49–73. ISSN: 0039-6028. DOI: https://doi.org/10.1016/S0039-6028(01)01755-1. URL: https://www.sciencedirect.com/science/article/pii/S0039602801017551.

[19] R. Car and M. Parrinello. "Unified Approach for Molecular Dynamics and Density-Functional Theory". In: *Physical Review Letters* 55 (22 Nov. 1985), pp. 2471–2474. DOI: 10.1103/PhysRevLett.55.2471. URL: https://link.aps.org/doi/10.1103/PhysRevLett.55.2471.

[20] D. M. Ceperley and B. J. Alder. "Ground State of the Electron Gas by a Stochastic Method". In: *Physical Review Letters* 45 (7 Aug. 1980), pp. 566–569. DOI: 10.1103/PhysRevLett.45.566. URL: https://link.aps.org/doi/10.1103/PhysRevLett.45.566.

[21] Shaodong Cheng et al. "Quantification of the boron speciation in alkali borosilicate glasses by electron energy loss spectroscopy". In: *Scientific Reports* 5.1 (2015), p. 17526.

[22] W Cochran and RA Cowley. "Dielectric constants and lattice vibrations". In: *Journal of Physics and Chemistry of Solids* 23.5 (1962), pp. 447–450.

[23] Valentino R. Cooper. "Van der Waals density functional: An appropriate exchange functional". In: *Physical Review B* 81 (16 Apr. 2010), p. 161104. DOI: 10.1103/PhysRevB.81.161104. URL: https://link.aps.org/doi/10.1103/PhysRevB.81.161104.

[24] Manuel Corva et al. "Carbon dioxide reduction on Ir (111): stable hydrocarbon surface species at near-ambient pressure". In: *Physical Chemistry Chemical Physics* 18.9 (2016), pp. 6763–6772.

[25] Marc G. Cuxart et al. "Borophenes made easy". In: *Science Advances* 7.45 (2021), eabk1490. DOI: 10.1126/sciadv.abk1490.

[26] A. Dal Corso. "Pseudopotentials periodic table: From H to Pu". In: *Computational Materials Science* 95 (2014). The PAW datasets used for B, Al, and O are B.pbe-n-kjpaw_psl.1.1.0.upf, Al.pbe-n-kjpaw_psl.1.1.0.upf, and O.pbe-n-kjpaw_psl.0.1.upf, respectively. See: https://dalcorso.github.io/pslibrary., pp. 337–350.

[27] Volker L Deringer and Gábor Csányi. "Machine learning based interatomic potential for amorphous carbon". In: *Physical Review B* 95.9 (2017), p. 094203.

[28] M. Dion et al. "Van der Waals Density Functional for General Geometries". In: *Physical Review Letters* 92 (24 June 2004), p. 246401. DOI: 10.1103/PhysRevLett.92.246401. URL: https://link.aps.org/doi/10.1103/PhysRevLett.92.246401.

[29] Andrew M. Duffin et al. "pH-dependent x-ray absorption spectra of aqueous boron oxides". In: *The Journal of Chemical Physics* 134.15 (Apr. 2011), p. 154503. ISSN: 0021-9606. DOI: 10.1063/1.3574838. eprint: https://pubs.aip.org/aip/jcp/article-pdf/doi/10.1063/1.3574838/14020645/154503_1_online.pdf. URL: https://doi.org/10.1063/1.3574838.

[30] C. Eibl, G. Lackner, and A. Winkler. "Quantitative characterization of a highly effective atomic hydrogen doser". In: *Journal of Vacuum Science & Technology A* 16.5 (Sept. 1998), pp. 2979–2989. ISSN: 0734-2101. DOI: 10.1116/1.581449. eprint: https://pubs.aip.org/avs/jva/article-pdf/16/5/2979/7432502/2979_1_online.pdf. URL: https://doi.org/10.1116/1.581449.

[31] C.S. Fadley. "X-ray photoelectron spectroscopy: Progress and perspectives". In: *Journal of Electron Spectroscopy and Related Phenomena* 178-179 (2010). Trends in X-ray Photoelectron Spectroscopy of solids (theory, techniques and applications), pp. 2–32. ISSN: 0368-2048. DOI: https://doi.org/10.1016/j.elspec.2010.01.006. URL: https://www.sciencedirect.com/science/article/pii/S0368204810000095.

[32] Somayeh Faraji et al. "High accuracy and transferability of a neural network potential through charge equilibration for calcium fluoride". In: *Physical Review B* 95.10 (2017), p. 104105.

[33] B. Feng et al. "Dirac Fermions in Borophene". In: *Physical review letters* 118 (9 2017), p. 096401. DOI: doi.org/10.1103/PhysRevLett.118.096401.

[34] Baojie Feng et al. "Experimental realization of two-dimensional boron sheets". In: *Nature chemistry* 8.6 (2016), pp. 563–568. ISSN: 1755-4349. DOI: 10.1038/nchem.2491.

[35] Daan Frenkel and Berend Smit. *Understanding Molecular Simulation*. 2nd edn., Academic Press, San Diego, 2002. ISBN: 978-0-12-267351-1.

[36] Asahi Fujino et al. "Hydrogenated Borophene Shows Catalytic Activity as Solid Acid". In: *ACS Omega* 4.9 (2019). PMID: 31497729, pp. 14100–14104. DOI: 10.1021/acsomega.9b02020. eprint: https://doi.org/10.1021/acsomega.9b02020. URL: https://doi.org/10.1021/acsomega.9b02020.

[37] Miao Gao et al. "Electron-phonon coupling in a honeycomb borophene grown on Al(111) surface". In: *Physical Review B* 100 (2 July 2019), p. 024503. DOI: 10.1103/PhysRevB.100.024503.

[38] M. Gastegger et al. "wACSF—Weighted atom-centered symmetry functions as descriptors in machine learning potentials". In: *The Journal of Chemical Physics* 148.24 (Mar. 2018), p. 241709. ISSN: 0021-9606. DOI: 10.1063/1.5019667. eprint: https://pubs.aip.org/aip/jcp/article-pdf/doi/10.1063/1.5019667/16654327/241709_1_online.pdf. URL: https://doi.org/10.1063/1.5019667.

[39] Daiyu Geng et al. "Experimental evidence of monolayer AlB_2 with symmetry-protected Dirac cones". In: *Physical Review B* 101 (16 Apr. 2020), p. 161407. DOI: 10.1103/PhysRevB.101.161407.

[40] S Alireza Ghasemi et al. "Interatomic potentials for ionic systems with density functional accuracy based on charge densities obtained by a neural network". In: *Physical review B* 92.4 (2015), p. 045131.

[41] Paolo Giannozzi et al. "Ab initio calculation of phonon dispersions in semiconductors". In: *Physical Review B* 43 (9 Mar. 1991), pp. 7231–7242. DOI: 10.1103/PhysRevB.43.7231. URL: https://link.aps.org/doi/10.1103/PhysRevB.43.7231.

[42] Paolo Giannozzi et al. "Ab initio calculation of phonon dispersions in semiconductors". In: *Physical Review B* 43.9 (1991), p. 7231.

[43] Paolo Giannozzi et al. "Quantum ESPRESSO toward the exascale". In: *The Journal of Chemical Physics* 152.15 (Apr. 2020), p. 154105. ISSN: 0021-9606. DOI: 10.1063/5.0005082. eprint: https://pubs.aip.org/aip/jcp/article-pdf/doi/10.1063/5.0005082/16721881/154105_1_online.pdf. URL: https://doi.org/10.1063/5.0005082.

[44] Paolo Giannozzi et al. "QUANTUM ESPRESSO: a modular and open-source software project for quantum simulations of materials". In: *Journal of Physics: Condensed Matter* 21.39 (Sept. 2009), p. 395502. DOI: 10.1088/0953-8984/21/39/395502. URL: https://doi.org/10.1088/0953-8984/21/39/395502.

[45] Stefan Grimme et al. "A consistent and accurate ab initio parametrization of density functional dispersion correction (DFT-D) for the 94 elements H-Pu". In: *The Journal of Chemical Physics* 132.15 (2010), p. 154104. DOI: 10.1063/1.3382344.

[46] Olivier Guise, Jeremy Levy, and John T. Yates. "Direct measurement of the direction of interface motion in the oxidation of metals and covalent solids—Al(111) and Si(100) oxidation with O2 at 300 K". In: *Thin Solid Films* 496.2 (2006), pp. 426–430. ISSN: 0040-6090. DOI: https://doi.org/10.1016/j.

tsf.2005.08.358. URL: https://www.sciencedirect.com/science/article/pii/S0040609005015671.

[47] Roohollah Hafizi et al. "A neural-network potential through charge equilibration for WS_2: From clusters to sheets". In: *The Journal of Chemical Physics* 147 (23 Dec. 2017), p. 234306. DOI: 10.1063/1.5003904.

[48] Katja Hansen et al. "Machine learning predictions of molecular properties: Accurate many-body potentials and nonlocality in chemical space". In: *The journal of physical chemistry letters* 6.12 (2015), pp. 2326–2331.

[49] Corey Hardin, Taras V Pogorelov, and Zaida Luthey-Schulten. "Ab initio protein structure prediction". In: *Current Opinion in Structural Biology* 12.2 (2002), pp. 176–181. ISSN: 0959-440X. DOI: https://doi.org/10.1016/S0959-440X(02)00306-8. URL: https://www.sciencedirect.com/science/article/pii/S0959440X02003068.

[50] Fred L Hirshfeld. "Bonded-atom fragments for describing molecular charge densities". In: *Theoretica chimica acta* 44 (1977), pp. 129–138.

[51] P. Hohenberg and W. Kohn. "Inhomogeneous Electron Gas". In: *Phys. Rev.* 136 (3B Nov. 1964), B864–B871. DOI: 10.1103/PhysRev.136.B864. URL: https://link.aps.org/doi/10.1103/PhysRev.136.B864.

[52] Michel A. Hove, William H. Weinberg, and Chi-Ming Chan. *Low-Energy Electron Diffraction (Experiment, Theory and Surface Structure Determination)*. Springer Series in Surface Sciences. Springer Berlin, Heidelberg, 2012. ISBN: 978-3-642-82721-1. DOI: https://doi.org/10.1007/978-3-642-82721-1.

[53] Yufeng Huang et al. "Density functional theory based neural network force fields from energy decompositions". In: *Physical Review B* 99.6 (2019), p. 064103.

[54] Oleksandr Isaienko et al. "Observation of the Bending Mode of Interfacial Water at Silica Surfaces by Near-Infrared Vibrational Sum-Frequency Generation Spectroscopy of the [Stretch + Bend] Combination Bands". In: *The Journal of Physical Chemistry Letters* 4.3 (2013). PMID: 26281750, pp. 531–535. DOI: 10.1021/jz3015088. eprint: https://doi.org/10.1021/jz3015088. URL: https://doi.org/10.1021/jz3015088.

[55] Yuchong Kang et al. "Substrate-Mediated Borophane Polymorphs through Hydrogenation of Two-Dimensional Boron Sheets". In: *The Journal of Physical Chemistry Letters* 13.43 (2022). PMID: 36300795, pp. 10222–10229. DOI: 10.1021/acs.jpclett.2c02417. URL: https://doi.org/10.1021/acs.jpclett.2c02417.

[56] J. Karthikeyan et al. "Borophene layers on an Al(111) surface – the finding of a borophene layer with hexagonal double chains and B9 nonagons using ab initio calculations". In: *Nanoscale* 10 (36 2018), pp. 17198–17205. DOI: 10.1039/C8NR04638G.

[57] RD King-Smith and David Vanderbilt. "Theory of polarization of crystalline solids". In: *Physical Review B* 47.3 (1993), p. 1651.

[58] Brian Kiraly et al. "Borophene Synthesis on Au(111)". In: *ACS Nano* 13.4 (2019). PMID: 30844248, pp. 3816–3822. DOI: 10.1021/acsnano.8b09339. URL: https://doi.org/10.1021/acsnano.8b09339.

[59] Douglas J. Klein et al. "Hückeloid model for planar boranes". In: *Theoretical Chemistry Accounts* 140 (2021), p. 55. ISSN: 1432-2234. DOI: 10.1007/s00214-021-02752-x. URL: https://doi.org/10.1007/s00214-021-02752-x.

[60] Tsk wai Ko et al. "A fourth-generation high-dimensional neural network potential with accurate electrostatics including non-local charge transfer". In: *Nature Communications* 12 (2021), p. 398.

[61] W. Kohn and L. J. Sham. "Self-Consistent Equations Including Exchange and Correlation Effects". In: *Phys. Rev.* 140 (4A Nov. 1965), A1133–A1138. DOI: 10.1103/PhysRev.140.A1133. URL: https://link.aps.org/doi/10.1103/PhysRev.140.A1133.

[62] Longjuan Kong, Kehui Wu, and Lan Chen. "Recent progress on borophene: Growth and structures". In: *Frontiers of Physics* 13 (3 2018), p. 138105. DOI: 10.1007/s11467-018-0752-8.

[63] Kyuho Lee et al. "Higher-accuracy van der Waals density functional". In: *Physical Review B* 82 (8 Aug. 2010), p. 081101. DOI: 10.1103/PhysRevB.82.081101. URL: https://link.aps.org/doi/10.1103/PhysRevB.82.081101.

[64] Fleur Legrain et al. "How chemical composition alone can predict vibrational free energies and entropies of solids". In: *Chemistry of Materials* 29.15 (2017), pp. 6220–6227.

[65] Cyrus Levinthal. "Are there pathways for protein folding?" In: *J. Chim. Phys.* 65 (1968), pp. 44–45. DOI: https://doi.org/10.1051/jcp/1968650044.

[66] Linfei Li et al. "Chemically identifying single adatoms with single-bond sensitivity during oxidation reactions of borophene". In: *Nature Communications* 13.1 (2022), p. 1796.

[67] Q. Li et al. "Synthesis of borophane polymorphs through hydrogenation of borophene". In: *Science (New York, N.Y.)* 371 (6534 2021), pp. 1143–1148. DOI: https://doi.org/10.1126/science.abg1874.

[68] Qing-Jie Li et al. "Development of robust neural-network interatomic potential for molten salt". In: *Cell Reports Physical Science* 2.3 (2021), p. 100359. ISSN: 2666-3864. DOI: https://doi.org/10.1016/j.xcrp.2021.100359. URL: https://www.sciencedirect.com/science/article/pii/S2666386421000448.

[69] Wenbin Li et al. "Experimental realization of honeycomb borophene". In: *Science Bulletin* 63.5 (2018), pp. 282–286. ISSN: 2095-9273. DOI: 10.1016/j.scib.2018.02.006. URL: https://www.sciencedirect.com/science/article/pii/S2095927318300707.

[70] Zhenwei Li, James R Kermode, and Alessandro De Vita. "Molecular dynamics with on-the-fly machine learning of quantum-mechanical forces". In: *Physical review letters* 114.9 (2015), p. 096405.

[71] Guigao Liu et al. "Elemental Boron for Efficient Carbon Dioxide Reduction under Light Irradiation". In: *Angewandte Chemie International Edition* 56.20 (2017), pp. 5570–5574. DOI: 10.1002/anie.201701370.

[72] Xiaolong Liu et al. "Borophene synthesis beyond the single-atomic-layer limit". In: *Nature Materials* 21 (2022), pp. 35–40. DOI: 10.1038/s41563-021-01084-2.

[73] Xiaolong Liu et al. "Probing borophene oxidation at the atomic scale". In: *Nanotechnology* 33.23 (2022), p. 235702.

[74] David Loffreda. "Theoretical insight of adsorption thermodynamics of multifunctional molecules on metal surfaces". In: *Surface Science* 600.10 (2006), pp. 2103–2112. ISSN: 0039-6028. DOI: https://doi.org/10.1016/j.susc.2006.02.045. URL: https://www.sciencedirect.com/science/article/pii/S0039602806002287.

[75] Ruggero Lot et al. "PANNA: Properties from artificial neural network architectures". In: *Computer Physics Communications* 256 (2020), p. 107402.

[76] Xinzhou Ma and Sebastian Günther. "Imaging the confined surface oxidation of Ni3Al(111) by in situ high temperature scanning tunneling microscopy". In: *Phys. Chem. Chem. Phys.* 20 (34 2018), pp. 21844–21855. DOI: 10.1039/C8CP03197E. URL: http://dx.doi.org/10.1039/C8CP03197E.

[77] "Machine learning for molecular and materials science". In: 559 (7715 2018), pp. 547–555. ISSN: 0028-0836. DOI: https://doi.org/10.1038/s41586-018-0337-2.

[78] Andrew J. Mannix et al. "Synthesis of borophenes: Anisotropic, two-dimensional boron polymorphs". In: *Science* 350.6267 (2015), pp. 1513–1516. DOI: 10.1126/science.aad1080. URL: https://www.science.org/doi/abs/10.1126/science.aad1080.

[79] Nicola Marzari et al. "Thermal Contraction and Disordering of the Al(110) Surface". In: *Physical Review Letters* 82 (16 Apr. 1999), pp. 3296–3299. DOI: 10.1103/PhysRevLett.82.3296.

[80] Iwao Matsuda and Kehui Wu. *2D Boron: Boraphene, Borophene, Boronene*. Springer Nature Switzerland AG, 2021. ISBN: 978-3-030-49999-0.

[81] Marco Molinari et al. "Water Adsorption and Its Effect on the Stability of Low Index Stoichiometric and Reduced Surfaces of Ceria". In: *The Journal of Physical Chemistry C* 116.12 (2012), pp. 7073–7082. DOI: 10.1021/jp300576b. URL: https://doi.org/10.1021/jp300576b.

[82] Tobias Morawietz, Vikas Sharma, and Jörg Behler. "A neural network potential-energy surface for the water dimer based on environment-dependent atomic energies and charges". In: *The Journal of Chemical Physics* 136.6 (Feb. 2012), p. 064103. ISSN: 0021-9606. DOI: 10.1063/1.3682557. eprint: https://pubs.aip.org/aip/jcp/article-pdf/doi/10.1063/1.3682557/15448232/064103_1_online.pdf. URL: https://doi.org/10.1063/1.3682557.

[83] M. Nakhaee, S. A. Ketabi, and F. M. Peeters. "Tight-binding model for borophene and borophane". In: *Physical Review B* 97 (12 Mar. 2018), p. 125424. DOI: 10.1103/PhysRevB.97.125424.

[84] C. Ocal, B. Basurco, and S. Ferrer. "An ISS-XPS study on the oxidation of Al(111); identification of stoichiometric and reduced oxide surfaces". In: *Surface Science* 157.1 (1985), pp. 233–243. ISSN: 0039-6028. DOI: https://doi.org/10.1016/0039-6028(85)90645-4. URL: https://www.sciencedirect.com/science/article/pii/0039602885906454.

[85] Artem R. Oganov and Colin W. Glass. "Crystal structure prediction using ab initio evolutionary techniques: Principles and applications". In: *The Journal of Chemical Physics* 124.24 (2006), p. 244704. DOI: 10.1063/1.2210932.

[86] C. W. Ong et al. "X-ray photoemission spectroscopy of nonmetallic materials: Electronic structures of boron and BxOy". In: *Journal of Applied Physics* 95.7 (Mar. 2004), pp. 3527–3534. ISSN: 0021-8979. DOI: 10.1063/1.1651321. eprint: https://pubs.aip.org/aip/jap/article-pdf/95/7/3527/10634593/3527_1_online.pdf. URL: https://doi.org/10.1063/1.1651321.

[87] Laerte L. Patera et al. "In Situ Observations of the Atomistic Mechanisms of Ni Catalyzed Low Temperature Graphene Growth". In: *Acs Nano* 7.9 (Sept. 2013), pp. 7901–7912. DOI: 10.1021/nn402927q.

[88] Linus Pauling and Robert B. Corey. "A Proposed Structure For The Nucleic Acids." In: *Proceedings of the National Academy of Sciences of the United States of America* 39 (1953), pp. 84–97. DOI: 10.1073/pnas.39.2.84.

[89] J. P. Perdew and Alex Zunger. "Self-interaction correction to density-functional approximations for many-electron systems". In: *Physical Review B* 23 (10 May 1981), pp. 5048–5079. DOI: 10.1103/PhysRevB.23.5048. URL: https://link.aps.org/doi/10.1103/PhysRevB.23.5048.

[90] John P. Perdew, Kieron Burke, and Matthias Ernzerhof. "Generalized Gradient Approximation Made Simple". In: *Physical Review Letters* 77 (18 Oct. 1996), pp. 3865–3868. DOI: 10.1103/PhysRevLett.77.3865.

[91] John P. Perdew and Yue Wang. "Accurate and simple analytic representation of the electron-gas correlation energy". In: *Physical Review B* 45 (23 June 1992), pp. 13244–13249. DOI: 10.1103/PhysRevB.45.13244. URL: https://link.aps.org/doi/10.1103/PhysRevB.45.13244.

[92] Zachary A. Piazza et al. "Planar hexagonal B36 as a potential basis for extended single-atom layer boron sheets". In: *Nature Communications* 5 (2014), p. 3113. DOI: 10.1038/ncomms4113.

[93] *Practical surface analysis : by Auger and x-ray photoelectron spectroscopy / edited by D. Briggs and M.P. Seah.* eng. Chichester: Wiley, 1983.

[94] Gianluca Prandini et al. "A Standard Solid State Pseudopotentials (SSSP) library optimized for precision and efficiency". In: *Materials Cloud Archive 2021* 76 (2021). DOI: 10.24435/materialscloud:rz-77.

[95] A B Preobrajenski et al. "Strong participator channels in the non-radiative resonant decay of B 1s excitation in B_2O_3". In: *Physica Scripta* 2005.T115 (Jan. 2005), p. 1071. DOI: 10.1238/Physica.Topical.115a01071. URL: https://dx.doi.org/10.1238/Physica.Topical.115a01071.

[96] Alexei B. Preobrajenski et al. "Honeycomb Boron on Al(111): From the Concept of Borophene to the Two-Dimensional Boride". In: *ACS Nano* 15.9 (2021). PMID: 34460239, pp. 15153–15165. DOI: 10.1021/acsnano.1c05603. URL: https://doi.org/10.1021/acsnano.1c05603.

[97] Pranay Ranjan et al. "Freestanding Borophene and Its Hybrids". In: *Advanced Materials* 31.27 (2019), p. 1900353. DOI: 10.1002/adma.201900353. URL: https://onlinelibrary.wiley.com/doi/abs/10.1002/adma.201900353.

[98] Anthony K Rappe and William A Goddard III. "Charge equilibration for molecular dynamics simulations". In: *The Journal of Physical Chemistry* 95.8 (1991), pp. 3358–3363.

[99] Raffaele Resta. "Macroscopic polarization in crystalline dielectrics: the geometric phase approach". In: *Reviews of modern physics* 66.3 (1994), p. 899.

[100] Karsten Reuter and Matthias Scheffler. "Composition, structure, and stability of RuO_2(110) as a function of oxygen pressure". In: *Physical Review B* 65 (3 Dec. 2001), p. 035406. DOI: 10.1103/PhysRevB.65.035406.

[101] Karsten Reuter, Cathy Stampfl, and Matthias Scheffler. *Ab Initio Thermodynamics and Statistical Mechanics of Surface Properties and Functions*. In: S. Yip (ed.), Handbook of Materials Modeling, Part A. Methods, Springer, Berlin, 2005. ISBN: 1-4020-3287-0.

[102] J. Rogal, K. Reuter, and Max-Planck-Gesellschaft zur Förderung der Wissenschaften. Fritz-Haber-Institut. *Ab Initio Atomistic Thermodynamics for Surfaces: A Primer*. AD-a476 575. Defense Technical Information Center, 2006. URL: https://books.google.it/books?id=TAy0AQAACAAJ.

[103] Patrick Rowe et al. "Development of a machine learning potential for graphene". In: *Physical Review B* 97.5 (2018), p. 054303.

[104] Matthias Rupp et al. "Fast and accurate modeling of molecular atomization energies with machine learning". In: *Physical review letters* 108.5 (2012), p. 058301.

[105] I. Štich et al. "Conjugate gradient minimization of the energy functional: A new method for electronic structure calculation". In: *Physical Review B* 39 (8 Mar. 1989), pp. 4997–5004. DOI: 10.1103/PhysRevB.39.4997. URL: https://link.aps.org/doi/10.1103/PhysRevB.39.4997.

[106] Mandana Safari et al. "Growing borophene on metal substrates: A theoretical study of the role of oxygen on Al(111)". In: *Physical Review Materials* 6 (11 Nov. 2022), p. 115801. DOI: 10.1103/PhysRevMaterials.6.115801. URL: https://link.aps.org/doi/10.1103/PhysRevMaterials.6.115801.

[107] Mandana Safari et al. "Metal mono-chalcogenides ZnX and CdX (X=S, Se and Te) monolayers: Chemical bond and optical interband transitions by first principles calculations". In: *Physics Letters A* 381.6 (2017), pp. 663–670. ISSN: 0375-9601. DOI: 10.1016/j.physleta.2016.11.040. URL: https://www.sciencedirect.com/science/article/pii/S037596011631917X.

[108] Matthias Scheffler. "Thermodynamic Aspects of Bulk and Surface Defects–First-Principle Calculations -". In: *Physics of Solid Surfaces 1987*. Ed. by J. Koukal. Vol. 40. Studies in Surface Science and Catalysis. Elsevier, 1988, pp. 115–122. DOI: https://doi.org/10.1016/S0167-2991(08)65025-9. URL: https://www.sciencedirect.com/science/article/pii/S0167299108650259.

[109] Yusuf Shaidu. "Interatomic Potential for Li-C Systems from Cluster Expansion to Artificial Neural Network Techniques". PhD thesis. https://hdl.handle.net/20.500.11767/115491: Scuola Internazionale Superiore di Studi Avanzati, SISSA, 2020.

[110] Yusuf Shaidu et al. "Incorporating Long-range Electrostatics in Neural Network Potentials via Variational Charge Equilibration from Shortsighted Ingredients". In: *unpublished* (2023).

[111] Li Shao et al. "A theoretical study of several fully hydrogenated borophenes". In: *Phys. Chem. Chem. Phys.* 21 (14 2019), pp. 7630–7634. DOI: 10.1039/C9CP00468H.

[112] Alexander V Shapeev. "Moment tensor potentials: A class of systematically improvable interatomic potentials". In: *Multiscale Modeling & Simulation* 14.3 (2016), pp. 1153–1173.

[113] Masahiro Shibuta et al. "Al13- and B@ Al12- superatoms on a molecularly decorated substrate". In: *Nature communications* 13.1 (2022), p. 1336.

[114] G. Simon et al. "Hyper-Raman scattering analysis of the vibrations in vitreous boron oxide". In: *Physical Review B* 76 (5 Aug. 2007), p. 054210. DOI: 10.1103/PhysRevB.76.054210. URL: https://link.aps.org/doi/10.1103/PhysRevB.76.054210.

[115] K.A. Simonov et al. "Controllable oxidation of h-BN monolayer on Ir(111) studied by core-level spectroscopies". In: *Surface Science* 606.3 (2012), pp. 564–570. ISSN: 0039-6028. DOI: https://doi.org/10.1016/j.susc.2011.11.031. URL: https://www.sciencedirect.com/science/article/pii/S003960281100464X.

[116] Jordan C Smith et al. "Boron substitution in aluminum cluster anions: magic clusters and reactivity with oxygen". In: *The Journal of Physical Chemistry A* 118.37 (2014), pp. 8485–8492.

[117] Justin S Smith, Olexandr Isayev, and Adrian E Roitberg. "ANI-1: an extensible neural network potential with DFT accuracy at force field computational cost". In: *Chemical science* 8.4 (2017), pp. 3192–3203.

[118] Thibault Sohier, Matteo Calandra, and Francesco Mauri. "Density functional perturbation theory for gated two-dimensional heterostructures: Theoretical developments and application to flexural phonons in graphene". In: *Physical Review B* 96 (7 Aug. 2017), p. 075448. DOI: 10.1103/PhysRevB.96.075448.

[119] Joachim Stöhr. *NEXAFS Spectroscopy*. Springer Berlin, Heidelberg, 1979, p. 190. DOI: https://doi.org/10.1007/978-3-662-02853-7.

[120] Qiang Sun, Karsten Reuter, and Matthias Scheffler. "Effect of a humid environment on the surface structure of $RuO_2(110)$". In: *Physical Review B* 67 (20 May 2003), p. 205424. DOI: 10.1103/PhysRevB.67.205424. URL: https://link.aps.org/doi/10.1103/PhysRevB.67.205424.

[121] Adam R. Symington et al. "surfinpy: A Surface Phase Diagram Generator". In: *Journal of Open Source Software* 4.34 (2019), p. 1210. DOI: 10.21105/joss.01210. URL: https://doi.org/10.21105/joss.01210.

[122] Thomas C. Allison. "NIST-JANAF Thermochemical Tables - SRD 13". In: *National Institute of Standards and Technology, License Information for NIST data* (2013). DOI: 10.18434/T42S31. URL: https://janaf.nist.gov/.

[123] Aidan P Thompson et al. "Spectral neighbor analysis method for automated generation of quantum-accurate interatomic potentials". In: *Journal of Computational Physics* 285 (2015), pp. 316–330.

[124] Aidan P. Thompson et al. "LAMMPS - a flexible simulation tool for particle-based materials modeling at the atomic, meso, and continuum scales". In: *Computer Physics Communications* 271 (2022), p. 108171. ISSN: 0010-4655. DOI: https://doi.org/10.1016/j.cpc.2021.108171. URL: https://www.sciencedirect.com/science/article/pii/S0010465521002836.

[125] CS Tian and YR Shen. "Recent progress on sum-frequency spectroscopy". In: *Surface Science Reports* 69.2-3 (2014), pp. 105–131.

[126] Atsushi Togo and Isao Tanaka. "First principles phonon calculations in materials science". In: *Scripta Materialia* 108 (2015), pp. 1–5.

[127] Masashi Tsubaki and Teruyasu Mizoguchi. "Fast and accurate molecular property prediction: learning atomic interactions and potentials with neural networks". In: *The journal of physical chemistry letters* 9.19 (2018), pp. 5733–5741.

[128] Erik Vesselli et al. "Large Interlayer Relaxation at a Metal-Oxide Interface: The Case of a Supported Ultrathin Alumina Film". In: *Physical Review Letters* 105 (4 July 2010), p. 046102. DOI: 10.1103/PhysRevLett.105.046102. URL: https://link.aps.org/doi/10.1103/PhysRevLett.105.046102.

[129] Lasse B. Vilhelmsen and Bjørk Hammer. "A genetic algorithm for first principles global structure optimization of supported nano structures". In: *The Journal of Chemical Physics* 141.4 (2014), p. 044711. DOI: 10.1063/1.4886337. eprint: https://doi.org/10.1063/1.4886337. URL: https://doi.org/10.1063/1.4886337.

[130] C.D. Wagner and G.E. Muilenberg. *Handbook of X-ray Photoelectron Spectroscopy: A Reference Book of Standard Data for Use in X-ray Photoelectron Spectroscopy*. Perkin-Elmer, 1979. URL: https://books.google.it/books?id=oY5TAAAAYAAJ.

[131] David J. Wales and Jonathan P. K. Doye. "Global Optimization by Basin-Hopping and the Lowest Energy Structures of Lennard-Jones Clusters Containing up to 110 Atoms". In: *The Journal of Physical Chemistry A* 101.28 (1997), pp. 5111–5116. DOI: 10.1021/jp970984n. eprint: https://doi.org/10.1021/jp970984n. URL: https://doi.org/10.1021/jp970984n.

[132] Han Wang et al. "DeePMD-kit: A deep learning package for many-body potential energy representation and molecular dynamics". In: *Computer Physics Communications* 228 (2018), pp. 178–184.

[133] Hong-Fei Wang. "Sum frequency generation vibrational spectroscopy (SFG-VS) for complex molecular surfaces and interfaces: Spectral lineshape measurement and analysis plus some controversial issues". In: *Progress in Surface Science* 91.4 (2016), pp. 155–182. ISSN: 0079-6816. DOI: https://doi.org/10.1016/j.progsurf.2016.10.001. URL: https://www.sciencedirect.com/science/article/pii/S0079681616300259.

[134] Yajun Wang and Michael Trenary. "Surface chemistry of boron oxidation. 2. The reactions of boron oxides B_2O_2 and B_2O_3 with boron films grown on tantalum (110)". In: *Chemistry of materials* 5.2 (1993), pp. 199–205.

[135] Zhiqiang Wang et al. "New crystal structure prediction of fully hydrogenated borophene by first principles calculations". In: *Scientific Reports* 7 (2017), p. 609. DOI: 10.1038/s41598-017-00667-x.

[136] Ch. Wöll et al. "Determination of atom positions at stacking-fault dislocations on Au(111) by scanning tunneling microscopy". In: *Physical Review B* 39 (11 Apr. 1989),

pp. 7988–7991. DOI: 10.1103/PhysRevB.39.7988. URL: https://link.aps.org/doi/10.1103/PhysRevB.39.7988.

[137] Mitchell A. Wood and Aidan P. Thompson. "Extending the accuracy of the SNAP interatomic potential form". In: *The Journal of Chemical Physics* 148.24 (Mar. 2018), p. 241721. ISSN: 0021-9606. DOI: 10.1063/1.5017641. eprint: https://pubs.aip.org/aip/jcp/article-pdf/doi/10.1063/1.5017641/16655417/241721_1_online.pdf. URL: https://doi.org/10.1063/1.5017641.

[138] Xiaojun Wu et al. "Two-Dimensional Boron Monolayer Sheets". In: *ACS Nano* 6.8 (2012), pp. 7443–7453. DOI: 10.1021/nn302696v.

[139] Tian Xie and Jeffrey C Grossman. "Crystal graph convolutional neural networks for an accurate and interpretable prediction of material properties". In: *Physical review letters* 120.14 (2018), p. 145301.

[140] Zhongjian Xie et al. "Two-Dimensional Borophene: Properties, Fabrication, and Promising Applications". In: *Research* 2020 (2020), pp. 1–23. DOI: 10.34133/2020/2624617.

[141] Ying Xu et al. "Borophane Polymorphs". In: *The Journal of Physical Chemistry Letters* 13.4 (2022). PMID: 35080410, pp. 1107–1113. DOI: 10.1021/acs.jpclett.1c03827. URL: https://doi.org/10.1021/acs.jpclett.1c03827.

[142] Luo Yan et al. "Theoretical dissection of superconductivity in two-dimensional honeycomb borophene oxide B_2O crystal with a high stability". In: *npj Computational Materials* 6 (2020), p. 94. DOI: 10.1038/s41524-020-00365-9.

[143] Yang Yang et al. "Segregation growth of epitaxial graphene overlayers on Ni(111)". In: *Science Bulletin* 61.19 (2016), pp. 1536–1542. ISSN: 2095-9273. DOI: https://doi.org/10.1007/s11434-016-1169-9. URL: https://www.sciencedirect.com/science/article/pii/S2095927316300214.

[144] Linfeng Zhang et al. "Deep potential molecular dynamics: a scalable model with the accuracy of quantum mechanics". In: *Physical review letters* 120.14 (2018), p. 143001.

[145] Ruiqi Zhang, Zhenyu Li, and Jinlong Yang. "Two-Dimensional Stoichiometric Boron Oxides as a Versatile Platform for Electronic Structure Engineering". In: *The Journal of Physical Chemistry Letters* 8.18 (2017), pp. 4347–4353. DOI: 10.1021/acs.jpclett.7b01721.

[146] Yingkai Zhang and Weitao Yang. "Comment on "Generalized Gradient Approximation Made Simple"". In: *Physical Review Letters* 80 (4 Jan. 1998), pp. 890–890. DOI: 10.1103/PhysRevLett.80.890. URL: https://link.aps.org/doi/10.1103/PhysRevLett.80.890.

[147] Zhuhua Zhang, Evgeni S. Penev, and Boris I. Yakobson. "Two-dimensional boron: structures, properties and applications". In: *Chemical Society Reviews* 46 (22 2017), pp. 6746–6763. DOI: 10.1039/C7CS00261K.

[148] Xiaofeng Zhao et al. "Strain-Engineered Metal-Free h-B2O Monolayer as a Mechanocatalyst for Photocatalysis and Improved Hydrogen Evolution Reaction". In: *The Journal of Physical Chemistry C* 124.14 (2020), pp. 7884–7892. DOI: 10.1021/acs.jpcc.0c00834.

[149] Chengyong Zhong et al. "Two-dimensional honeycomb borophene oxide: strong anisotropy and nodal loop transformation". In: *Nanoscale* 11 (5 2019), pp. 2468–2475. DOI: 10.1039/C8NR08729F.

[150] Xiang-Feng Zhou et al. "Semimetallic Two-Dimensional Boron Allotrope with Massless Dirac Fermions". In: *Physical Review BLett.* 112 (8 Feb. 2014), p. 085502. DOI: 10.1103/PhysRevLett.112.085502. URL: https://link.aps.org/doi/10.1103/PhysRevLett.112.085502.

[151] Xiang-Feng Zhou et al. "Semimetallic Two-Dimensional Boron Allotrope with Massless Dirac Fermions". In: *Physical Review Letter* 112 (8 Feb. 2014), p. 085502. DOI: 10.1103/PhysRevLett.112.085502. URL: https://link.aps.org/doi/10.1103/PhysRevLett.112.085502.

[152] Xiang-Feng Zhou et al. "Two-dimensional magnetic boron". In: *Physical Review B* 93 (8 Feb. 2016), p. 085406. DOI: 10.1103/PhysRevB.93.085406. URL: https://link.aps.org/doi/10.1103/PhysRevB.93.085406.

[153] Xiang-Feng Zhou et al. "Unexpected Reconstruction of the α-Boron (111) Surface". In: *Physical Review Letters* 113 (17 Oct. 2014), p. 176101. DOI: 10.1103/PhysRevLett.113.176101.

[154] Yunxing Zuo et al. "Performance and cost assessment of machine learning interatomic potentials". In: *The Journal of Physical Chemistry A* 124.4 (2020), pp. 731–745.